UNIVERSIDADE DE LISBOA
FACULDADE DE CIÊNCIAS
DEPARTAMENTO DE GEOLOGIA

Ore mineralogy and geochemistry of the Mandoos Volcanic Massive Sulphide (VMS) deposit, Sumail Ophiolite, Oman

Bruno Barros Moreira

Mestrado em Geologia Económica
Especialização em Prospeção Mineral

Relatório de Estágio orientado pelos Professores Doutores
António Mateus e Bernhard Pracejus

2017

UNIVERSIDADE DE LISBOA
FACULDADE DE CIÊNCIAS
DEPARTAMENTO DE GEOLOGIA

Ore mineralogy and geochemistry of the Mandoos Volcanic Massive Sulphide (VMS) deposit, Sumail Ophiolite, Oman

Bruno Barros Moreira

Mestrado em Geologia Económica
Especialização em Prospeção Mineral

Relatório de Estágio orientado pelos Professores Doutores
António Mateus e Bernhard Pracejus

2017

Table of Contents

Acknowledgments

First and foremost, I would like to thank my supervisors Prof. Dr. António Mateus and Prof. Dr. Bernhard Pracejus, for the countless discussions and proofreading of many manuscripts.

Further thanks go to Prof. Dr. Ana Jesus, as a non-official supervisor, for introducing me to Oman and giving me the opportunity to be part of this project, and also Filipa Luz for all her help and friendship during the last years.

I give special thanks to FCUL and all my professors for the teaching throughout all these years, and Dr. Pedro Rodrigues for his help in EPMA data acquisition. I gratefully thank GUtech, especially Dr. Michaela Bernecker for receiving me and make me part of a wonderful team, also Dr. Wilfried Bauer for his help with the modelling software and Mohamed Al Salmi and his amazing team that did their best to provide me the best conditions to do this work. I further thank Dr. Mathieu Bennoit (Toulouse University) and Prof. Fernando Rocha and Maria Cristina Sequeira (Aveiro University) for the acquisition of imperative data needed to accomplish this work. Many thanks go to Cyntia Mourão (Lisbon University) and all the lab technicians in SQU for their help in the sample preparation process and also a special mention to Dr. Carlos Inverno, Prof. Dr. Jorge Figueiras and Prof. Dr. Raul Jorge for their reviews and contributions to improve this work.

Further thanks go to my GE€CO colleagues, namely André Cravinho, Filipe Ribeiro, Frederico Martins, Hugo Esteves, Ivo Martins, José Roseiro, José Velez, Marcelo Silva, Miguel Santos and Rita Ferraz, for all the time spent discussing geological and non-geological topics. Extra thanks go to André Cravinho, Eduardo Soares and Theresa Boehm for all the good time spent in Oman and all their help during the elaboration of this report, this also extends to all AGEO interns, AGEO students and all the friends I made in GUtech.

I would like to thank all my friends for sharing their time, especially to Buceto™ members and I honestly thank everyone who feels addressed by this acknowledgment. I deeply acknowledge the great support and love of my family, my brother Filipe, sister Rafaella and nephew Salvador, a special mention to my mom and grandparents for all their support and strength to carry on.

Resumo

O Sultanado de Omã situa-se na península arábica e desde sempre despertou grande interesse geológico por nele aflorar a maior e mais bem preservada secção de manto superior, crosta oceânica e sedimentos pelágicos, conhecida como ofiolito de Sumail. A obducção deste ofiolito sobre a plataforma arábica ocorreu durante o Cretácico Superior, relacionando-se com o fecho do oceano Tétis. A sequência obductada pode atingir os 20 km de espessura e ocupa toda a região nordeste do Sultanado (Montanhas de Omã), formando uma faixa de direção NE-SE com ca. de 550 km de comprimento e 150 km de largura. Da base para o topo esta sequência compreende harzburgitos tectonizados (manto superior), uma porção gabroica com texturas variadas cortada por dioritos e trondjemitos, e um complexo de diques que alimenta a sequência extrusiva (lavas em almofada) superior. Esta última pode ser subdividida, dependendo dos autores, até um máximo de 5 unidades principais. *Geotimes* é a unidade basal desta sequência extrusiva, repousando diretamente sobre o complexo de dique em dique. Sobre esta assenta a unidade *Lasail* que, de acordo com Kusano *et al*. (2012), desenvolve interdigitações com a *Geotimes* sugerindo a possibilidade de corresponder a uma mera subunidade da última. A unidade *Alley* repousa sobre as duas últimas e partilha uma relação espacial com a unidade Boninítica.

Os depósitos de sulfuretos maciços vulcanogénicos localizam-se maioritariamente na região norte de Omã, entre as sequências lávicas, sobretudo na transição *Geotimes-Lasail*. Barrie e Hannington (1999) descrevem estes depósitos como sendo do tipo máfico devido à natureza das rochas encaixantes típicas nestes sistemas ofiolíticos. Os minérios são ricos em Cu e pobres em Pb quando comparados com outros depósitos do tipo VMS (*Volcanogenic Massive Sulphide*). As primeiras evidências de mineração destes depósitos remontam à Idade do Bronze, tendo incidido sobretudo nos domínios de enriquecimento secundário (supergénico) de cobre. As minas de Lasail, Bayda e Aarja, no distrito de Sohar, representam as primeiras explorações de minério, rico em calcopirite, conhecidas no país.

O depósito de Mandoos 1 localiza-se no norte de Omã, no distrito de Sohar, e foi descoberto em 2009 após campanha de prospeção geofísica (VTEM). Trata-se de um depósito oculto, coberto por gravilhas não consolidadas, possivelmente hospedado na unidade vulcânica *Alley*. A modelação tridimensional do depósito com o *software* MICROMINE revela um corpo mineralizado com 550 m de comprimento e largura máxima de 370 m, alongado segundo NW-SE e inclinado para SE; a sua espessura varia entre 1 e 90 m. O cálculo do volume da lentícula de minério aponta para um valor global de 1.8 milhões m^3 que, assumindo uma densidade média de 4.44 g/cm^3, resulta numa tonelagem de minério de aproximadamente 8 Mt com 1.72 wt% Cu. A modelação espacial da distribuição dos valores de concentração de Cu e Zn no depósito não colocou em evidência qualquer tipo de zonamento composicional relevante.

Em Mandoos, duas campanhas distintas de amostragem foram efetuadas: uma amostragem pontual levada a cabo pela Dra. Ana Jesus em 2015, ao longo da frente de exploração Este; e uma amostragem em sondagens cedidas pela Mawarid à Universidade GUtech. Destas amostragens resultou uma coleção de 42 amostras, 27 das quais referentes a minérios sulfuretados, 6 representando jaspes mineralizados, 5 documentando sedimentos metalíferos e 4 basaltos mineralizados. Todas estas amostras foram alvo de caracterização petrográfica e geoquímica detalhada com o intuito de contribuir com informações úteis à compreensão do depósito de Mandoos e ao estabelecimento de um modelo metalogenético coerente.

Os minérios associados a depósitos do tipo máfico são geralmente dominados por pirite, apresentando quantidades subordinadas de calcopirite e esfalerite. Tal é observado nos minérios texturalmente e mineralogicamente monótonos de Mandoos 1, os quais incluem ainda brechas cimentadas por sílica e

alguns filossilicatos. Os sulfuretos de ferro predominam (principalmente pirite), ocorrendo ainda calcopirite, esfalerite, algumas fases mais ricas em cobre e, raramente, galena. Por sua vez, as fases minerais constituintes da ganga correspondem maioritariamente a quartzo, filossilicatos e laumontite. Os minérios são relativamente pouco retrabalhados termicamente, permitindo a preservação de um grande número de arranjos espaciais primários, sendo bastante comum a presença de texturas framboidais e colomórficas, para além de icnofósseis tipo *polychetae* piritizados. A origem biogénica de texturas framboidais foi rejeitada, tendo esta sido esta atribuída à propriedade ferromagnética da greigite, precursor da pirite em texturas framboidais. As fases mais ricas em Cu (bornite, covelite e spionkopite) são correlacionáveis com os estádios mais tardios de mineralização, evidenciando um evento mais oxidante. Esta lentícula mineralizada é alimentada por um *stockwork* caracterizado por basaltos silicificados com disseminações de pirite e alguns veios preenchidos por pirite e calcopirite, não sendo evidente o desenvolvimento de uma rede anastomosada de veios mineralizados.

Texturas primárias de marcassite (colomórfica) e crescimentos de wurtzite em espaço aberto (e em contexto proximal de *black-smoker*) são observadas em algumas das amostras estudadas. Contudo, a coexistência de duas fases de ferro (pirite e marcassite) e de zinco (esfalerite e wurtzite) foi atribuída às variações físico-químicas abruptas que se podem fazer sentir, em poucos centímetros, nestes sistemas. Estas duas fases (marcassite e wurtzite) cristalizam preferencialmente em equilíbrio com soluções hidrotermais ácidas, sendo a mistura destas soluções com a água do mar responsável pelo aumento de pH que, por sua vez, conduz ao desenvolvimento das fases mais estáveis nessas condições (pirite e esfalerite)

Relativamente aos sedimentos metalíferos (*umbers* e *ochres*), estes evidenciam texturas sedimentares com alternâncias de bandas mais ricas ou empobrecidas em óxidos e hidróxidos de ferro. Adicionalmente, observam-se também pseudomorfoses de sulfuretos, completamente oxidados. Por sua vez os jaspes mineralizados apresentam abundantes disseminações de sulfuretos, sendo ainda cortados por veios selados por pirite e calcopirite. A formação dos jaspes foi interpretada como síncrona do evento evolutivo mais oxidante, responsável pela formação das fases mais ricas em Cu, enquanto a génese dos sedimentos metalíferos foi atribuída a eventos tardios de oxidação da lentícula mineralizada no fundo oceânico e/ou à precipitação de metais libertados para a coluna de água em contexto exalativo e ambiente oxidante.

Os dados de natureza geoquímica, mais precisamente a análise dos padrões de concentração normalizada de terras raras, sugere que a deposição dos minérios sulfuretados terá sido governada por misturas de água do mar e fluido hidrotermal, tal como nos jaspes, embora com proporções distintas. Os padrões obtidos para os sedimentos metalíferos (*umbers* e *ochres*) sugerem adsorção significativa de terras raras disponíveis na água do mar pelos filossilicatos constituintes dos sedimentos. As terras raras contidas nos minérios sulfuretados e nos jaspes deverão resultar da lixiviação dos basaltos a muro da mineralização, aquando da alteração hidrotermal. Os enriquecimentos em terras raras evidenciados pelas amostras de minério e jaspes podem ser alcançados com uma mistura de água do mar:basalto entre 0.85:0.15 e 0.99:0.01 para basaltos pouco alterados e entre 0.50:0.50 e 0.95:0.05 no caso de basaltos alterados. A modelação das magnitudes características dos fluidos hidrotermais de análogos modernos (TAG e EPR) podem ser simuladas com proporções entre 0.999:0.001 e 0.9999:0.0001, contudo a anomalia positiva em Eu e fracionação positiva em terras raras leves e pesadas típicas nestes fluidos não são completamente reproduzidas. Os enriquecimentos relativos em Cd, W, Sn, Te e In revelados por alguns minérios sulfuretados indicam a possibilidade do fluido hidrotermal mineralizante incluir uma contribuição magmática (episódica? e muito diluída), a qual pode ainda justificar outras diferenças composicionais observadas.

Palavras-chave: Ofiolito de Sumail, Omã, sulfuretos maciços, mineralogia dos minérios, geoquímica de rocha total.

Abstract

The modelling of the Mandoos 1 massive sulphide deposit revealed an orebody of ca. 8 million tonnes with an average grade of 1.72 wt% Cu. The spatial distribution of Cu and Zn concentrations suggests that the ores are relatively homogenous in composition and were not significantly affected by metal zoning refinement processes. The massive sulphide lens is mainly composed of iron sulphide rich (pyrite ± marcasite) breccias, cemented by silica ± phyllosilicates ± laumontite, having chalcopyrite (commonly altered to Cu-rich phases) and sphalerite as accessory minerals. The ores preserve large number of primary textures (colloform and framboidal) and also tubeworms (*polychetae*). The observed large amount of trace elements in the majority of mineral phases are consistent with the poor thermal reworking of the ores, also compatible with the monotonous and low diverse mineral assemblage. This Cu-rich VMS deposit is characterised by secondary Cu enrichment, developed during an oxidising event, which might also be synchronous of jaspers formation. When these sulphide ores were not covered, a seafloor weathering produced sequences of umbers and ochres with variable thickness, where massive sulphide breccias are oxidised and impregnated with silica in a more cold and oxidising environment, although these can also be formed by direct precipitation of metals within the water column, derived from exhalative discharges and deposited in such conditions. The REE normalised patterns of sulphide ores are consistent with a mixture of seawater and vent fluids (derived from basalt leaching – SW:B). The relative REE enrichments displayed by the ore samples can be simulated by a ratio of seawater (SW) and basalt (B) scattered between 0.85:0.15 and 0.99:0.01 for less altered basalts, while for altered basalts (B') the values range from 0.50:0.50 to 0.95:0.05. The same is observed in sulphide-mineralised jaspers, while the REE in umbers and ochres derives entirely from seawater. Present-day vent-fluids REE magnitudes (TAG an EPR) are simulated with SW:B and SW:B' interactions between 0.999:0.001 and 0.9999:0.0001. Nevertheless the pattern displayed by modern vent fluids, characterised by an evident Eu positive anomaly and positive LREE and HREE fractionation, is not completely reproduced by the performed simulation. Evidence of magmatic contributions to the hydrothermal mineralising fluid is supported by overall enrichments in Cd, W, Sn, Te and In; these contributions may also explain some other observed compositional differences.

Key-words: Sumail Ophiolite, Oman, massive sulphide, ore mineralogy, whole rock geochemistry.

Acronyms and Abbreviations

Geochemical Features			
Rare Earth Elements	REE	Suprasubduction Zone	SSZ
Light Rare Earth Elements	LREE	Moho Transition Zone	MTZ
Heavy Rare Earth Elements	HREE	Depleted Mantle Source	DMM
High Field Strenght Elements	HSFE	C1 Chondrite	C1
Large Ion Litophile Elements	LILE	Primitive Mantle	PM
Mid-Ocean Ridge Basalts	MORB	Back-arc basins basalts	BABB
Normal Mid Ocean Ridge Basalts	N-MORB	Forearc Basin	FAB
Enriched Mid Ocean Ridge Basalts	E-MORB	Island Arc Tholeiites	IAT

Minerals			
pyrite	*Py*	zeolite (group)	*Zeo*
chalcopyrite	*Ccp*	chlorite	*Chl*
sphalerite	*Sp*	quartz	*Qz*
marcasite	*Mrc*	hematite	*Hem*
wurtzite	*Wur*	carbonates	*Cb*
bornite	*Bn*		
galena	*Gn*		
laumontite	*Lmt*		

Geology- various			
atoms per unit formula	apuf	North East	NE
parts per million	ppm	South West	SW
weight percent	*wt%*	Volcanic Associated Massive Sulphide	VAMS
Whole-rock	WR	Volcanic Hosted Massive Sulphide	VHMS
X-ray fluorescence	XRF	Vulcanogenic Massive Sulphide	VMS
Wavelenght dispersive X-ray fluorescence	WDXRF	Iberian Pyrite Belt	IPB
Inductively Coupled Plasma Mass Spectrometry	ICP-MS	Massive Sulphide	MS
Polarized light	PL	Versatile Time-Domain Electromagnetic	VTEM
Reflected light	RL	Mandoos	MD
Plane polarized light	PPL	Back Scatter Electrons	BSE
Crossed polarized light	XPL	Seawater	SW
Million Tonnes	Mt	Basalt	B
Million years	M.y.	Altered Basalt	B'
Below Detection Limit	BDL	East Pacific Rise	EPR
		Trans Atlantic Geotransverse	TAG

Institutional			
Faculty of Sciences, University of Lisbon	FCUL	Sultan Qaboos University	SQU
Centre National de la Recherche Scientifique	CNRS	German University of Technology, Oman	GUTech

Others			
exempli graia/example	e.g.	*sensu strictu*/strict sense	*s.s.*
sensu lato/broad sense	*s.l.*	*Id est*/This is	*i.e.*

List of Figures

1. Introduction and Objectives

Oman, located in the southeastern coast of the Arabian Peninsula is bordered by the United Arab Emirates (northwest), Saudi Arabia (West) and Yemen (southwest). The geological relevance of the country comes mostly because of the largest and also the best preserved slab of upper mantle, oceanic crust and pelagic sediments in the world known as the Sumail ophiolite. A series of nappes were also emplaced along with the ophiolite; those thrust sheets comprise, from the bottom to the top, the Sumeini, Hawasina, and Haybi nappes, that were emplaced onto the Arabian continental margin between Coniacian and Campanian, during Neo-Tethys closure (Immenhauser *et al*. 2000).

According to Barrie and Hannington (1999), the volcanogenic massive sulphide deposits (VMS) hosted in ophiolitic sequences are classified as "mafic type" due to the predominance of mafic rocks. Deposits of this type are normally fewer in number, smaller in size, Cu-rich and Pb-poor when compared with other types of massive sulphide ores. In Oman, VMS deposits are mostly found in the northern part of the Sumail ophiolite, where the volcanic lava sequences are best exposed, and its exploitation goes back to the Bronze Age.

The Mandoos deposit was discovered in 2009 when the Mawarid Mining conducted a Versatile Time-domain Electro-Magnetic (VTEM) survey over an extension of wadi gravels in the north of Oman. Four first-order anomalies were identified in the region and the presence of massive sulphides was confirmed during a subsequent drilling survey. The Mandoos 1, Mandoos 2 and Mandoos 3 anomalies host massive sulphides but only the first includes Cu-mineralisation and tonnage economically viable for exploitation. The last anomaly (Mandoos 4) did not revealed the presence of orebodies of any kind (Mawarid Mining, 2014).

The Mandoos 1 deposit is located in the Sohar region and is hosted in massive basaltic lavas possibly related to the Alley volcanic unit. The mining operations started in October 2011 with extraction by open pit and lasted till early-2015, when all activities were abandoned due to economic issues. Underground exploration did not start due to problems with the local community. Engineers assessed a total mineral resource of 8 million tonnes of massive sulphides, with 5 million tonnes in reserves at 1.8% Cu (Mawarid Mining, 2014).

Samples for this study were obtained from *in situ* sampling and drill-cores picking from the assortment offered by the Company to the German University of Technology in Oman (GUtech). The main objective of this work consists on the mineralogical and geochemical characterisation of the Mandoos massive sulphide ores, by means of: (1) detailed re-logging of the drill-cores at GUtech; (2) petrography and detailed mineralogical studies with an Electron Probe Micro Analyser (EPMA); (3) whole rock multi-element geochemistry of a set of pre-selected samples from 2 different sampling surveys. All the petrography and analytical work was focused on massive sulphide samples (breccias), metalliferous sediments (umbers and ochres) and jaspers (mineralised). The numerical analysis and modelling of data mining assay for a large number of drill cores provided by Mawarid Mining further allowed assessing the vertical/lateral metal zonation in the orebody. The data and information collected represent a significant contribution to the establishment of a comprehensive metallogenetic model for the Mandoos VMS deposit.

2. Geological Setting

2.1 Regional Setting

In Palaeozoic times, Oman was part of the Gondwana (southern half of Pangea supercontinent), bordered by Paleo-Tethys to the north and east and by Panthalassa to the west. From Late Carboniferous to Early Permian all the eastern region of Oman was covered by a thick ice sheet as recorded by tillite deposits of the Hufq-Haushi area (Immenhauser *et al*. 2000). After that glaciation, a climatic warming result in lacustrine deposits in eastern Oman. The break-up of Gondwana led to the opening of two basins: the first rifting event separated the eastern Oman territory (Afro-Arabia) from northern Gondwana, called the early Indian Ocean-Batain basin; the second rifting event detached the northern Arabia territory from future parts of Eurasia, labelled as Neo-Tethyan Hawasina basin. The rift shoulder uplift and the simultaneous sea level rise led to the deposition of the Haushi Group sediments (shallow marine and fluvial) in the Early Permian. The subsequent global sea level rise and the thermal subsidence of the rift shoulders submerged the northern and eastern territories of Oman, resulting on the deposition of the Akhdar Group carbonates (Immenhauser *et al*. 2000). By the Middle-Late Permian, a large carbonate platform was established over Oman (Saiq Formation) and this sedimentation lasted until Aptian-Cenomanian. Outwards of the shelf carbonate platform, shelf slope carbonates from the Sumeini Group, proximal basin facies sediments from the Hawasina complex were developed. Two volcanic horizons, comprising alkaline-basalts and rhyolitic tuffs from Triassic, are preserved within the Saiq Formation (Haybi complex). Sedimentation along the Arabian platform ceased at the end of Cenomanian when the Aruma foreland basin was formed as a consequence of the passive margin contraction (Glennie *et al.*, 1973). In Upper Cretaceous (between Coniacian and Campanian times), the Sumeini, Hawasina, Haybi and ophiolite nappes were emplaced onto the Arabian platform. The Sumeini, Hawasina and Haybi complex are contemporaneous units preserving different, progressively more distal paleogeographic facies (Searle *et al.*, 2003), but are nevertheless commonly referred to, as the Hawasina nappes.

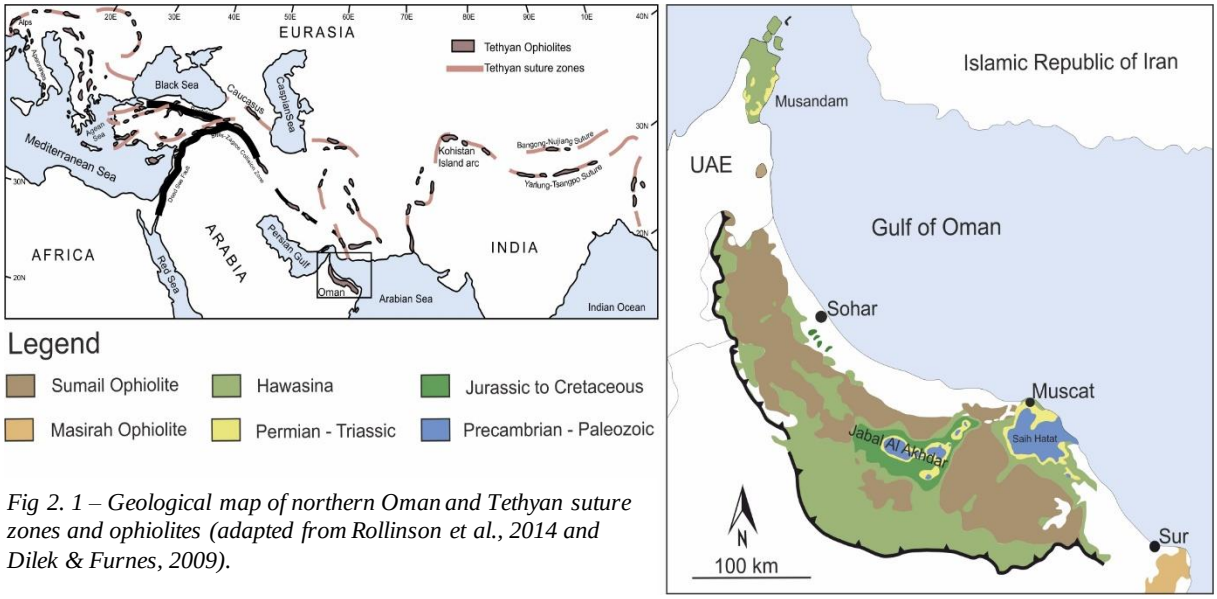

Fig 2. 1 – Geological map of northern Oman and Tethyan suture zones and ophiolites (adapted from Rollinson et al., 2014 and Dilek & Furnes, 2009).

2.1.1 Emplacement Models and Geodynamic Implications

The tectonic setting of the Sumail ophiolite is still open to discussion. According to various authors, the ophiolite was originated in a typical mid-ocean ridge environment while others propose a supra-subduction zone for its origin. The mid-ocean ridge model implies an obduction starting at the ridge; therefore, similar ages would be expected for the ophiolite units and the subduction zone footwall (metamorphic sole and Haybi complex), which is not the case (Searle & Cox, 1999). The Haybi complex is older than the ophiolite unit and records an oceanic-derived volcanism such as the Triassic alkaline (ankaramites, nephelinites) and tholeiitic basalts (Searle & Cox, 1999), as well as the Late Permian and Late Triassic limestone blocks and Cretaceous melanges. The amphibolites forming the metamorphic sole are compositionally distinct of the ophiolite volcanic rocks and the Haybi complex alkaline basalts display geochemical trends similar to those of the Haybi tholeiitic volcanic rocks (Triassic or Jurassic). Therefore, the ophiolite obduction could not have started at the mid-ocean ridge (Searle *et al.*, 1999); this is further reinforced by the similar dating of plagiogranites and metamorphic sole (Hacker, 1994), placing the subduction of Haybi complex basalts beneath the ophiolite at the same time of the ophiolite was developed during the Cenomanian-Tourian (Searle & Cox, 1999).

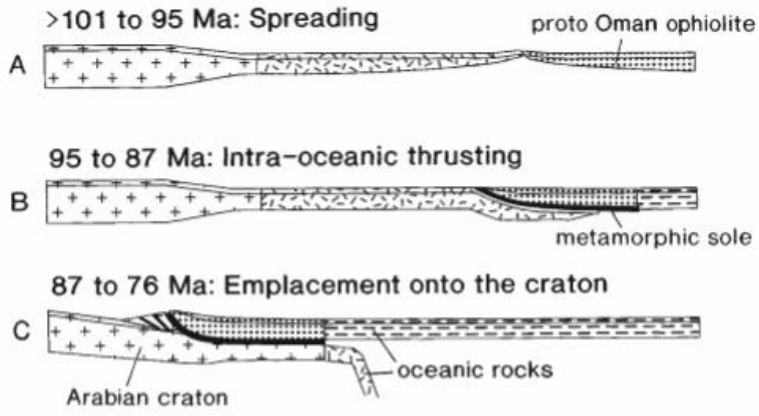

Fig 2. 2 – Emplacement model where the mid-ocean ridge is the starting point for the ophiolite obduction (in Searle & Cox, 1999)

The plausible setting where older and colder material could be in contact with hot-forming ophiolite rocks would be a transform-fault zone; however, clear evidence for that structural array is missing at Oman (MacLeod & Rothery, 1992). Searle & Cox (1999) reject both previous models for the tectonic setting that formed the Sumail ophiolite, which must have started above a northeast-dipping zone, away from the continental margin. The emplacement of the Sumail ophiolite began along with the Sumail thrust in a trench where older, colder ocean floor rocks (Haybi complex) were being subducted to the NE beneath the Sumail ophiolite, at the same time or right after the Sumail crustal sequence formation. Between 97-75 Ma the ophiolite was formed at a spreading centre above a northeast-dipping zone. The subduction of Haybi volcanic rocks reached 12-14 km below the Moho and their metamorphic recrystallisation achieved the upper amphibolitic facies conditions in a time span between 95-93 Ma (Searle & Cox, 1999). Those amphibolites formed the metamorphic sole and were welded to the base of the mantle sequence of the ophiolite. During burial processes, greenschist facies metamorphism affected the Haybi volcanic rocks, manganiferous cherts, exotic limestones, and shales, and they were welded onto the base of the amphibolites. All this sequence, ophiolite and metamorphic sole, was then emplaced onto the Arabian platform, reaching a distance of 350-400 km in a southwest direction (Searle & Cox, 1999).

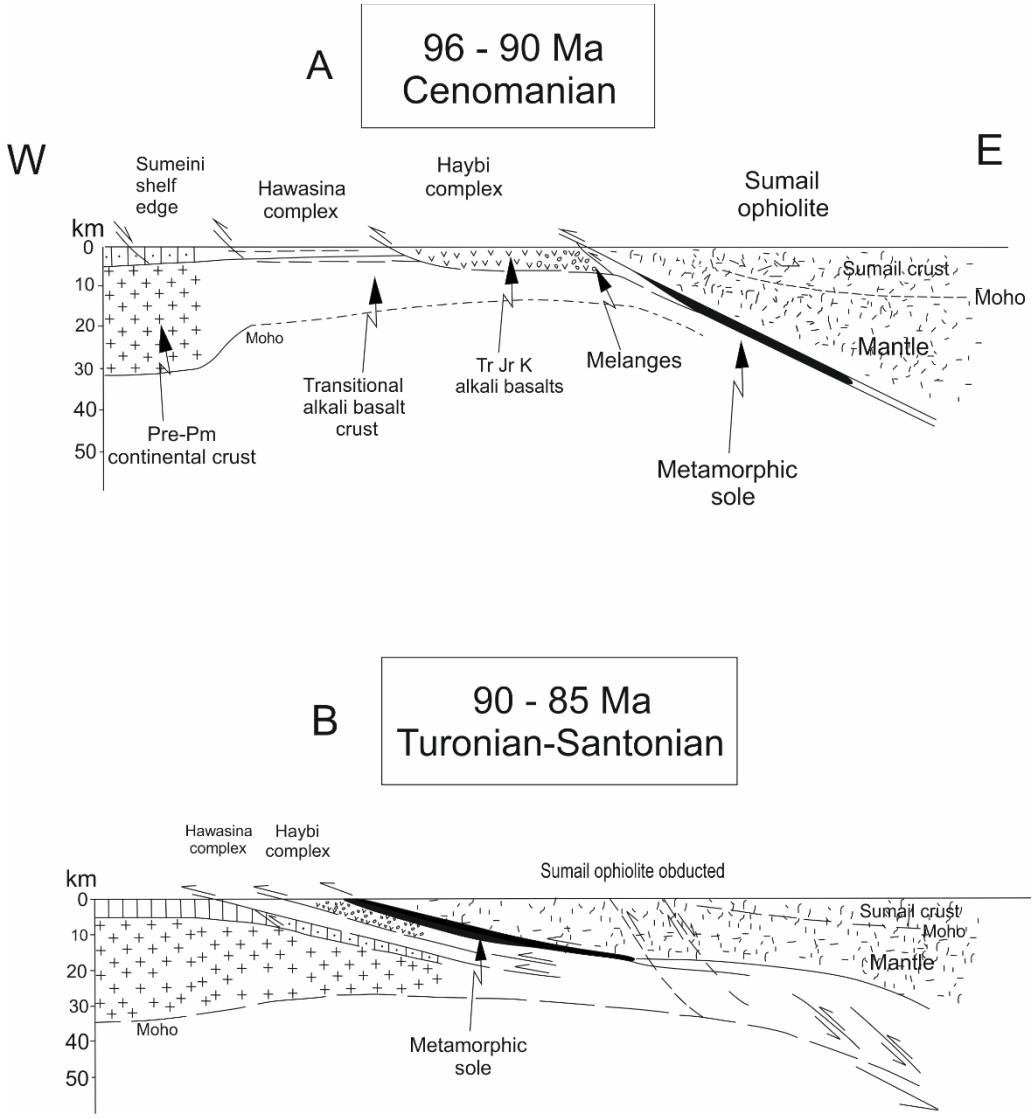

Fig 2. 3 – Model for the ophiolite obduction in the northern Oman showing; A – structural position of Sumeini, Hawasina and Haybi complexes before the emplacement; B – formation of the metamorphic sole (in Searle & Cox, 1999).

Paleo-depths of metamorphism were estimated from high-pressure metamorphic rocks presently located in the southeastern sector of the ophiolite. All the continental margin of the Oman Mountains was subducted to lower levels, in opposition to the central sector where no high-pressure metamorphic rocks are known. The deepest metamorphism is recorded by the As Sifah eclogites (garnet + clinopyroxene + glaucophane + phengite–bearing metabasalts and garnet + chloritoid–bearing metapelites) that were subducted to depths around 90 km. The eclogites occur within the Permian carbonated Saiq formation and evolved along a clockwise P-T path culminating at 20–23 ± 2.5 kbar and 540 ± 75 °C, suggesting that the continental crust was subducted underneath the ophiolite. Medium-pressure rocks are known in the northern part of the ophiolite from crossite- and glaucophane-bearing metabasalts in the north of Oman and high-pressure garnet amphibolites in the United Arab Emirates; however, in Bani Hamid area, the granulite facies point to P-T conditions of metamorphism of 6–9 kbar and 850 °C. In opposition to the Haybi complex that formed the majority of the metamorphic sole, the protoliths of granulites were quartzites and carbonates from the continental margin (Searle & Cox, 1999).

2.1.2 The Sumail Ophiolite

The Sumail ophiolite, also referred as Semail or Samail in the literature, has been recognised as the best preserved and largest slab of upper mantle, oceanic crust and pelagic sediments accessible on land. It was emplaced from NE to SW onto the Arabian passive continental margin, during late Cretaceous times due to the closure of the Tethys Ocean. With approximately 550 km long and 150 km wide (Searle *et al.*, 1999) the ophiolite belt comprises a complete section of the upper crust peridotites (8 – 12 km) and oceanic crust (4 – 7 km) (Lippard *et al.*, 1986), exposing a slice of oceanic lithosphere up to 20 km thick.

The typical oceanic lithosphere is entirely exposed in the Sumail ophiolite and its emplacement onto the Arabian platform did not result in significant structural dismembering; i.e., despite of regional doming and local thrusting, primary lithostratigraphic relationships are fairly preserved. It is believed that the oceanic nappe, along with several structurally underlying nappes, was emplaced in its present position (Glennie *et al.*, 1973).

The mantle sequence of the Sumail ophiolite is mainly composed of tectonised harzburgite, originated by partial melting of fertile primary spinel lherzolite (Searle *et al.*, 1999). Below the Moho, high temperature mineral lineations formed due to the plastic flow during mantle upwelling and diverging away from the ridge. Mineral fabrics originated during the ophiolite emplacement overprint these early mantle fabrics along the base, as evident in a strongly banded harzburgite-lherzolite-dunite basal unit. The appearance of plagioclase marks the petrological Moho, where dunite pods with small chromite-rich lenses occur (Searle & Cox, 1999).

The oceanic crustal section of the ophiolite is composed of cumulate gabbros overlain by isotropic gabbros which are intruded by diorites and trondhjemites; some discordant wehrlites can intrude higher levels of the crustal sequence. A sheeted dyke complex outlines the main pathways that fed the extrusive pillow lavas (Searle & Cox, 1999). Up to 2 km of lavas form the upper sequence of the ophiolite, outcropping mostly in northern part of Oman. The volcanic sequence can be subdivided into different units depending on the authors, resulting in a maximum of five major units (Alabaster *et al*, 1982; Gilgen *et al.*, 2014), as addressed below.

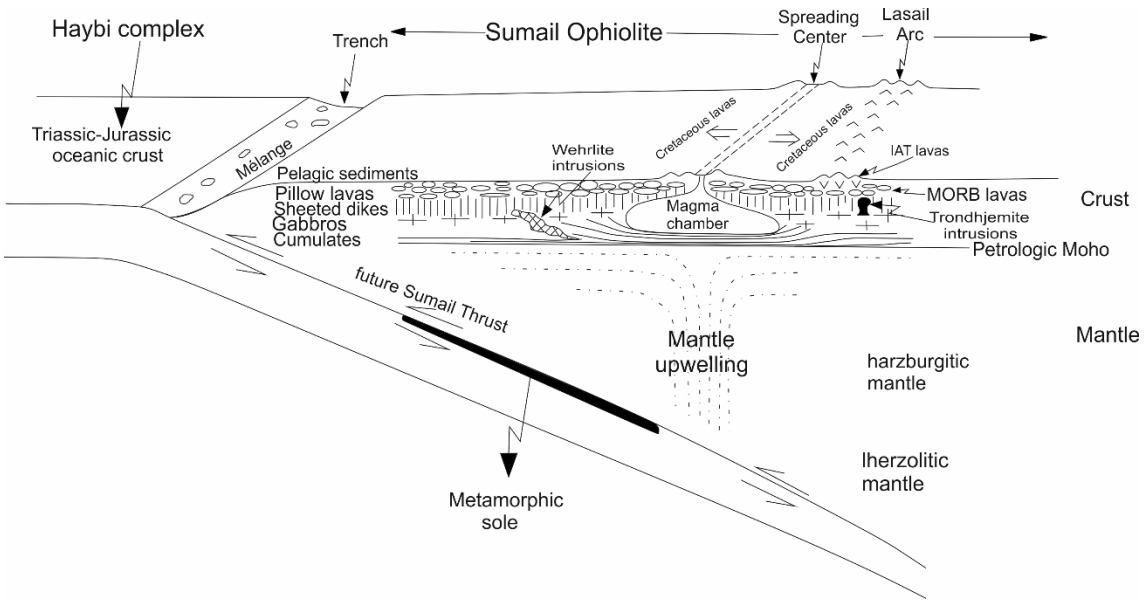

Fig 2. 4 – Subduction-zone emplacement model showing the internal structure of the ophiolite (in Searl & Cox, 1999).

2.1.3 Volcano-stratigraphic Sequence

As aforementioned, the upper section of the ophiolite nappe is composed of up to 2 km of pillow lavas covered by up to 30 m of pelagic sediments containing microfossils of Cenomanian to Turonian age (Gilgen *et al.*, 2014). U-Pb zircon ages of trondhjemites from many different levels along the ophiolite section fall in the time window from 97.3 to 94.4 Ma (Rollinson, 2009). Those ages, considered together with micropaleontology data gathered from pelagic sediments interbedded in the lavas, allow inferring that the seafloor volcanism was active during ca. 10 m.y. (from ca. 98.9 to 89 Ma). According to Searle and Malpas (1982), it took 3 to 7 m.y. from the volcanism cessation until the ophiolite obduction; other authors assume that the time span was even shorter, from 1 to 2 m.y. The Sumail ophiolite lavas form a defined set of volcano-stratigraphic units presumably derived from overlapping volcanic centres at spreading axes and, thereafter, at off-axis locations (Gilgen *et al.*, 2014). Five lava units were distinguished by Alabaster *et al.* (1982) according to field, petrological and geochemical characteristics; these are labelled as Geotimes, Lasail, Alley, Clinopyroxene-phyric, and Salahi.

Geotimes is the lowermost unit of the extrusive volcanism; it lays directly on top of the sheeted dyke complex and can vary between 0.75 and 1.5km in thickness (Alabaster *et al.*, 1982; Lippard *et al.*, 1986). These lavas can be recognised in the field considering: (i) the common occurrence of tubular pillows instead of massive flows; (ii) the scarcity of amygdule and variole-rich textures; and (iii) the typical reddish-brown colour due to the widespread, fine-grained hematite dissemination and hematite-rich inter-pillow hyaloclastites. They are slightly depleted in incompatible trace elements when compared to N-MORB basalts, along with negative anomalies of Nb and Ta (Godard *et al.*, 2003)

The Lasail unit overlies, at least locally, Geotimes. According to Alabaster and Pearce (1985), the Lasail unit is restricted to some areas, being interpreted as a product of off-axis volcanism. However, following Kusano *et al.* (2012), the Lasail unit is inter-fingered with Geotimes and can be simply envisaged as a subunit of the latter. It consists of grey to pale green basaltic to andesitic pillow lavas that can vary from 0 to 0.75 km thick (Lippard *et al.*, 1986); the typical green colour is due to the relative abundance of epidote and chlorite. Geochemically, the Lasail lavas are depleted in both light rare earth elements (LREE) and incompatible elements when compared to N-MORB basalts (Godard *et al.*, 2003).

The Alley unit lies on top of both Geotimes and Lasail, and comprises grey and brown pillowed and massive flows, as well as basalt breccias; this unit can vary from 0.75 to 2 km in thickness. The 2 to 3 meters of pillows are characterised by abundant amygdule filled with zeolites and celadonite, besides glomerophyric clusters of clinopyroxene (Alabaster *et al.*, 1982; Lippard *et al.*, 1986). The Alley and Lasail lavas share a similar normalised pattern for rare earth element (REE), although the concentration in LREE is slightly lower in Alley lavas. These two units can be also differentiated on the basis of Zr and Cr contents (Lippard *et al.*, 1986).

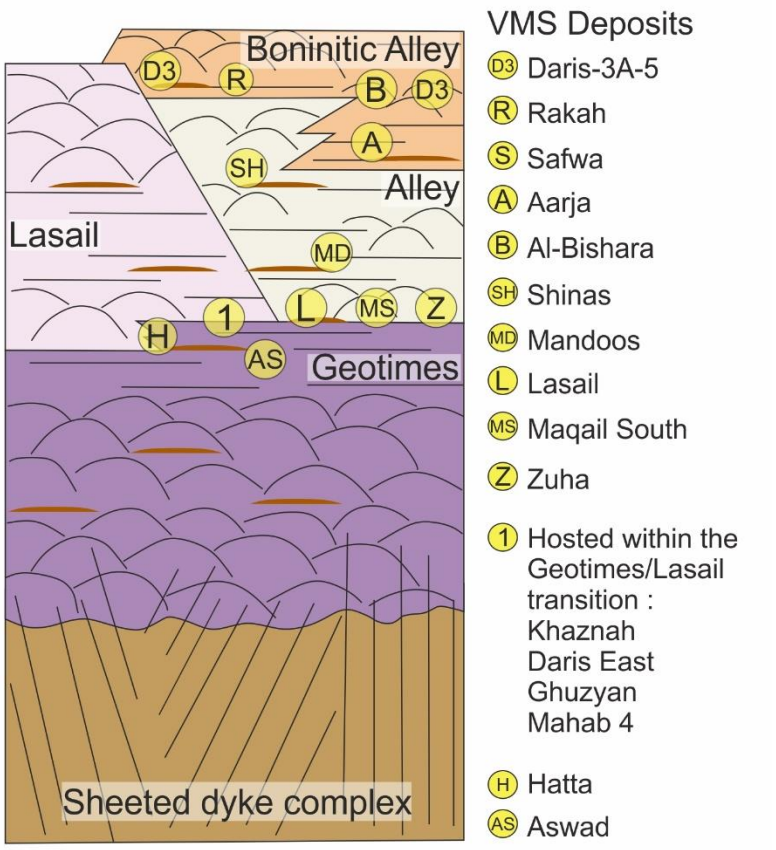

Fig 2. 5 – Schematic representation of the volcano-stratighaphic sequence of the northern Oman illustrating also the position of some VMS deposits (adapted from Gilgen et al., 2014).

Overlying these three volcanic units, some small-volume basaltic flows with abundant clinopyroxene phenocrysts are found, belonging to the Clinopyroxene-phyric unit; these lavas area characterised by lower Zr and Ti contents but higher Cr grades (Alabaster *et al.*, 1982; Lippard *et al.*, 1986). The Salahi unit consists of alkaline to transitional within-plate lavas (Alabaster *et al.*, 1982). These two latter units are restricted to specific areas and they are not found anywhere else besides the outcrops reported in Alabaster *et al.* (1982); both units are not associated with any sulphide mineralization (Gilgen *et al.*, 2014). Some boninitic outcrops show a spatial relationship with Alley lavas. Those lavas have regional meaning but it is not clear if all the occurrences are limited to just one stratigraphic unit; they usually occur as vesicular pillows and sheet flows, reaching several meters in thickness, with (micro)phenocrysts of orthopyroxene, clinopyroxene, olivine, and chrome-spinel (Gilgen *et al.*, 2014). Some boninitic dykes found in the Shinas mine are younger than the Alley lavas, suggesting that their development and emplacement took place, at least in some areas, after the Alley unit.

2.2 VMS Deposits

Volcanogenic Massive Sulphide (VMS) deposits precipitate from hydrothermal fluids and form stratiform accumulations of sulphides at sea floor level. Commonly associated with volcanic rocks, this type of deposits represent an important source of Cu, Zn, Pb, Au, and Ag along with Co, Sn, Ba, S, Se, Mn, Cd, In, Bi, Te, Ga, and Ge as co- or by-products. The study of active, metal-precipitating hydrothermal vents on the sea floor has been the key factor to understand the land-based VMS deposits formation (Barrie and Hannington, 1999).

A five-fold classification is commonly used to describe most of ancient and active VMS deposits. This classification is mainly based on the composition of the host rocks, assuming that the metals in sulphide ores derive mostly from leaching and scavenging of a footwall substrate. The main five types of host rocks composition where the classification is rooted are: mafic, bimodal-mafic, mafic-siliciclastic, bimodal-felsic, and bimodal-siliciclastic (Barrie and Hannington, 1999).

The "mafic type" is defined by the larger predominance of mafic rocks on the hosting stratigraphic sequence given the rare or even absence of felsic rocks, although minor siliciclastic or ultramafic rocks can be present. Ophiolites are one of the settings classified as mafic and most of the examples from this type are exclusively Phanerozoic in age. Ocean ridges, advanced back-arc rifts and supra-subduction spreading zones are the common settings where modern analogues of this type are found. The basaltic host rock is predominantly tholeiitic, with some local boninitic occurrences. Mafic VMS deposits are normally fewer in number, smaller, Cu-rich and Pb-poor in comparison with the other massive sulphide deposit types (Barrie and Hannington, 1999).

The "bimodal-mafic" type is characterised by having more than 50% of mafic rocks and a low percentage (> 3%) of felsic ones in the hosting sequence; the mafic/felsic ratio is 3:1 or greater, but felsic volcanic rocks are usually the nearest host rocks. The composition of the volcanic host rocks points to primitive volcanic arcs or rifted primitive volcanic arc settings. Mafic rocks are usually basaltic and tholeiitic (can be transitional to calc-alkaline), while felsic rocks have a rhyolitic composition or transitional with calc-alkaline rhyolites. Noranda (Quebec) and Kidd Creek (Ontario) are the two main examples of this "bimodal-mafic" type, although Kidd Creek is atypical due to its ultramafic footwall.

The "mafic-siliciclastic" VMS type has identical proportions of mafic or intrusive rocks and siliciclastic (turbidites); in this VMS type, felsic rocks occur in small amounts or may even be absent from the hosting sequence. The Besshi deposit in Japan is one land-based example of this VMS type, similar to the VMS occurrences in the rifted continental margin in the Gulf of California, the Middle Valley rift, or in the Escanaba trough at the northeast Pacific Ocean, or in the Atlantis II deeps of the Red Sea.

The "bimodal-felsic" VMS type is characterised by a higher content of felsic volcanic rocks (>50 %) in comparison with siliciclastic rocks (<15 %) in the volcano-stratigraphic hosting sequence; mafic rocks usually complete the hosting sequence. Like in "bimodal-mafic" VMS deposits, deposits hosted in "bimodal-felsic" sequences share the same age distribution, but are more abundant in Phanerozoic times, usually related to more compositionally mature volcanic arcs, or rifted volcanic arc settings than the "bimodal-mafic" VMS types. High-silica rhyolite compositions are common in the felsic host rocks with calc-alkaline to transitional affinities, while the mafic rocks comprise calc-alkaline or transitional tholeiitic to calc-alkaline rocks. This VMS type contains, in average, higher contents of Zn and Ag in comparison with all the other VMS types (Barrie and Hannington, 1999).

The last type of VMS deposit is the "bimodal-siliciclastic" which has equivalent proportions of volcanic rocks (usually felsic rocks are much more abundant than mafic) and siliciclastic rocks. These deposits are usually found in belts of Phanerozoic age (like the Iberian Pyrite Belt, Portugal and Spain). Some authors refer that the felsic volcanic hosting rocks are generally calc-alkaline; however, this compositional feature is usually due to crustal assimilation and that is consistent with continental arc or rifted continental arc settings. Tholeiitic basalts are the common mafic rocks in this type of VMS deposit, however there are exceptions like in the Iberian Pyrite Belt where alkaline basalts are found in higher levels of the stratigraphic sequence. The "bimodal-siliciclastic" VMS deposits have the lowest contents in Cu and the highest in Pb, but are the largest in size in comparison with all the remaining VMS types (Barrie and Hannington, 1999).

2.2.1 Ophiolite-Hosted Volcanogenic Massive Sulphide Deposits

Ophiolite-hosted VMS deposits are "mafic type" deposits, also commonly referred as Cyprus type, normally displaying a shape similar to those modern analogues found in massive sulphide mounds. They often display an elongated shape instead of equidimensional, reflecting the strong structural control set by fault zones in hydrothermal-mineralising venting. The footwall contact has usually a concave shape, while the hanging wall is flat, outlining a long-term exposure on the seafloor that tends to flatten the upper surface of the massive sulphide deposit. The massive sulphide lens formed along half grabens or adjoining listric fault zones are usually thicker in one flank and thinner towards their width. The lens comprises breccia and pyrite sands, covered by Fe-rich oxidized sediments (ochres) (Galley & Koski, 1997).

The root of most of massive sulphide deposits goes tens of meters below the paleo seafloor where a discrete stockwork cuts the basaltic host rock and promotes the long-lived flow of hydrothermal(-mineralising) fluids responsible for the observed alteration halo (chlorite-quartz-pyrite). The sulphide stockwork is composed of small and irregular, anastomosed veins/veinlets in a chlorite-quartz groundmass (lower part) but, below the massive sulphide lens, the veins increase in size giving rise to *in situ* breccias. Recurrent rejuvenation of permeability, due to cyclic build-up of fluid pressure, promotes the development of spaces than can be filled with sulphides, forming small massive sulphide lenses. In the upper stockwork, basalts are silicified whereas at the base of some ore lenses sulphide-quartz breccias may develop (Galley & Koski, 1999).

There is a gradual contact (several meters) between the stratiform massive sulphide lens and the top of the stockwork, where the veins coalesce to form the massive sulphide lens leaving altered basalt fragments isolated and almost indistinct towards the core of the lens. Those orebodies are normally massive, made up of fine-grained granoblastic to idiomorphic pyrite, with abundant vuggy cavities lined by idiomorphic pyrite. Veins of colloform to sandy sulphides cut the massive sulphide that appears more brecciated upwards. The blocks (cemented by "sandy" sulphide) are normally colloform banded sulphide; however, some blocks of chalcopyrite aggregates are present in a matrix of pyrite and quartz. These blocks might correspond to fragments of high temperature sulphide chimneys; some worm burrows (tube-worms) were identified indicating that some of the breccias might correspond to sulphide chimneys. The sulphide lenses become less consolidated towards the top and are commonly covered by layered Fe oxides sediments (ochres) composed of goethite, natro-jarosite, jarosite, hematite, maghemite and magnetite; these sediments may include some interlayered graded beds of "detrital" sulphide and tend to be confined to direct contact with the massive sulphide lenses whereas jaspers (commonly radiolarian-bearing) are not so restrict. The jaspers are thought to be formed from pelagic and hydrothermal chemical-sediments while ochres from *in situ* weathering of the underlying sulphide, although some authors suggest that this type of Fe-oxide deposits are formed from subaerial weathering (Galley & Koski, 1999).

Pyrite is the main sulphide mineral in this type of ores, being chalcopyrite and sphalerite the second most abundant sulphide minerals. These deposits can also include marcasite, cubanite, covellite, bornite, digenite, chalcocite, galena, pyrrhotite, idaite, bravoite, carollite, and mackinawite, with minor amounts of magnetite and hematite. The most common gangue components are quartz and gypsum. Referring to the ochre caps, these include goethite, jarosite, amorphous oxides, hematite and rare native gold. The veining system of the stockwork consists mainly of pyrite and quartz-pyrite, being the pyrite present in disseminations throughout the chloritized and silicified host lavas; it is in these silicified zones that the chalcopyrite veins are mostly concentrated. Pyrite in pyrite veins are commonly fine-grained granoblastic to idiomorphic (with small amounts of chalcopyrite and sphalerite forming inclusions and fracture infillings) while in quartz-pyrite veins, the sulphide is usually corroded and replaced by quartz

and/or chalcedonic silica, being the latter more common at the top of the stockwork. In general, the mineral assemblage forming the base of the lens is pyrite-silica breccia, where pyrite and chalcopyrite are surrounded and partially replaced by silica. On top, a massive pyrite facies of fine-grained (idiomorphic to subhedral) pyrite; this pyrite is commonly zoned, with inclusions of pyrrhotite, chalcopyrite, magnetite, cubanite and Fe-rich sphalerite (Galley & Koski, 1999). Colloform banded veins commonly cut the base of the massive pyrite, although these colloform textures are more abundant in the breccia zone. The colloform veins and rims are composed of interlayered pyrite, marcasite, chalcopyrite, sphalerite, and quartz, where chalcopyrite veining increases towards the top of the lens. Covellite, chalcocite and digenite are secondary copper minerals and are mostly present below the Fe oxide ochre cap, although they can be found in the entire orebody replacing chalcopyrite (Galley & Koski, 1999).

2.2.2 VMS Deposits in Oman

Volcanogenic massive sulphide deposits are mostly found in the northern part of the Oman Mountains, within the volcanic lavas sequence. Early evidence of mining is from the Bronze Age and Islam rise, mostly focused on secondary copper minerals found below strongly oxidised (superficial) caps (Lippard *et al.*, 1986). Lasail, Bayda and Aarja in the Sohar district were the first mines where primary chalcopyrite-bearing massive sulphides were exploited between 1983 and 1993; Lasail was the largest deposit, producing 9.2 Mt of ore at 1.42 wt% copper. From 1994 to 2005, the iron-hats of Yanqul were mined for gold, but since 2000 many important discoveries have been made, and Hatta, Shinas, Safwa and Mandoos were mined by Mawarid Mining L.L.C.

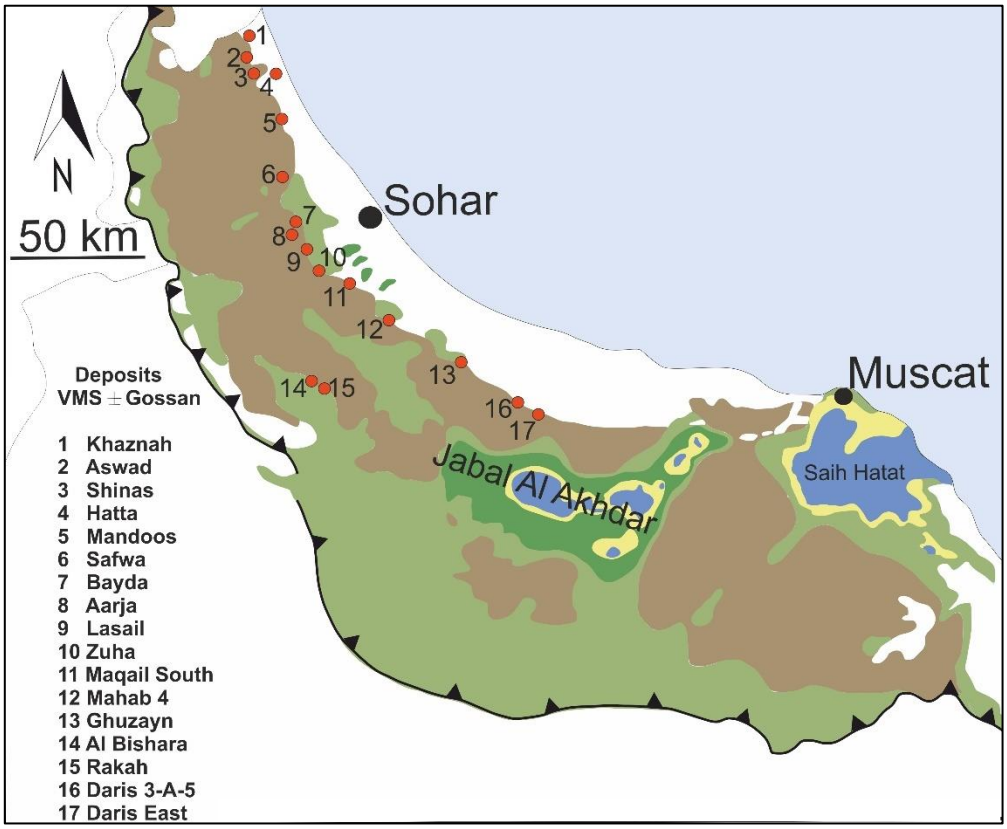

Fig 2. 6 – Simplified geological map displaying the location of a large number of deposits within the volcanic units represented as in figure 2.1.

The 50 Mt total tonnage of the Sumail deposits are not comparable with other VMS districts around the world (Franklin *et al.*, 2005) but is in the same range indicated for the Troodos ophiolite VMS deposits.

The Geotimes/Lasail contact and to a lesser extent the Geotimes/Alley contact were thought to be the main ore horizons, corresponding to the paleo-seafloor where the sulphide mounds were formed; however, some of the later discoveries do not fit this simplified model of occurrence (Gilgen *et al*, 2014).

2.2.3 The Mandoos Deposit

There are no published data about the Mandoos 1 deposit, and the following information was gathered from a Mawarid Mining unpublished report. The Mandoos area (Fig 2.7), more specifically the Mandoos 1 deposit area, is covered by unconsolidated wadi gravels (8 to 34 m) and there are no signs of volcanic rocks exposures; they only occur 2 km along strike to the north and south, and indications provided by the regional geological mapping show that the volcanic sequence dips to the east. The Mandoos 1 ores occur intra-Lasail or Alley volcanic units, although the relatively high magnetisation of the host rock favours the latter unit. Such differences in magnetic properties of the two volcanic units derive from the relative amount of igneous iron-oxides in the lavas, thus providing characteristic magnetic signals. The geology of the deposit was inferred from drill-holes and logging, showing that the massive sulphide in the Mandoos 1 prospect spreads over 60 m thick in the northern part, which is interpreted as an evidence of a topographic-low or an asymmetric-graben infilling; a strong structural control of ore deposition and accumulation is suggested due to the significant thickness decrease of the lens towards north, east and west.

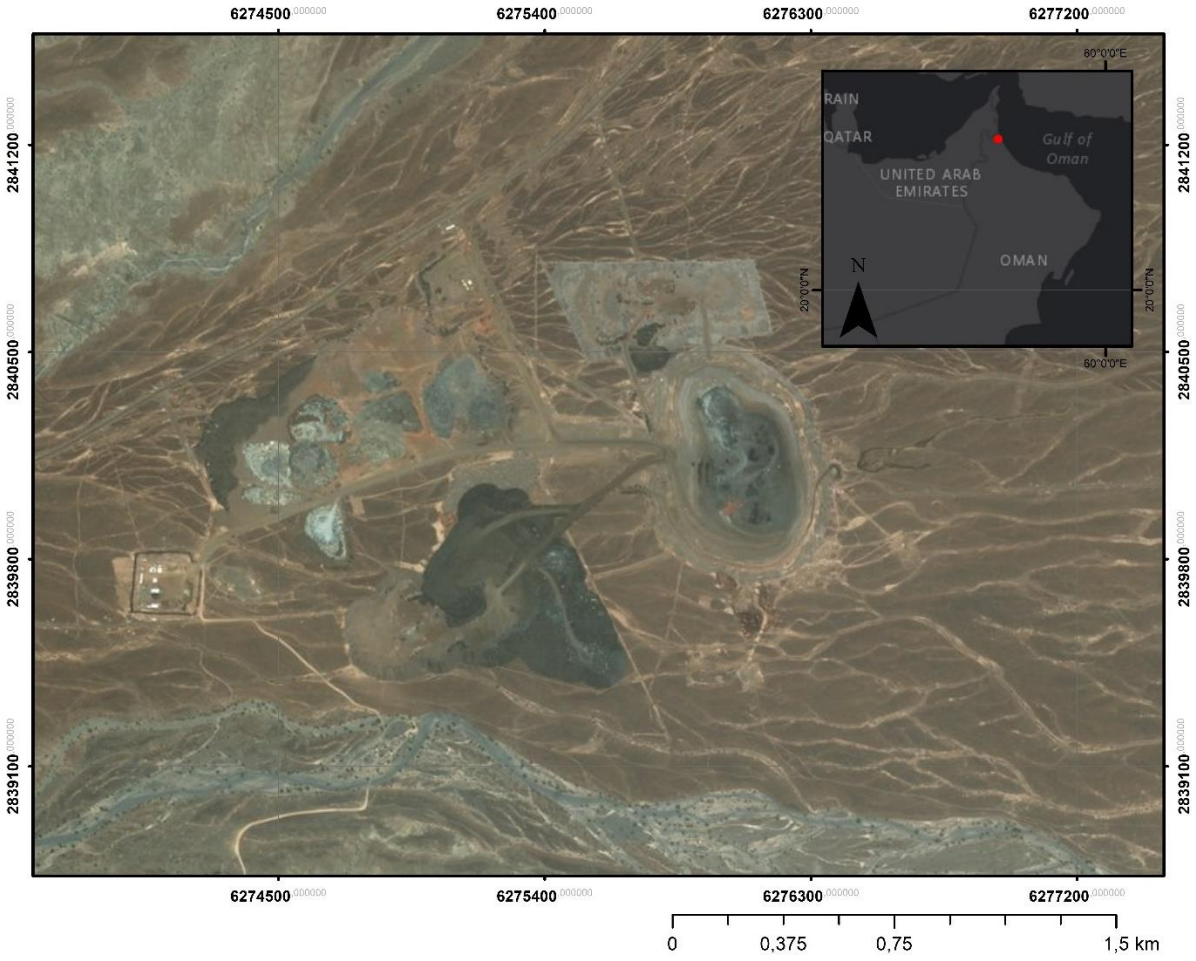

Fig 2. 7 – Location of Mandoos 1 open pit (ArcGIS).

The massive sulphide lens (Fig 2.8) is hosted in massive basaltic lavas with some minor pillow lavas occurring on its footwall. The contact of the massive sulphides and the upper lavas is traced by a red-

brown umber layer. A gossanous zone is also present where the lens was exposed to weathering, mostly in the transition from the mineralised volcanic rock and the unconsolidated wadi gravels.

As in most of the ophiolite-hosted deposits, pyrite is the dominant sulphide in Mandoos 1 deposit, with minor chalcopyrite and sphalerite. Chalcopyrite normally concentrates in the upper levels of the massive sulphide lens, and the higher copper grades together with some anomalous contents of Au, Ag and Zn outline the transition zone towards the iron-hat cover, strongly suggesting the progression of late (supergene?) enrichment processes. In the footwall of the lens there is a clay-silica-pyrite alteration zone, which appears to be more extensive towards the north and west and thin towards the south. The ore in this deposit can be subdivided in three types: (i) the massive sulphide zone that comprises more than 90% pyrite and late-formed chalcopyrite; (ii) the silica massive sulphide zone that occurs only in short (and discontinuous) intersections; and (iii) the stockwork hosted in a silica-clay altered basalt placed below the central part of the lens and showing a pyrite-quartz-jasper association, usually poor in copper.

Many different diachronic alteration events are recorded. Hematite-rich alteration is preserved in basalts showing also evidence of carbonate alteration as veinlet infillings preceding the main mineralising event. As referred before, the transition zone between the massive sulphide lens and the gossan cover is where the higher grades of copper are found; that enrichment is mostly due to the alteration of chalcopyrite to chalcocite, bornite and covellite. Synchronous with the massive sulphide formation a chlorite (+quartz) alteration occurs and is best seen along the "chilled margins" in pillow lavas.

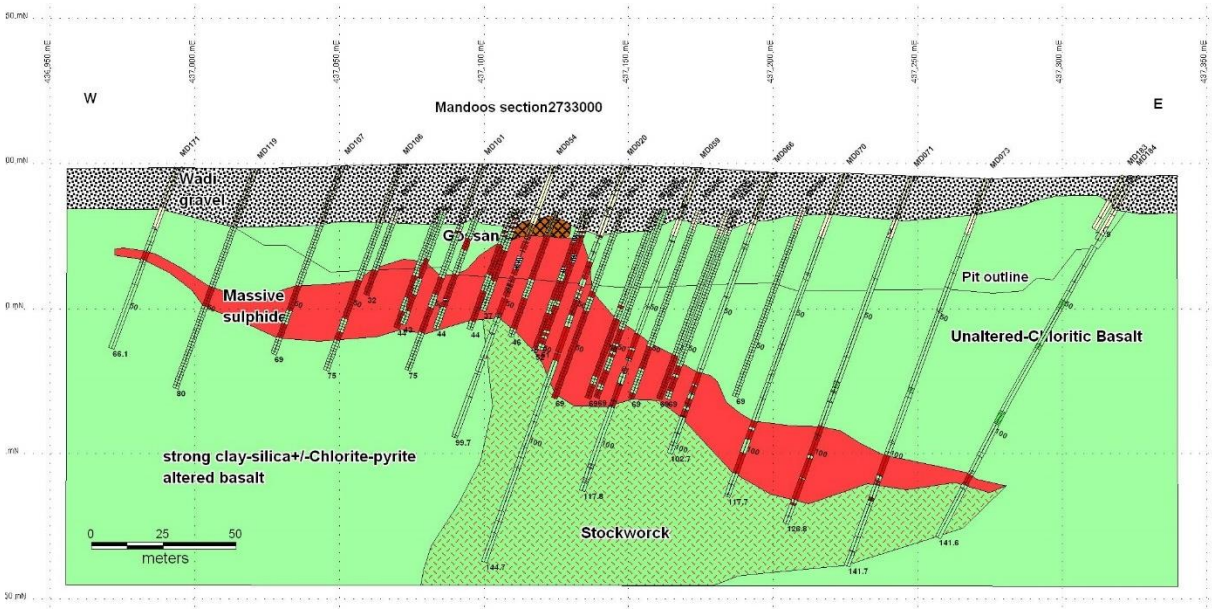

Fig 2. 8 – Cross-section of the ore body showing the relative position of the stockwork and the gossan cover (Mawarid Mining, 2014).

3. Methodology

3.1 Sampling

The sampling survey comprised two different phases. The first one took place throughout the east-wall of the Mandoos Mine open pit, granted to the Mawarid Mining Company; the second phase involved six drill-cores provided by the same company, after their previous re-logging.

The sample labelling distinguishes the survey phase. Samples from the open pit were labelled with MD, initials for Mandoos, followed by the profile reference (P1, P2, P3 and P4) and sample number. Labels of drill-core samples comprise the original reference given to drill holes and the depth where the sample was collected, besides the MD initials.

The first sampling phase was performed by Dr. Ana Jesus in May 2015 and includes samples from the massive sulphide orebody and metalliferous sediments. This discrete sampling programme along the east-wall of the open pit (from the central part of the deposit towards south) allowed collecting 24 specimens (Appendix I).

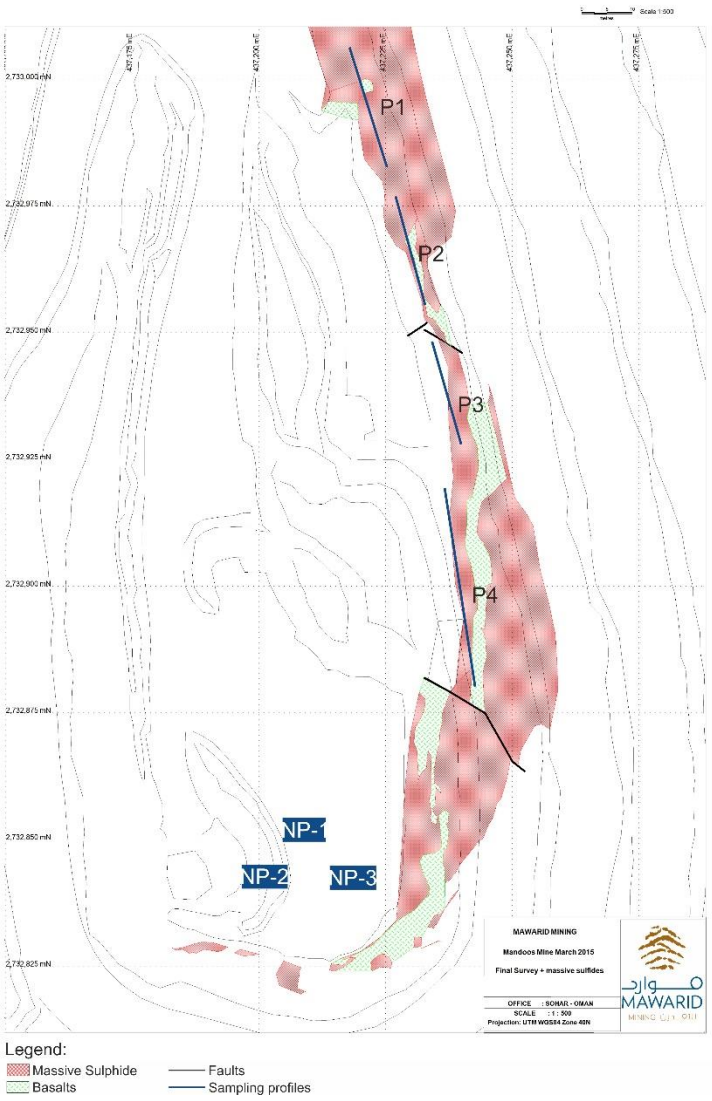

Fig 3. 1 – First sampling survey along the open pit east wall, illustrating the location of the 4 sampled profiles and some other collected samples.

The second phase of the sampling survey was performed in March, 2016. The selected six drill holes are not restricted to the ore body exposed in open pit, and embrace outskirt domains of the mineralised area as illustrated in Figure 3.2. According to the available data, cores from drill hole MD174 should represent the north-western part of the ore body, while those from MD150 and MD178 should characterise its central domain; samples from MD429, MD430 and MD431 drill holes represent the south-estern part of the deposit, outside the open pit. The sampling programme was targeted to intersected segments of the ore lens, embracing cores of massive sulphide segments, mineralised jaspers and metalliferous sediments (umbers and ochres). Due to the poor core preservation, the spatial representativeness of sampling might be compromised in certain parts of the section; indeed, the majority of ore segments in drill holes display evidence of significant crumbling and/or variable mingling, or show effects of strong weathering, being covered by sulphate crusts of irregular thickness. The best approach was to collect all the well-preserved and less-altered specimens throughout the six drill cores, totalling 18 samples and resulting in a combined collection of 42 samples: 27 of massive sulphides, 6 of mineralised jaspers, 5 of metalliferous sediments and 4 of a mineralised silicified basalt.

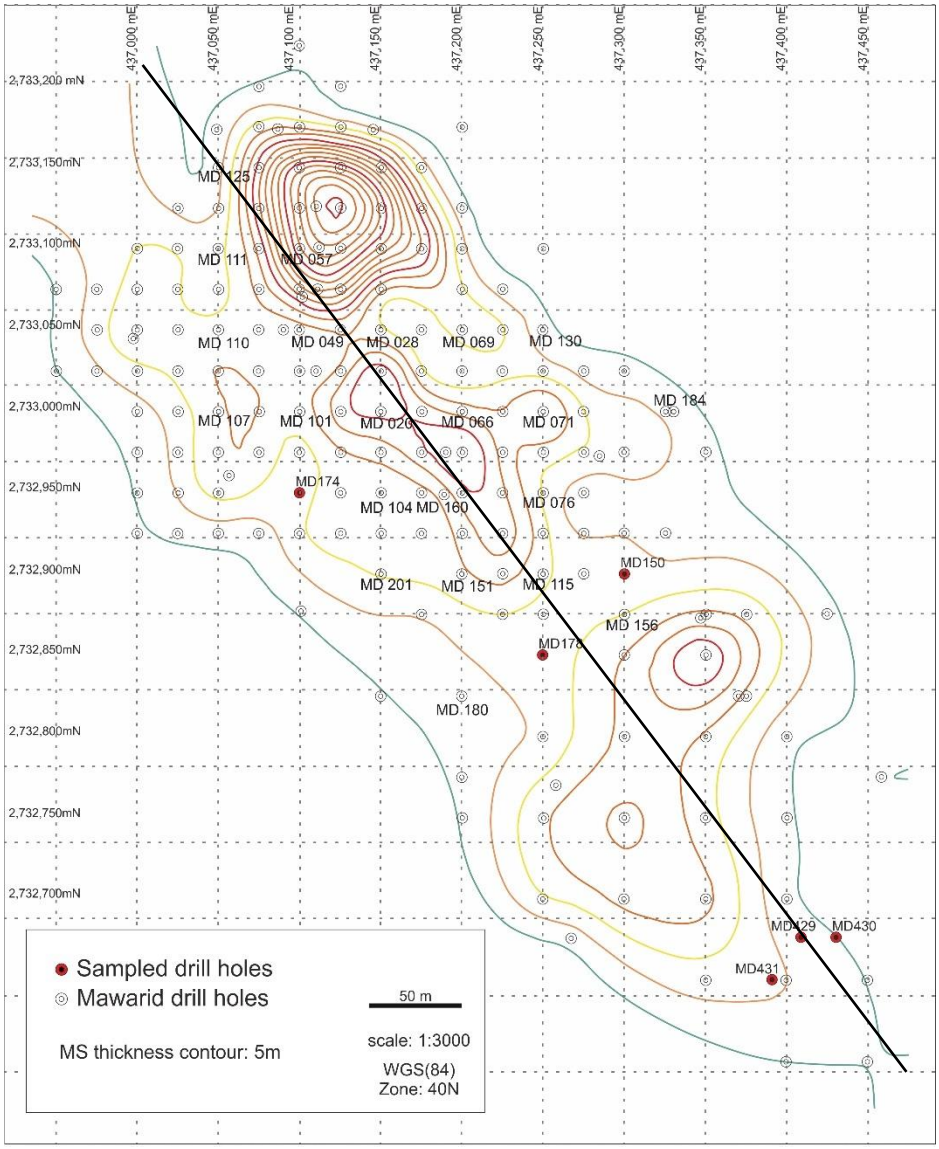

Fig 3. 2 – Drill holes location at Mandoos 1; the red mark represents the drill holes sampled in this work (second survey); information from drill holes marked with the reference was used in the modelling exercise. Black line represents NW-SE cross section. shown in Fig 4.4, 4.5 and 4.6.

3.2 Sample Preparation

Sample preparation took place between May and September, 2016, using the facilities available at the Sultan Qaboos University (SQU) and the Faculty of Sciences of the University of Lisbon (FCUL). The first steps of sample preparation were made in SQU due to the impossibility to export rock samples out of Oman.

3.2.1 Thin and Polished Sections Preparation

A large number of polished thin sections and mounts were made, according the usual procedures, as follows:

a) The samples were cut with a diamond saw considering the surface chosen for further petrographic analysis; the slabs should get the size to fit the glass for thin sections, or to fit the mounts cup.
b) Mount samples were placed into cups, further filled with epoxy resin and then placed into a vacuum chamber hoven for resin settling.
c) To prepare thin sections, the slabs were glued onto unpolished glasses; slab surfaces were previously flattened in an automatic plate using 600 *mesh* silicon carbide powder. After being glued, the samples rested in a heated press for resin settling.
d) All the thin section samples were trimmed with a diamond precision saw, and only about 0.5mm thick of rock was left glued on the glass.
e) The lapping is one of the critical steps to get good results before polishing, and this process differs for thin sections or mounts. For thin sections the mechanism is completely automatic but the good results will depend on the good calibration of the machine. The samples were placed on a jig and the lapping was done in a plate using 600 *mesh* silicon carbide powder until the thickness of a bit more than 30 μm was reached. The lapping of the mounts was completely handmade, involving a sequence of steps to decrease the grid size and to get the best surface to polish. It started with a 220 *mesh* diamond plate followed by the 600 *mesh* diamond plate. After the diamond plate the samples were lapped on a glass surface using silicon carbide powder, starting with 800, then 1000 and finally 1200 *mesh*.
f) The other critical step is the polishing; it was done automatically but, like the lapping, a precise calibration was critical for good results. Both sample types, thin sections and mounts, were polished using the same method. They were polished using a cloth plate impregnated with diamond paste and lubricant. A series of different grain size diamond paste were used, starting with 14 μm (only for thin sections), 6 μm, 3 μm and finishing with 1 μm.

3.2.2 Powders for Whole-rock Multi-element Analysis

All the samples selected for whole-rock geochemistry were identically processed following the common approach; i.e.:

a) The samples were cut in thin slabs using a diamond saw.
b) The surfaces of all slabs were smoothed with emery to remove traces of ink, weathering and contamination from the saw blade.
c) The size reduction of slabs was made by hammering the samples wrapped in white paper, to avoid contact with the hammer and the metal base.
d) When necessary, a Cr-hardened steel roll mill was used for size reduction of samples; this step was only used when hammering was not enough to reduce the sample to the desired size.
e) Powdering of all samples using an agate ring mill anytime the sample weight was between 100 and 120 gr; when that weight of sample was not achieved, a smaller agate ball mill was used instead.

The rock powders obtained through this process were also used to produce pressed-powder pellets for XRF.

3.3 Analytical Procedures and Conditions

3.3.1 XRD

XRD analyses were performed in some samples to complement petrography whenever microscopy did not allow to clearly identify some mineral phases. The samples (a fine powder) were prepared at SQU facilities and placed on a spinning single-crystal silicon sample holder. The XRD record, measured at a step size of 0.0167° (2θ), was acquired with a X' Pert PRO X-ray Diffraction machine from Panalytical that used a Cu-Kα radiation (1.54060 Å) and was set to 40 mA and 45 kV. The data was further assessed with the "High Score Plus" software.

3.3.2 Portable EDXRF

During re-logging and sampling, a portable XRF was used at SQU facilities, as an auxiliary tool during macroscopic sample characterisation. A Niton XL3t 950 Handheld XRF Analyzer (Thermo Scientific), calibrated with laboratory test standards and equipped with a SDD GOLDD+ detector and a Ag anode X-ray tube (excitation voltage 50 kV, 200 mA, 2 Watt), was used in such approach. The instrument self-calibrates on an internal standard whenever the machine is switched on. No sample preparation is required since the beam is shot directly onto the sample area to be analysed.

3.3.3 Whole Rock WDXRF

One alternative to get WDXRF data consists of prepare in advance powdered samples with a flat surface. The preparation of pressed-powder pellets involved the following steps:

a) One pellet requires 12 g of rock powder, being that the average weight measured for all samples.
b) In a mortar, the sample was mixed with a mixture of acetone and elvacite (polymer), carefully mixed until reaching total homogenisation.
c) The sample holder was placed in a press, and the sample placed in the holder with a tube and a cylinder to slightly press it.
d) A perfect flat lid is placed onto the sample and pressure is slowly applied, allowing time for the volatiles to escape and the polymer to settle. This procedure is done twice after carefully rotating the sample holder for another position.

All measurements were carried at the Aveiro University facilities using an Axios equipment from Panalytical with a rhodium ampoule. The analytical error for major elements is 2% of the measured value, while minor and trace elements detection limits are available in Appendix II.

3.3.4 Whole Rock ICP-MS

The acquisition of minor and trace elements took place at the Géosciences Environnement Toulouse laboratory (Observatoire Midi-Pyrénées), Université of Toulouse III, via HR-ICP-MS ELEMENT XR and using the procedure described by Barrat *et al.* (2007). A HF-$HClO_4$ digestion (Yokoyama *et al.*, 1999) with Tm addition (Barrat *et al.*, 1996) was used to prepare the samples. After the acid digestion, the samples were diluted and analysed to obtain all minor and trace element concentrations. Analytical blanks were subtracted to BHVO2 and samples cps; so, if the blank is higher than the signal, the calculated concentration is negative and cancelled. Instrumental detection limits, analytical and total procedural blanks can be consulted in Appendix III.

3.3.5 Electron Probe Micro Analysis

All mineral chemistry analyses were produced on polished mounts covered by a thin carbon coating (20 nm) at FCUL facilities. The instrument used in this stage was a JEOL-JXA 8200 Micro Probe, equipped with four wavelength-dispersive spectrometers (WDS), six analysing crystals (LIF, LIFH, PET, PETH, TAP and LDED2) and secondary and retro-diffused electron detectors coupled to an energy-dispersive spectrometer (EDS). The measurements were performed with a 5 μm diameter beam, a 25 nA current and an accelerating voltage of 15 kV. In routine, the acquisition time for peaks was 20 s and 5 s for background radiation. The standards used and the detection limits for all measured elements are listed in Appendix IV and Appendix V, respectively.

4. Model for the Mandoos 1 Deposit

4.1 The Tridimensional Modelling of Mandoos 1 Deposit

The 3D model of the Mandoos 1 deposit was built using the data provided by Mawarid Mining and the MICROMINE software. The starting database includes data from 33 drill-holes (see figure 3.2): 29 along the pit zone, one located 1 km north from the pit, and the last three placed 250 m SE from the pit (the last drill-holes were performed during one of the latest exploration surveys done by the company). The 29 drill-holes are distributed in a regular 50 m x 50 m square grid.

The data were organised in *collar*, *survey*, *assay* and *lithology*. *Collar* data includes geographical coordinates, altitude and drill-hole length (DHL), besides the bore-hole ID (BHID). *Survey* data includes depth, azimuth and dip values. *Assay* data comprise concentration values of Cu, Zn and Fe in weight percentage (wt%) and Au and Ag in parts per million (ppm) linked to a particular depth. The *lithology* data includes the depth where a given lithology intersected by drill-hole starts and ends, and the lithological information. The Mawarid Mining also provided STRING files containing the pit design and sections of the ore-body.

This complete database is essential to build the 3D model, and its organisation is a key factor to easily insert the data on MICROMINE. *Collar* and *survey* data will allow placing the drill-holes, while *assay* and *lithology* data will let assigning grades and lithology along them. The STRING file for the pit design was used to model the shape of the pit and site; a digital landscape model (DTM) was created from the pit design file in addition with a geo-referenced image of the site extracted from Google Earth. In addition, the STRING file with the sections of the ore-body allowed to locating the orebody using not only the information gathered from the 33 drill-holes, but also from all the drills done by the company in the Mandoos 1 deposit.

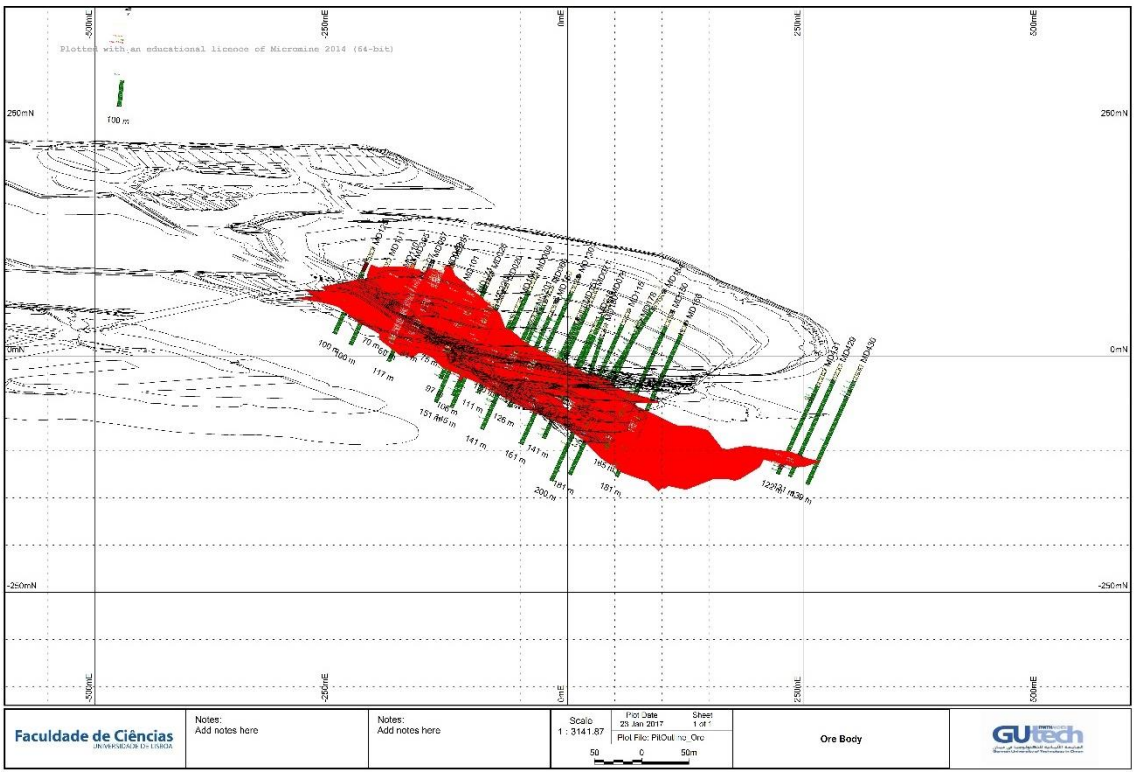

Fig 4. 1 - Pit design with implanted drill cores and the orebody extension.

Figure 4.1 illustrates the N-S aligned pit, with 620 m length and 390 m width; its depth increases towards south where it reaches 160 m, 60 m more than the deepest part of the north sector. The massive sulphide body has 550 m long and up to 370 wide; the average width is around 200 m. The massive sulphide lens varies in thickness from less than 1 m to a maximum of 90 m recorded in the northern sector of the deposit. The lens shows also a general NW-SE elongation dipping moderately towards SE.

4.1 Grades and Tonnage

Using the *implicit modelling* tool from MICROMINE, which uses simple kriging as the interpolation method, it was possible to model the Cu and Zn grades in the orebody. The buffer used in the interpolation was 75 m, i.e. 1.5 x the spacing between drills (50 m). Also, a colour code was given to the elements, red was used for Cu while blue was assigned to Zn. A colour grading, from light to dark colours, represents lower and higher grades. The limits used to define the cut-off grade for the colour coding were the minimum, first quartile, median and third quartile; however all analyses below the mine cut-off grade (0.3 wt% Cu) were previously excluded.

Fig 4.3 displays Cu and Zn grades distribution along the deposit, respectively; image (A) in both figures represents the higher grades with a cut-off defined by the third quartile of the concentration distributions, i.e. 2.44 wt% for Cu and 0.44 wt% for Zn. It is worth noting that the south sector is the most enriched in these elements, more precisely in section 2732850mN (drill-hole MD150 – Fig 3.2) where the two elements are largely overlapped, suggesting the lacking of significant metal zonation. The central sector of the deposit also shows Cu- and Zn-enriched zones (Section 2733000mN – Fig 3.2), but in this case an evident separation exists: a Cu-rich zone (MD071) to the east and a Zn-rich zone to the west (MD020). Along the two drill-holes that crosscut these two distinct zones there is no firm evidence for metal zonation, as can be seen in the sections in Appendix VI. The same can also be inferred from the NW-SE cross section along the lens alignment (see Fig 3.2), Fig 4.4 and Fig 4.5 show the Cu and Zn variations, respectively, along the ore body. As can be seen, the overlapping of Cu-rich and Zn-rich zones is recorded all over the entire lens. It is also clear that the north sector of the deposit is where the highest thickness of the ore-body is observed (Fig 4.6); however, this thick accumulation of sulphides do not display the highest grades. Due to the ore lens morphology and some evidence for NW-SE (to N-S?) fault zones, this thicker domain of the ore-body is interpreted as a hemi-graben filled with massive sulphides (Fig. 4.2).

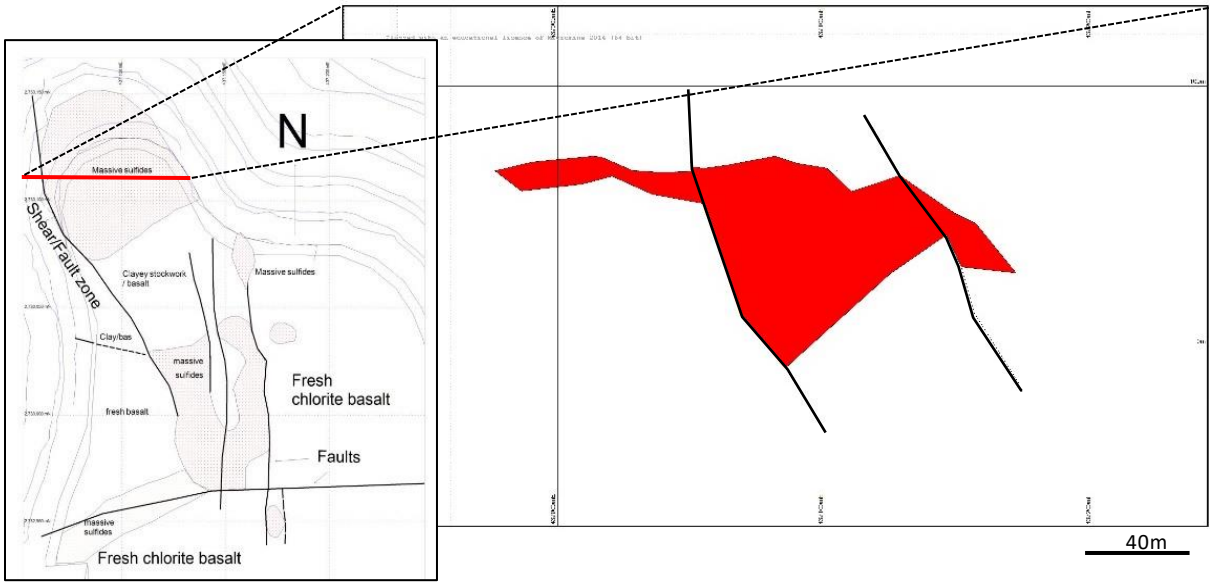

Fig 4. 2 – North sector fracture network and massive sulphide lens E-W cross-section showing the fault-related displacements consistent with a hemi-graben morphology.

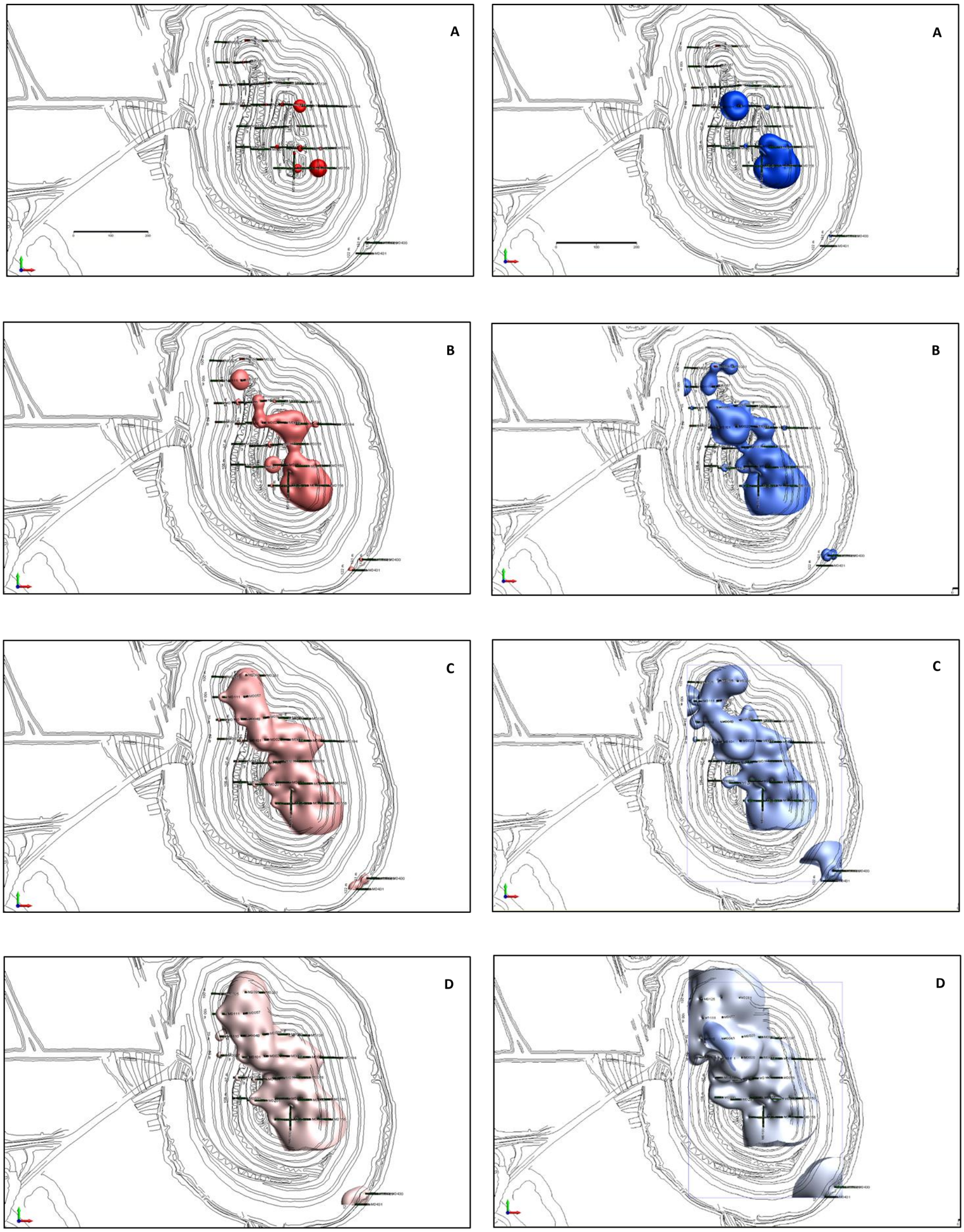

Fig 4. 3 – LEFT - MICROMINE implicit modelling for Cu distribution by cut-off grade; (A) 2.44 wt%, (B) 0.88 wt%, (C) 0.5 wt% and (D) 0.3 wt% (mine cut-off grade. RIGHT - MICROMINE implicit modelling for Zn distribution by cut-off grade; (A) 0.44 wt%, (B) 0.15 wt%, (C) 0.09 wt% and (D) 0.01 wt%.

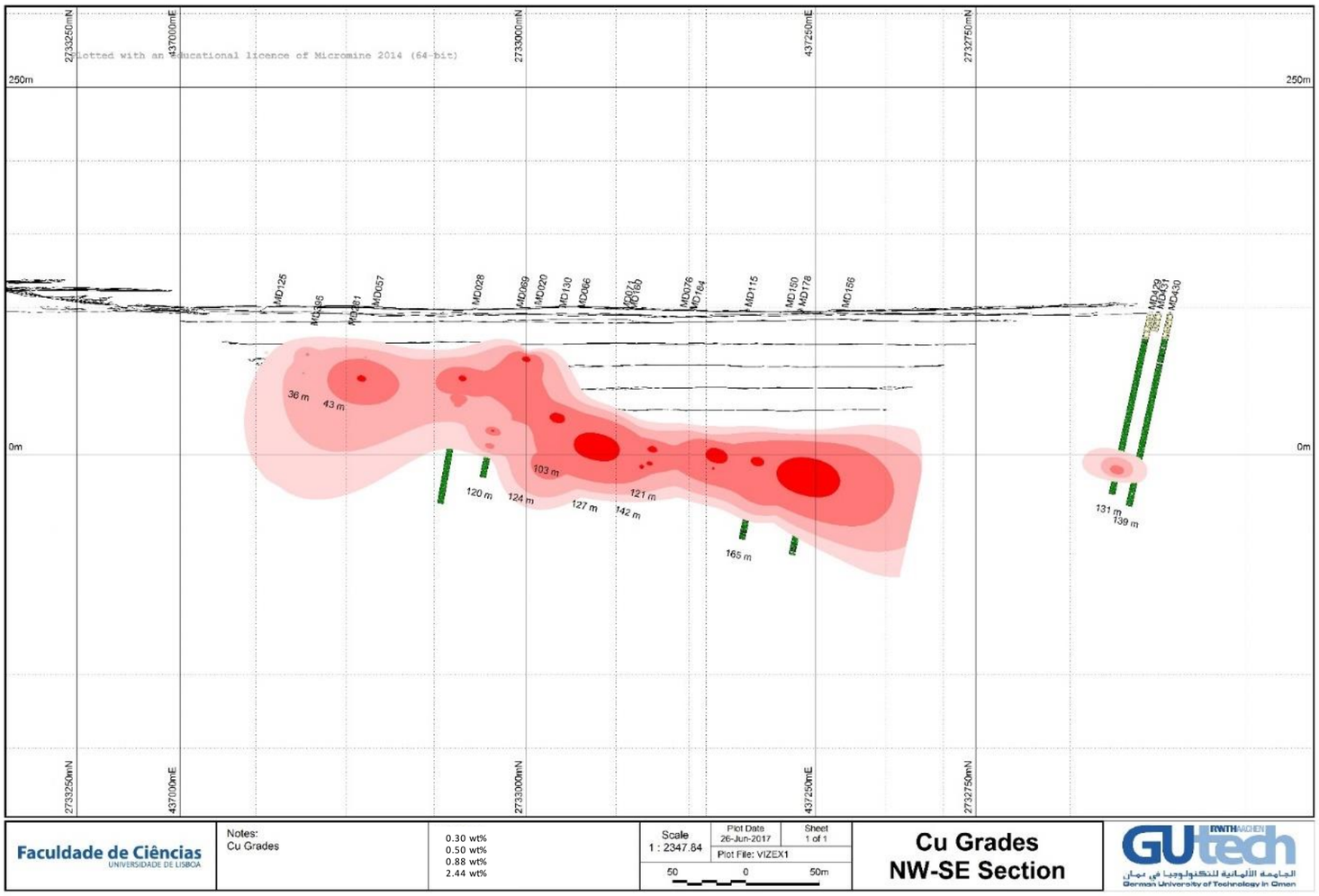

Fig 4. 4 - Cu grades distribution along NW-SE section (see Fig. 3.2)..

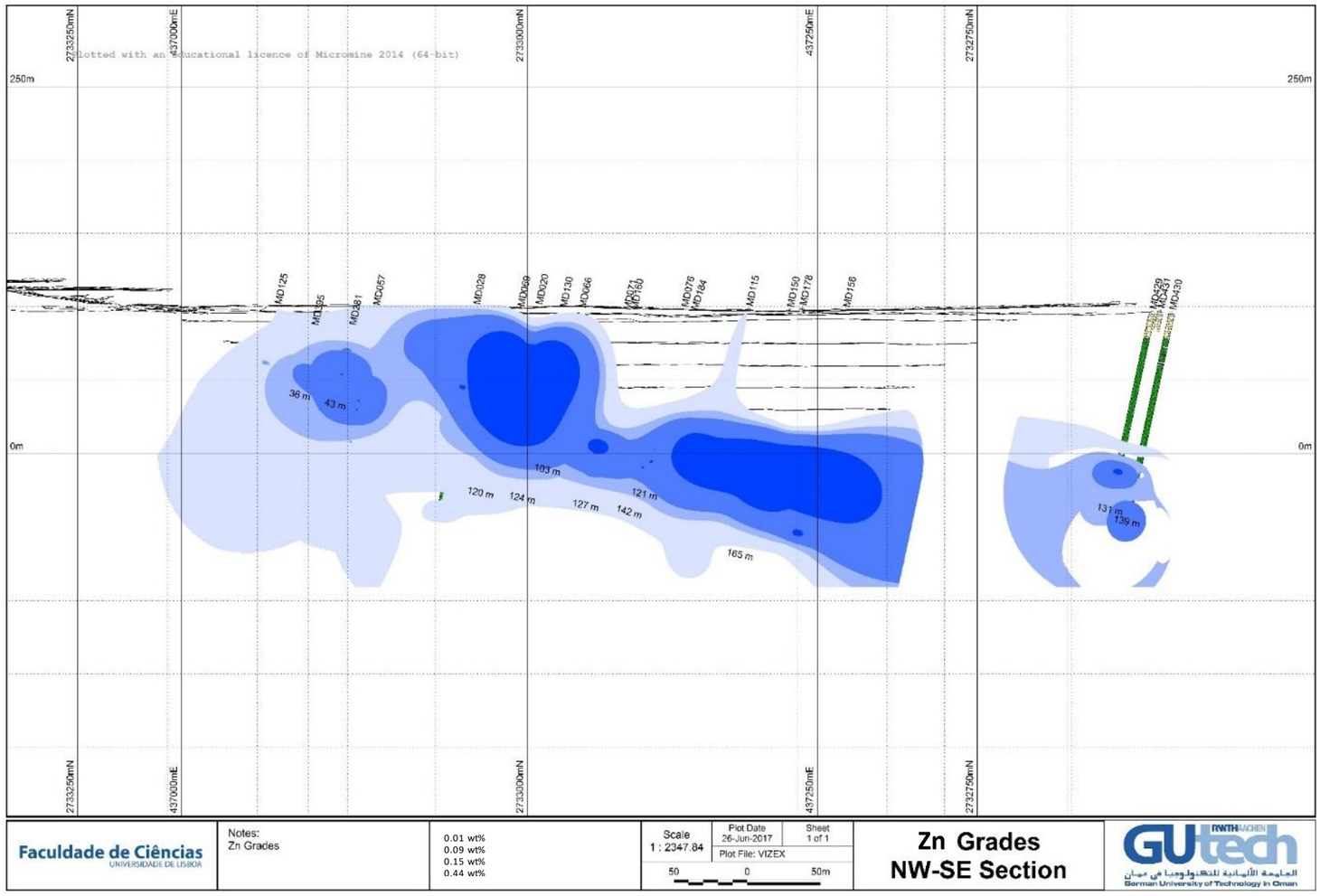

Fig 4. 5 - Zn grades distribution along NW-SE section (see Fig. 3.2).

The Mawarid's engineers assessed in Mandoos 1 a total resource of about 8 Mt of Cu-rich massive sulphide ore (mine cut-off grade = 0.3 wt% Cu), including ca. 5 Mt in reserves with 1.8 wt% Cu (Mawarid Mining, 2014; Rob Willis, pers. com. to Ana Jesus, February, 2015). The orebody (Fig 4.6) volume calculation revealed a total value of 1.8 M m^3. Assuming a typical composition of about 80% pyrite, 12% quartz, 5% chalcopyrite and 2% of sphalerite, and knowing that the respective densities are 4.8 g/cm^3, 2.65 g/cm^3, 4.1 g/cm^3 and 3.9 g/cm^3, the massive sulphide lens comes out with an average density of 4.44 g/cm^3 and total tonnage of 7.99 Mt. The average grade of 1.8 wt% Cu reported by the company is also obtained by a simple mean calculation of all Cu values above the mine cut-off grade; however when weighted, the average grade drops to 1.72 wt% Cu.

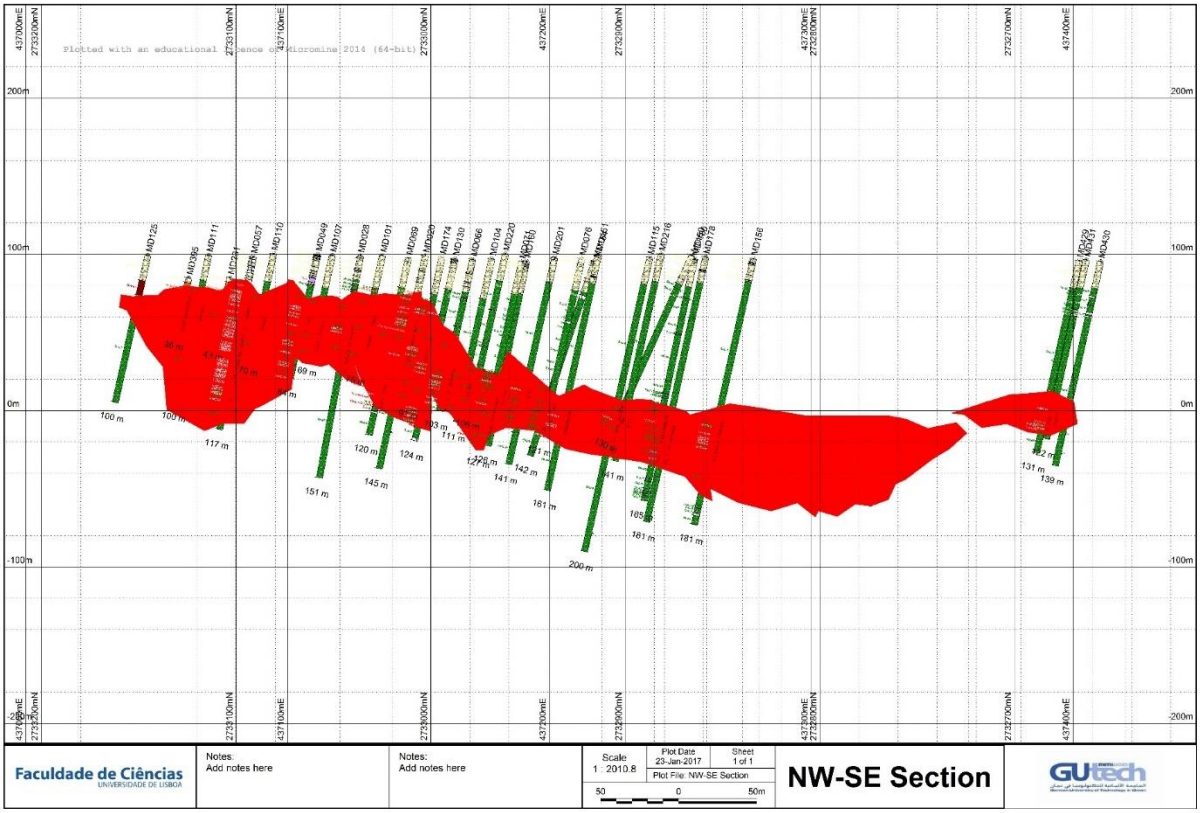

Fig 4. 6 - NW-SE section of the Mandoos massive sulphide lens.

5. Petrography

The present section of the work summarises the main mineralogical and textural features displayed by sulphide ores (including mineralised basalts), metalliferous sediments (umber and ochres) and jaspers (massive sulphide mineralised jaspers and manganese jasper) at microscale, using reflected and transmitted light microscopy. Complementary EPMA information and additional macroscopic (hand sample) evidence will also be locally included.

5.1 Sulphide Ores

Samples of massive sulphides *s.s.* are not common in this deposit. Actually, throughout all the sampling survey there was no evidence of real massive sulphides; the ores normally occur as heterometric breccias (Fig. 5.1). Texturally, these breccias are quite regular, with the exception of some cases comprising fragments that display wider textural diversity. The presence of pyritised (transversal and longitudinal) cross-sections of tubeworms (*polychetae*) is worth noting (Fig. 5.2 – 1, 2), placing the examined samples in the black-smokers environment (MD-P2-3-2). A large number of samples consist of poorly calibrated breccias mainly composed of pyrite clasts (Fig. 5.1). Their formation is possibly a result of successive mass-wasting events occurring at the sea-mounds. The clasts can vary from small, single, fractured, (sub)euhedral grains to large fragments of massive aggregates. These can differ in composition or in texture, pyrite being the most common example.

Samples from "massive sulphide ores" show a monotonous mineral assemblage, comprising a small number of different mineral phases. They are mainly composed of recrystallised pyrite, having chalcopyrite, marcasite and sphalerite as common accessory minerals; Cu-rich phases are also present in some samples and quartz, laumontite and phyllosilicates are the usual gangue-forming phases. Primary textures are common among the clasts: round to long colloform clasts (Fig. 5.2 - 4, 5, 6, 7) and framboidal masses (Fig. 5.3 – 3) are seen throughout the breccias, usually associated with chalcopyrite, occurring as replacements of former pyrite grains. Often recrystallised, the cores of pyrite aggregates also preserve primary textures such as framboidal and colloform; wherever these clasts do not show preserved primary textures, it becomes difficult to distinguish between the recrystallised and a second generation of pyrite. All these structures appear to be replaced or filled by chalcopyrite ± bornite ± Cu-rich phases; usually, the alteration starts at the crystal borders and creates a Cu-rich ramification structure that sometimes partly obliterates all the primary texture (Fig. 5.3 – 7). Clasts, presumably related to hydraulic brecciation, are also frequent and these can vary in size, but normally are coarse-sized clasts composed mostly of recrystallised pyrite, crisscrossed by a network of late quartz-veins showing a jigsaw fit texture, being the surroundings of the veins more recrystallised.

Pyrite clasts (varying from euhedral crystals to large masses) are typical, but marcasite, chalcopyrite and sphalerite clasts can also be seen. Pyrite shows distinct occurrence modes, being the most common as euhedral recrystallised masses where a growth zonation (or banding) is evident, usually decorated by small inclusions of sphalerite (Fig. 5.2 – 8) and rarely by chalcopyrite inclusions. The growth zonation is often traced by alternation between well-recrystallised pyrite and porous pyrite. In some samples, euhedral pyrite displays vuggy arrangements. Marcasite can be seen more rarely as coarse euhedral grain masses (Fig. 5.3 – 2), displaying colloform textures and more often as masses (usually surrounded by pyrite) partly replaced by chalcopyrite. Chalcopyrite occurs as large masses, being replaced by bornite and other Cu-rich phases, and as clear masses/crystals with sphalerite inclusions.

Some samples show a platy chalcopyrite in quartz and phyllosilicates veins and it can also be observed in crack-infillings affecting pyrite. Usually the cement of these breccias comprise quartz and

phyllossilicates, or a mixture of quartz and small pyrite grains ("pyrite sands"); nevertheless laumontite also occurs, often as an accessory phase in the cement and as part of the mineral infillings of open spaces in large masses of pyrite and chalcopyrite.

The sample MD-P3-4-1 is an exception, displaying a carbonate cement. Similarly, the sample MD-NP-1 is characterised by a particular texture, where large sphalerite masses containing numerous oriented chalcopyrite (triangular) inclusions can be interpreted as a primary texture (Fig. 5.3 - 5), by analogy to what is commonly displayed by black-smokers. The sphalerite masses are inter-grown/filled with laumontite and is locally replaced by bornite, as happens with co-existent chalcopyrite. The Zn-rich zone contacts with a Cu-rich zone, where some sphalerite can be seen replaced by chalcopyrite (?). In these samples, some of the chalcopyrite masses are also inter-grown with laumontite; these late infillings also contain pyrite, marcasite and fine-grained sphalerite. The MD-NP-1 sample also includes skeletal wurtzite (paramorphic sphalerite) infilled/altered by iron sulphides taking advantage of the space between crystals. Platy crystals of wurtzite forming well-developed elongated prismatic aggregates crystallised in open spaces (infilled with laumontite) can also be locally observed (Fig. 5.3 – 4).

Fig 5. 1 - ***Hand Samples****:* ***A*** *– MD-NP-1 – Zn-rich ore, sphalerite and chalcopyrite rich ore with late laumontite infillings;* ***B*** *– MD-P3-4-1 – massive sulphide breccia mainly composed of pyrite clasts cemented by carbonates;* ***C*** *– MD-P2-3-2 – massive sulphide breccia cemented by silica and phyllosilicates, characterised by preserved primary textures, including pyritised tubeworms;* ***D*** *- MD178-128.80 – massive sulphide breccia cemented by silica and crosscut by large sphalerite rich vein;* ***E, F, G, H*** *– samples of massive sulphide breccias displaying a silica rich cement. The graphic scale bar is 2 cm.*

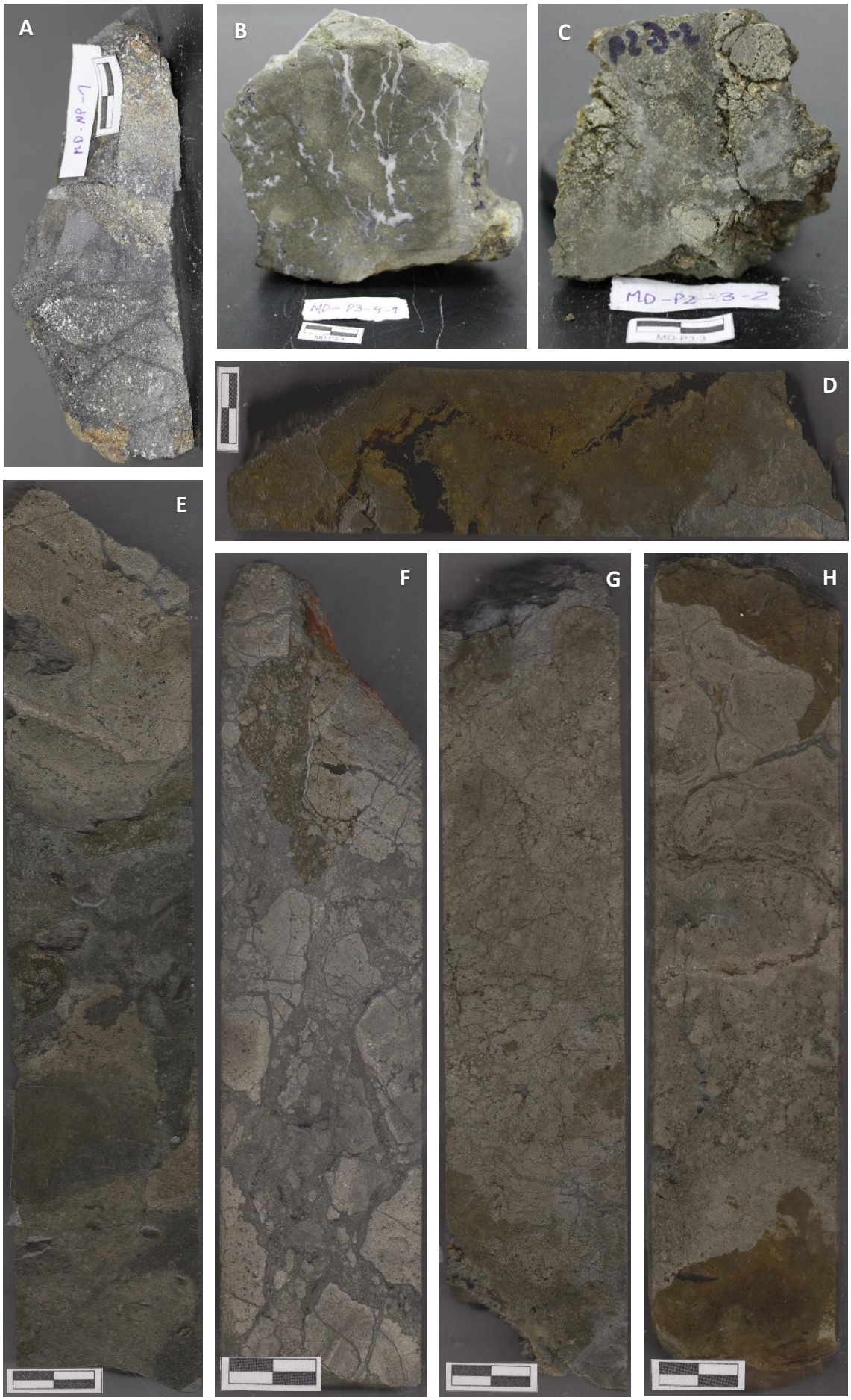
A
B
C
D
E
F
G
H

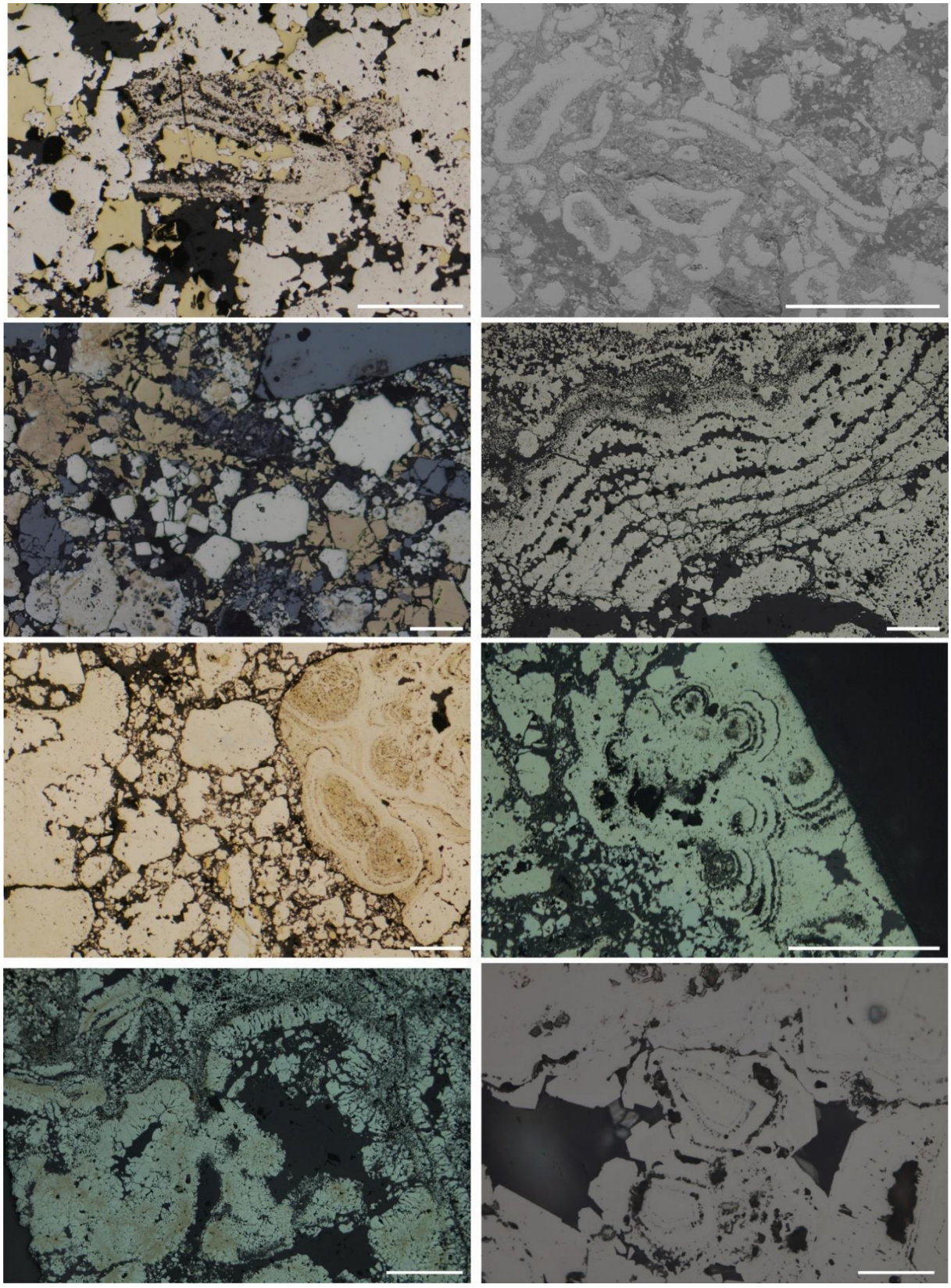

Fig 5. 2 – ***Microphotography - 1 -*** *Tubeworm preserved in the second generation of Py and Ccp intergrowths – RL – PPL;* ***2*** *– Pyritised tubeworms (various sections) in a cement enriched in silica and phyllosilicates – BSE;* ***3*** *– Massive sulphide breccia texture displaying Py, Ccp and Sp clasts – RL – PPL;* ***4*** *– Colloform Py intergrowth with silica displaying some hydraulic brecciation – RL – PPL;* ***5*** *– Py breccia showing recrystallised clasts and clasts displaying primary textures (colloform) – RL – PPL;* ***6*** *– Colloform Py preserved in recrystallised mass – RL – PPL;* ***7*** *– Colloform marcasite being replaced by Ccp – RL – PPL;* ***8*** *– Py displaying growth zonation marked by Sp inclusions. The graphic scale bar is 400 μm in RL and TL microphotography and 200 μm in BSE images.*

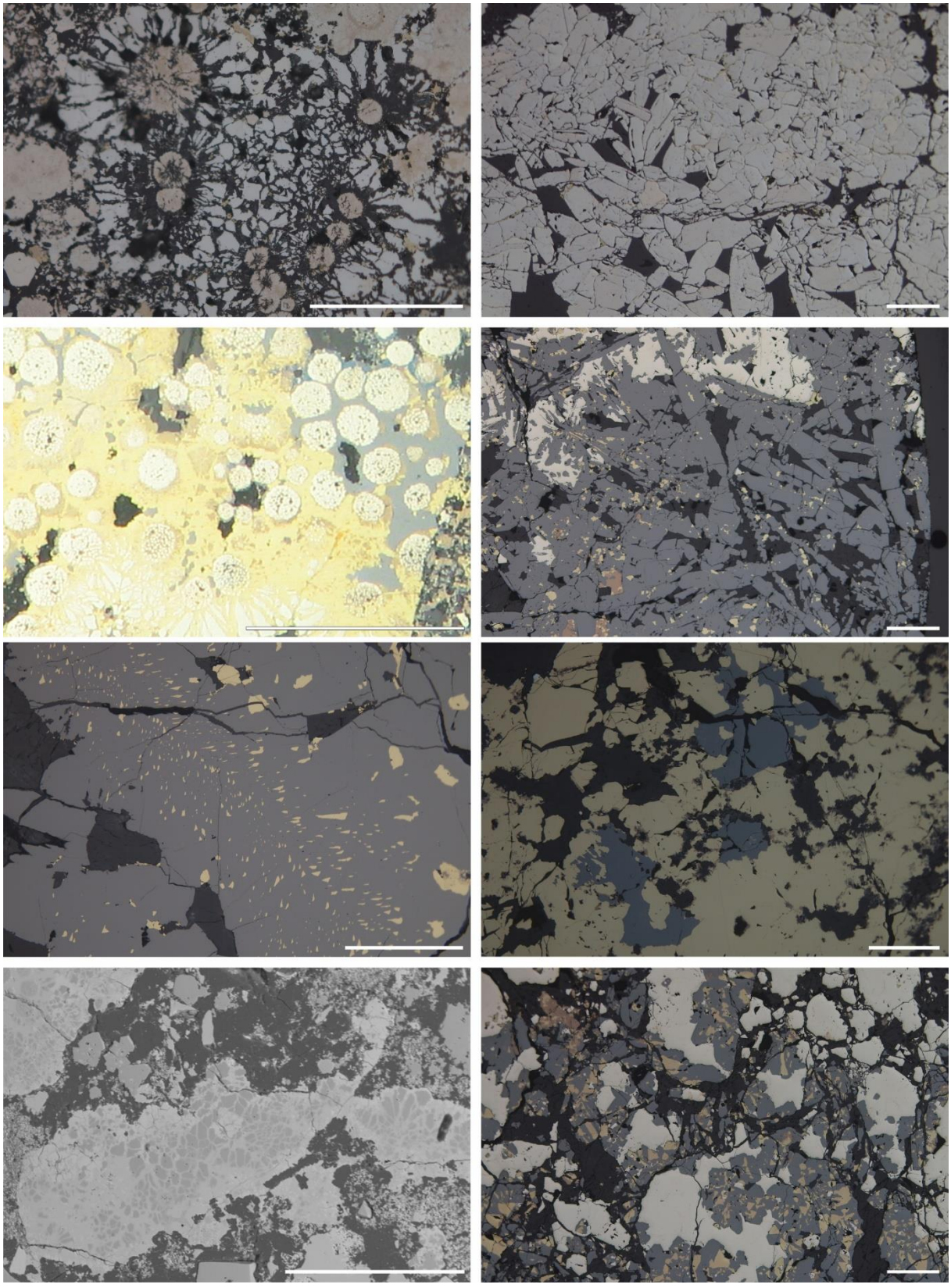

Fig 5. 3 – ***Microphotography - 1*** *- Mrc growing around framboidal Py – RL – PPL;* ***2*** *– Coarse grain euhedral Mrc intergrowth with silica – RL – PPL;* ***3*** *– Framboidal Py clast being replaced by Ccp, Cu-rich phases oxidising Ccp – RL – PPL;* ***4*** *– Prismatic Wur infilled with Lmt – RL – PPL;* ***5*** *– Sp displaying crystallographically oriented Ccp inclusions and infilled together with Lmt – RL – PPL;* ***6*** *– Sp and Ccp intergrowths – RL – PPL;* ***7*** *– Clast showing "shattered" texture due to Ccp and Cu-rich phases alteration – BSE;* ***8*** *– Wur (prismatic sections) with Ccp inclusions in Py clasts – RL – The graphic scale bar is 400 μm in RL and TL microphotography and 200 μm in BSE images*

5.2 Silicified Mineralised Basalt

The silicified basalts display abundant disseminations of fine-grained euhedral to sub-euhedral pyrite (Fig. 5.4 – 1, 2). Mineralised veins are seen crosscutting the basalts. Adjoining their walls, pyrite dissemination is more intense and coarser-grained, whereas minor amounts of chalcopyrite can also be present. The infillings of these veins include a mineral assemblage composed of coarse-grained euhedral pyrite crystals encased by large masses of chalcopyrite with scarce sphalerite inclusions (Fig. 5.4 – 3). Sphalerite is seen as inclusions in both pyrite and chalcopyrite; this sphalerite can show effects of "chalcopyrite disease" and is characterised by low Fe-contents. Some late-deposited quartz and phyllosilicate rich vein infillings (? poorly polished surface mineral) crosscut chalcopyrite masses; these also carry some pyrite and sphalerite. A second generation of sphalerite is characterised by lighter internal reflections, indicating lower Fe-contents (presumably developed under lower temperature conditions); the zinc was possibly released during the sphalerite replacement by chalcopyrite and lately incorporated in the quartz rich veins.

*Fig 5. 4 – **Hand Samples** - MD430-131.00 (**A**) and MD430-127.70 (**B**) – Silicified basalt displaying sulphide disseminations and sulphide veins. **Microphotography – 1** – Euhedral Py disseminations in the basalt – RL – PPL; **2** - Euhedral Py disseminations in the basalt – RL – XPL; **3** – Py, Ccp and Qz present in veins – RL – PPL; **4** – Breccia texture present in vuggs – RL – PPL; **5** - Breccia texture in rock vugs – RL – XPL. The graphic scale bar is 400 μm in RL and TL microphotography and 2 cm in hand samples.*

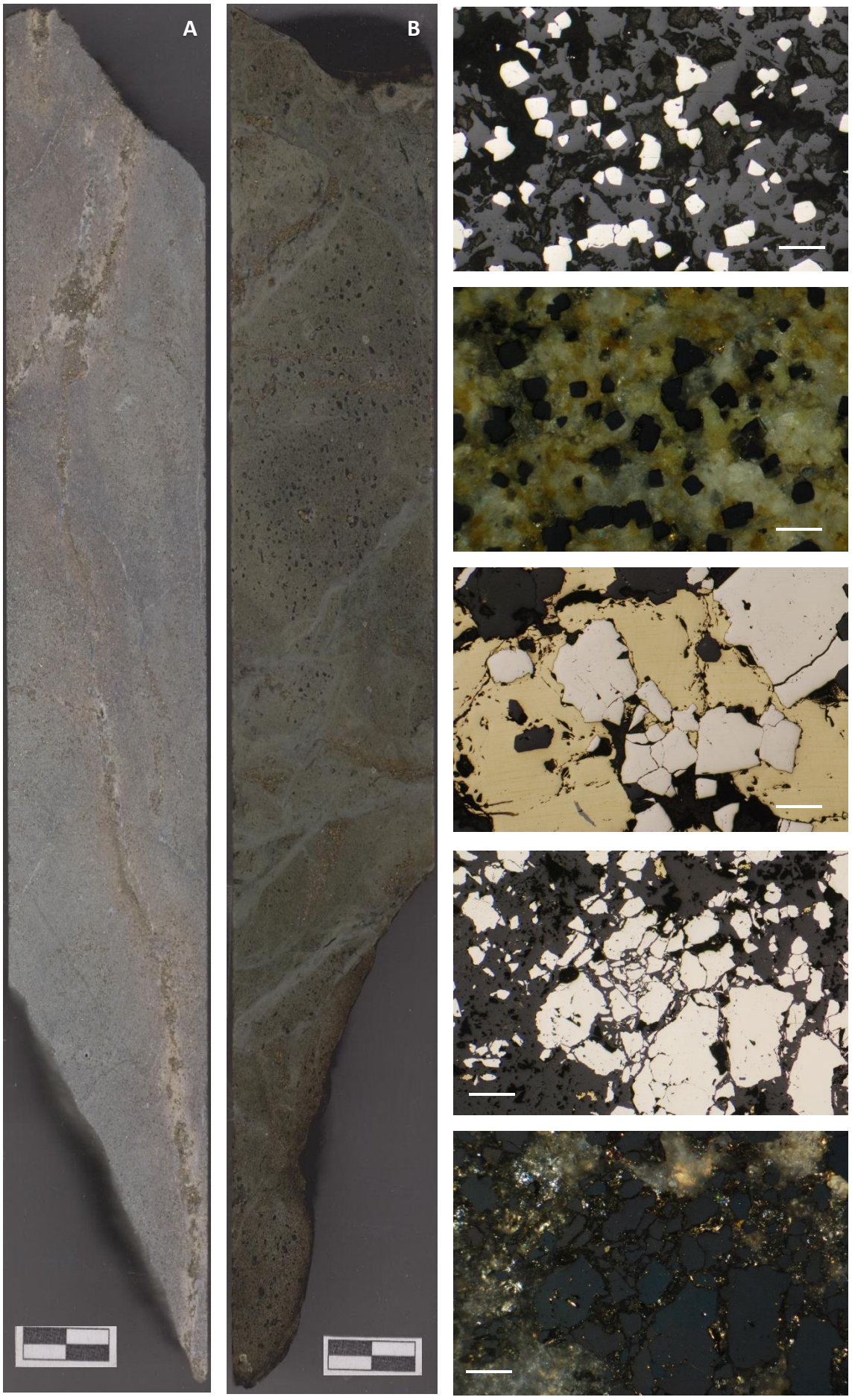
A
B

5.3 Metalliferous Sediments

Three texturally different types of metalliferous sediments were examined. The first one shows a clear sedimentary texture composed of a rhythmic fine-grained banding of Fe-oxide poor to Fe-oxide enriched sediments (Fig. 5.5 F), the latter being more abundant and thicker. In these layers, the Fe-oxide grains tend to develop clusters with ellipsoidal shapes (Fig. 5.6 – 2) whose minor axes are sub-perpendicular to the layering (indicating some compression, conceivably related to sedimentation and diagenesis processes). The sample also displays two different types of carbonate veins, one perpendicular to the layering, with no evidence of mineralization, and a later set of veins showing comb-texture (Fig. 5.6 – 1) with accessory amounts of sulphides (chalcopyrite and Cu-rich phases? in Fig. 5.6 - 7). There is no other evidence of sulphide minerals or clasts. Sample (MD178-134.20) also shows a sedimentary texture, but in this case the alternation of layers is between Fe-oxide rich (jasper like) and sulphide-rich sediments (Fig. 5.5 E), the latter mainly composed of pyrite and chalcopyrite but also containing small amounts of sphalerite and covellite.

Pyrite occurs in different textural arrangements, mostly forming fine-grained masses (resulting in a "dirty-looking" polished surface), but it can occur as well as sub-euhedral grains of variable size (resulting in a "clean" polished surface). The massive pyrite borders sometimes show some recrystallisation (?) and these massive aggregates may preserve some colloform textures. As previously referred, ochre sediments may include some interlayered graded beds of "detrital" sulphides and tend to be confined to the contact with the massive sulphide lenses, as observed in this sample. A clear contact between massive sulphides and the layered Fe-rich sediment with sulphide rich intercalations also shows a sphalerite infilling (vein/space??); it is characterised by very fine intergrowths of sub-euhedral sphalerite grains, quartz(?) and some covellite. The third type (MD174-62.15) shows a completely different texture: a coarse-grained breccia impregnated and cemented by Fe-oxides and criptocrystalline silica (Fig. 5.5 C); the clasts are also replaced by Fe-(hydr)oxides and hydroxides, mostly hematite and goethite. The observed texture is easily correlated with the massive sulphide breccias, where euhedral altered pyrite clasts (Fig. 5.6 – 6, 7), along with colloform (Fig. 5.6 – 8) and framboidal pyrite clasts, can still be recognized as pseudomorphs. Some sulphides are still preserved in few mineral cores, namely chalcopyrite being replaced by bornite and other Cu rich phases (Fig. 5.6 – 3, 4).

*Fig 5. 5 – **Hand Samples** – **A** – MD-P2-2B – Ochre; **B** – Umber; **C** – MD174-62.15 - Oxidised massive sulphides; **D** – Massive sulphide mineralised jasper; **E** - MD178-134.20 – Ochre displaying sulphide layers close to the contact with the massive sulphide lens; **F** – MD-P2-2A - Layered ochre. The graphic scale bar is 2 cm.*

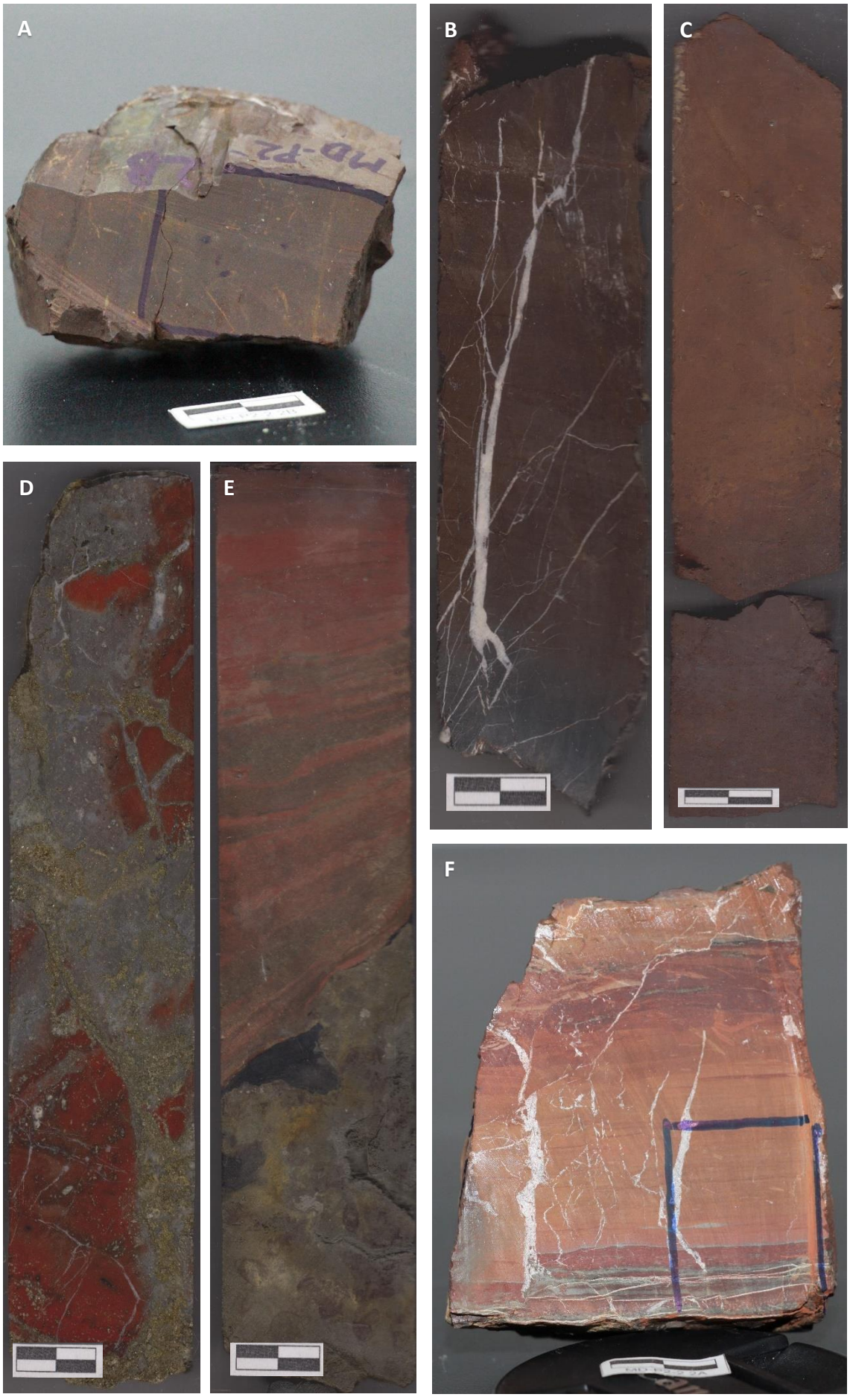
A
B
C
D
E
F

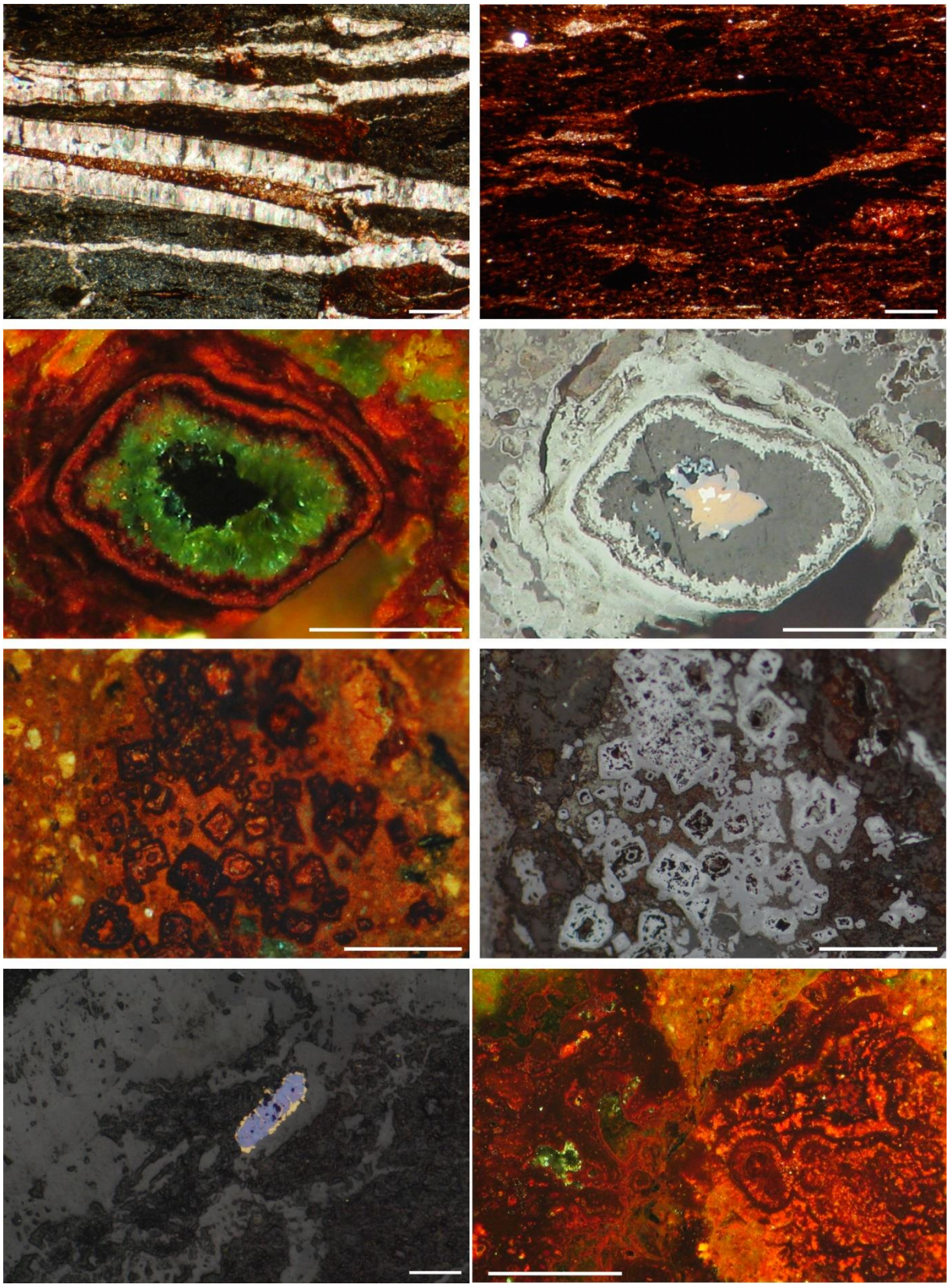

Fig 5. 6 – ***Microphotography – 1*** *– Carbonate veins crosscutting the sample parallel to the layering – TL – XPL:* ***2*** *– Fe-oxide clusters sub-perpendicular to the layering – TL – XPL;* ***3*** *– Sulphide clast replaced by Fe-oxides and hydroxides and infilled by malachite? – RL – XPL;* ***4*** *– Preserved sulphides in the clast core – RL – PPL;* ***5*** *– Pseudomorphs after py in Fe-hydroxide matrix – RL – XPL;* ***6*** *- Fe-oxides pseudomorphs after py– RL – PPL;* ***7*** *– Sulphides in carbonate vein – TL – PPL;* ***8*** *– Oxidised colloform texture – RL – XPL. The graphic scale bar is 400 µm in RL and TL microphotography.*

5.4 Jaspers

The examined jaspers are always mineralised, as disseminations or vein infillings, particularly when in direct contact with massive sulphides. Disseminations of pyrite are common, developing aggregates of small anhedral grains and, most often, aggregates of euhedral crystals of variable size, possibly representing recrystallised grains (Fig. 5.7 – 1). An intermediate stage between these two occurrence modes is possibly represented by larger anhedral pyrite aggregates. Scarce chalcopyrite intergrowths with sphalerite displaying effects of "chalcopyrite disease" (secondary exsolution) are also disseminated but mostly associated with the anhedral pyrite aggregates. This chalcopyrite is locally replaced by bornite and covellite, suggesting a less reducing environment. Both euhedral pyrite and the aggregates have sphalerite inclusions. Two different sphalerite inclusions can be seen: clear sphalerite (more common) and sphalerite with chalcopyrite segregations.

It is also noticeable a grain size increase towards the massive sulphide veins; also, the grains become more euhedral. The veins show a Fe-leached rim and are composed of large euhedral to sub-euhedral crystals of pyrite encased in large masses of chalcopyrite, accompanied by quartz (Fig. 5.7 – 5, 6). Some pyrite grains show more "clean" and flat edges, contrasting with the core domains, which are more irregular, indicating the progression of recrystallisation processes. Chalcopyrite is usually seen filling cracks on the pyrite whereas there is evidence for scarce chalcopyrite inclusion in pyrite, mostly adjoining chalcopyrite masses. Besides the Fe-leached rims observed in the veins, other leached zones, with no evidence of iron oxides are also seen throughout the samples. These are characterised by larger pyrite crystals (Fig. 5.7 – 2) and anhedral aggregates with a breccia texture; some sphalerite and chalcopyrite is also observed in this zone. The jasper impregnation by sulphides is possible due to increasing porosity during leaching, leading also to the formation of veins and some collapse breccias (Fig. 5.7 – 3, 4), later silicified when the system temperature cools down.

One sample (MD-NP-3) shows a completely different mineralogy, being composed of cryptocrystalline silica inter-grown with manganese oxides; the sample also shows large euhedral pyrolusite crystals (diamond shape) and late veins possibly sealed by romanechite (according to its optical properties). In the hand specimen it is evident the presence of jasper clasts within the manganese ore.

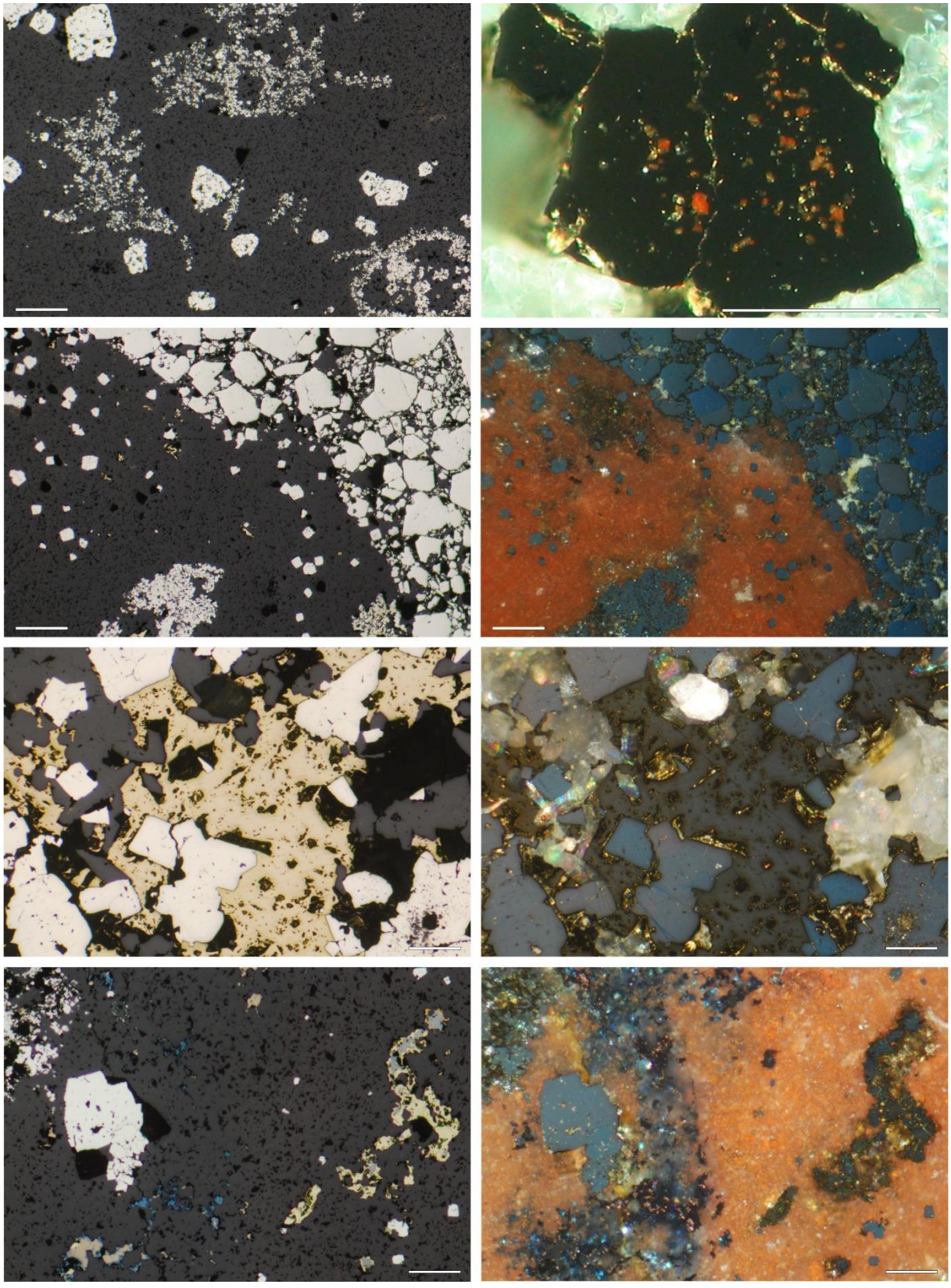

Fig 5. 7 – ***Microphotography – 1*** *– Fine-grained anhedral aggregates and euhedral Py disseminations in jasper – RL – PPL;* ***2*** *– Py grain with jasper inclusions, displaying a leached rim – RL – XPL;* ***3*** *– Py breccia zone in contact with jasper having disseminated Py – RL – PPL;* ***4 -*** *Py breccia zone in contact with jasper including Py disseminations (as in microphoto 3) – RL – XPL;* ***5 -*** *Sulphides associated with mineralised veins – RL – PPL;* ***6 -*** *Sulphides associated with mineralised veins (as in microphoto 5) – RL – XPL;* ***7*** *– Disseminations in jasper, Ccp being altered by Cu-rich phases – RL – PPL;* ***8 -*** *Disseminations in jasper, Ccp being altered by Cu-rich phases (as in microphoto 7) – RL – XPL. The graphic scale bar is 400 µm in RL and TL microphotography.*

6. Mineral Chemistry

Sulphide phases forming the massive ores of Mandoos were the main focus of the work carried out using EPMA. Therefore, a comprehensive survey was prepared, covering different sulphides and textural arrangements, and resulting in 946 quantitative analyses distributed over 15 polished mounts previously examined under the reflected light microscope. The analytical dataset obtained include 310 analyses of pyrite, 262 of chalcopyrite, 181 of sphalerite, 111 of marcasite, 64 of various Cu-rich phases, 13 of bornite and 5 of galena (Appendix VII for detection limits and Appendix VIII for analyses).

6.1 Iron Sulphide Phases

Iron sulphides are by far the most abundant phases in the studied ore samples. Pyrite prevails and its composition is close to ideal FeS_2, with median composition of $Fe_{0.999}S_2$ and iron content scattered in the 0.948-1.017 interval. Various elements are present in minor and trace amounts; the most significant are Cu, Zn and Pb, displaying highly asymmetric distributions typified by median values of 210 ppm, 315 ppm, 180 ppm and contents up to 89780 ppm, 27890 ppm and 7070 ppm, respectively (Fig. 6.1). Also worth mentioning is the presence of non-negligible amounts of As, In, Se and Co, characterised by median values of 70 ppm, 70 ppm, 90 ppm and 200 ppm respectively.

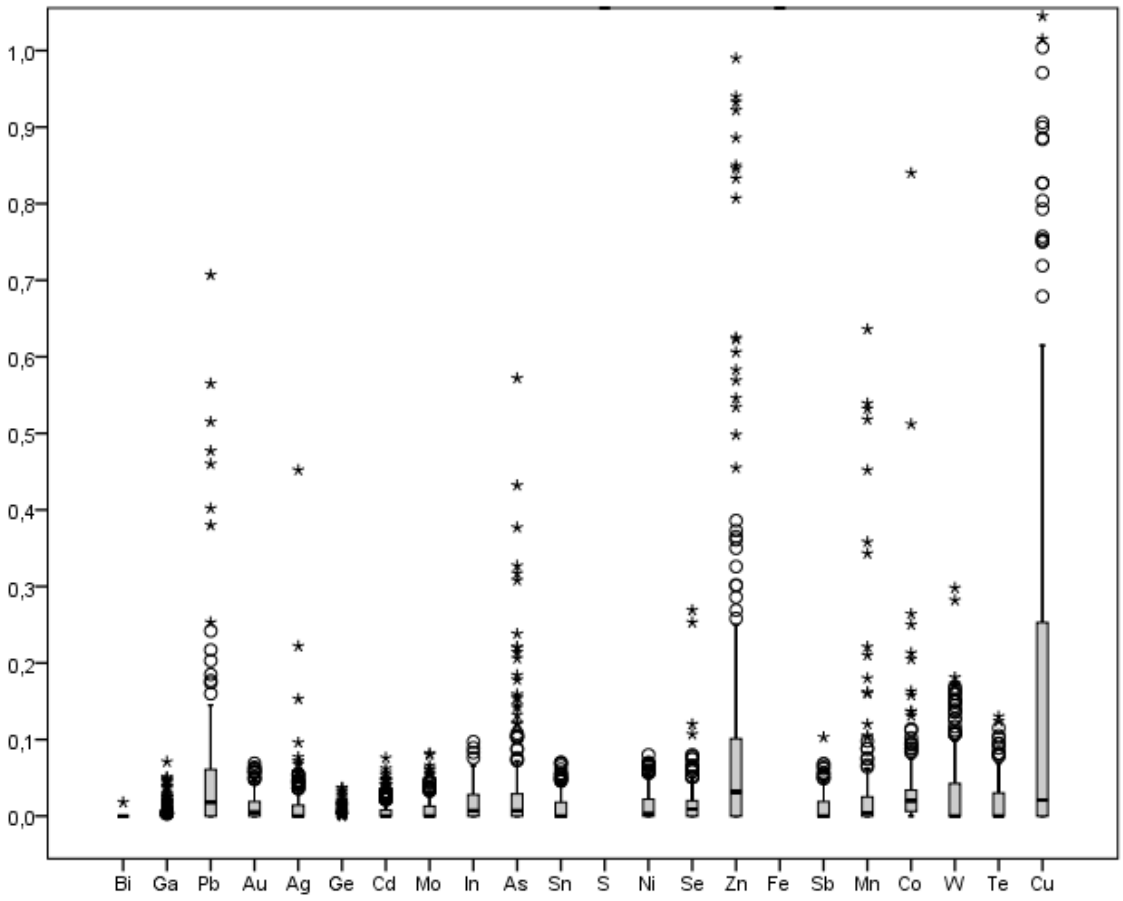

Fig 6. 1 - Box and whiskers plot for the multi-element concentration distributions displayed by 310 analyses of pyrite (concentration values in wt%). Note the relative importance of Cu, Zn and Pb as minor elements. Traces of some other elements are noteworthy, namely As, In, Se and Co (and Au?).

Marcasite composition is also close to ideal, with $Fe_{0.949-1.017}$ and median composition of $Fe_{0.997}S_2$. It displays minor/trace amounts of Cu, Zn and Pb (like pyrite), which may reach 3820 ppm, 9800 ppm and 3850 ppm, respectively (Fig. 6.2); the median values of the concentration distributions for these elements are BDL or quite close to that value (highlighting the strong distribution asymmetry), being the third quartile equal to 1020 ppm, 320 ppm and 200 ppm respectively. In addition, traces of Mn and Co are statistically meaningful, displaying median values of 70 ppm and 200 ppm, respectively. The last two elements are possibly accompanied by W, Te, In and Au, for which the calculated medians are BDL (third quartile = 428 ppm), 20 ppm, 60 ppm and 50 ppm.

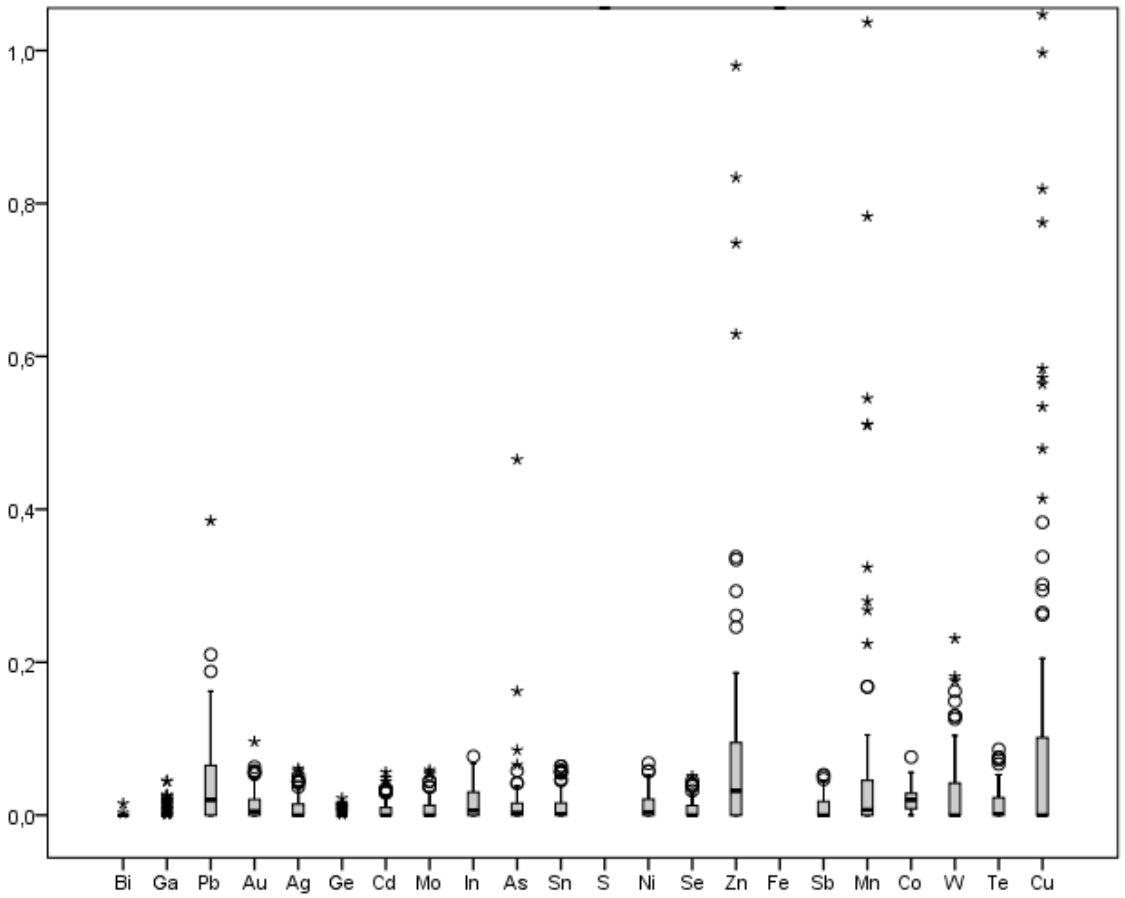

Fig 6. 2 - Box and whiskers plot for the multi-element concentration distributions displayed by 111 analyses of marcasite (concentration values in wt%). Note the relative importance of Cu, Zn and Pb as minor elements (like pyrite). Traces of Mn and Co also with statistical meaning.

When plotted in a ternary diagram (Fig. 6.3), both pyrite and marcasite show similar behaviour, notwithstanding the larger deviation displayed by pyrite analyses. The (S+As)–Fe–(Cu+In) diagram shows, as expected, a strong overlapping of the majority of samples in the FeS_2 end-member field but with a clear trend of Cu enrichment, in this case towards the chalcopyrite composition. The same trend is shown in the (S+As)–(Zn+Cd+Co)–(Cu+In) diagram, but it also points out an enrichment, although less significant, in Zn revealed by the compositional departure towards the sphalerite composition.

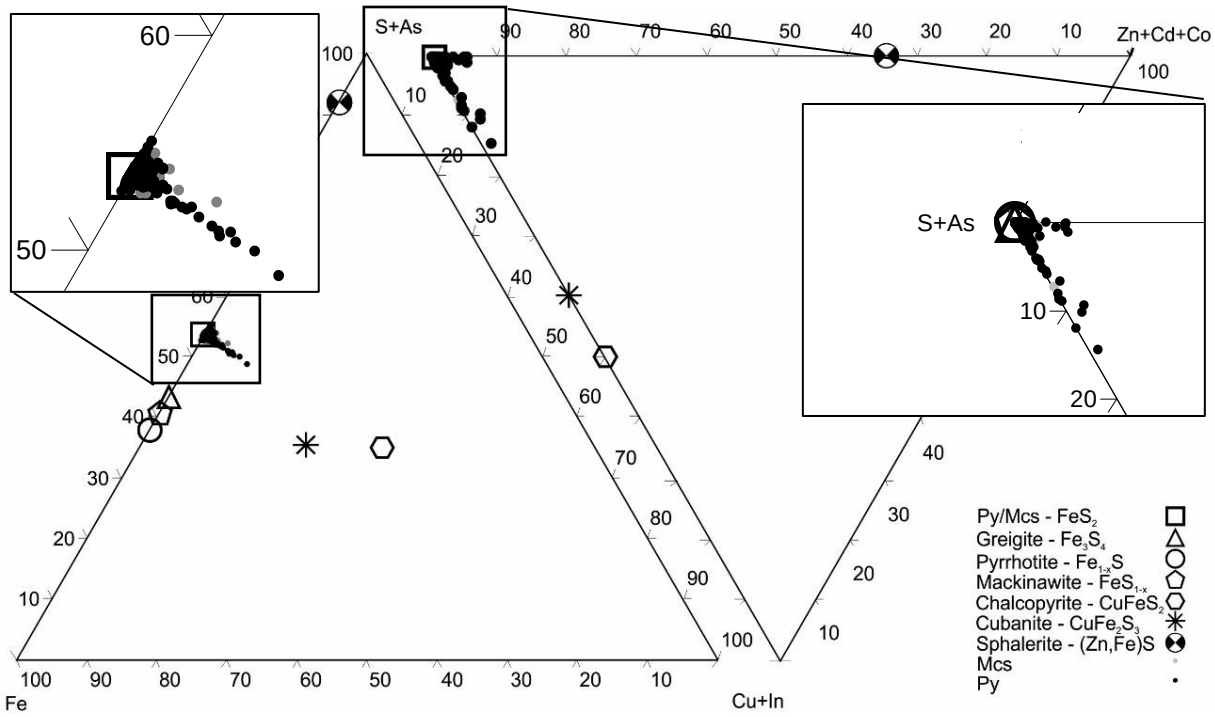

Fig 6. 3 - Ternary (S+As)–(Cu+In)–(Zn+Cd+Co)–Fe diagrams putting in evidence compositional deviations towards Cu and Zn enrichment.

The compositional trends of Cu and Zn enrichment are also seen when plotting bivariate diagrams for the most significant minor and trace elements. In Figs 6.4 and 6.5, the textural arrangements where the pyrite and marcasite analyses were obtained, are distinguished. Primary textures, such as framboidal and colloform, and recrystallised masses or euhedral grains were individualised. Despite some analyses might be affected by crypto-exsolutions or crypto-inclusions (e.g. massive marcasite replaced by chalcopyrite – Fig 6.5), it is clear that Zn enrichments in pyrite or marcasite are mostly related to masses or individual grains; conversely, Cu enrichments are mainly observed in pyrite developing primary textures (markedly framboids); this Cu-enrichment trend is not so clear in colloform marcasite.

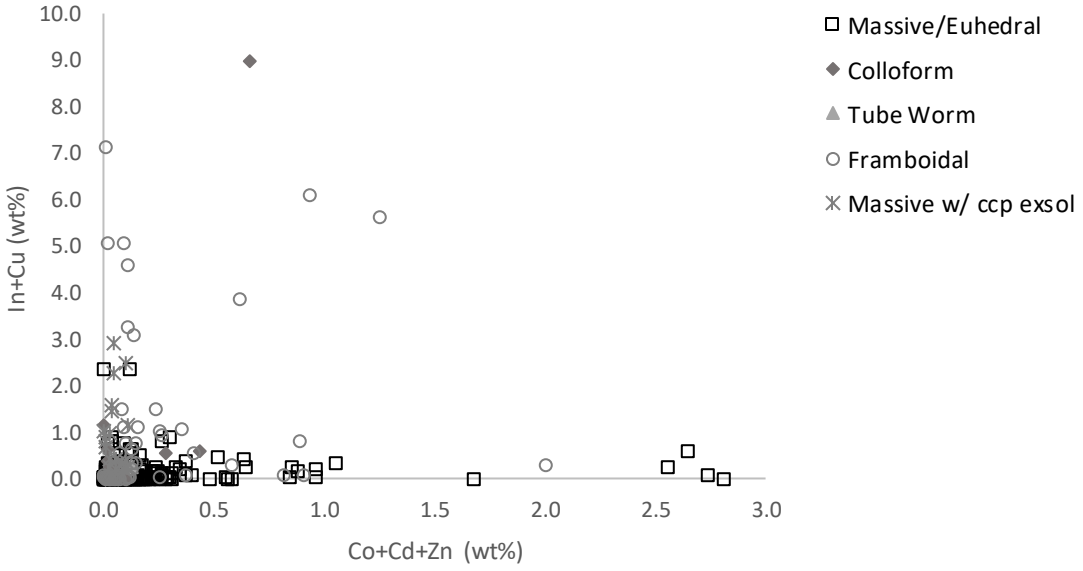

Fig 6. 4 - Bivariate diagram for textural discriminated pyrite analyses.

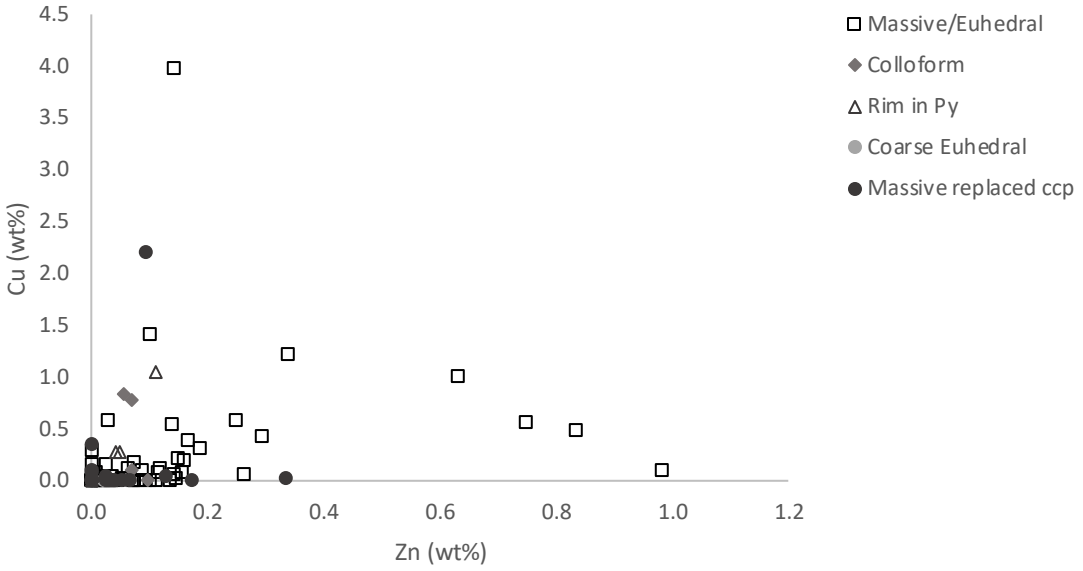

Fig 6. 5 - Bivariate diagram for textural discriminated marcasite analyses.

Some colloform structures revealed rhythmic alternation between pyrite and a Cu-rich phase, probably bornite. Fig 6.6 shows the EPMA image displaying an analysed profile, while the graphic puts in evidence the Cu, and Fe variations along the same profile. The Cu variation is evident, and such variations provide information on physical and chemical conditions during precipitation, allowing the identification of cyclic changes in the fluid chemistry.

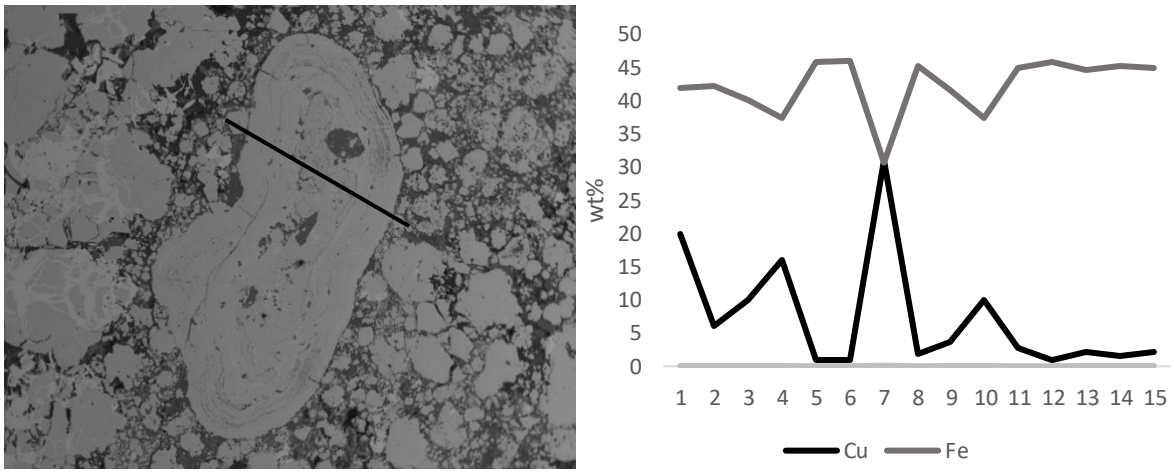

Fig 6. 6 – Pyrite colloform clast displaying the analysed profile. The graphic shows the Cu variations registered during the formation of that primary texture.

6.2 Cu Sulphide Phases

From all the Cu phases, chalcopyrite is the most abundant in the examined ore samples. Its composition is close to $FeCuS_2$, with $Fe_{0.901\text{-}1.148}$ and $Cu_{0.903\text{-}1.125}$; the estimated median composition for chalcopyrite in Mandoos 1 is $Fe_{0.966}Cu_{0.991}S_2$.

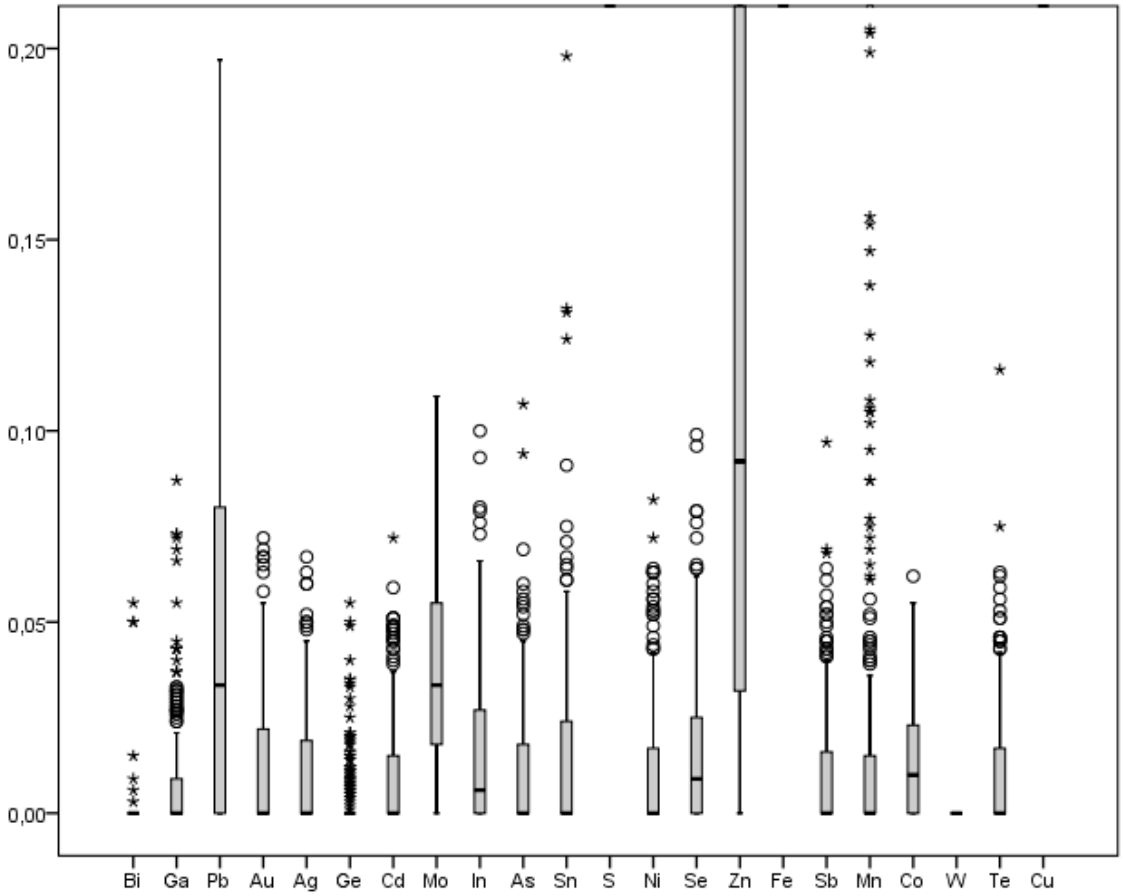

Fig 6. 7 - Box and whiskers plot for the multi-element concentration distributions displayed by 262 analyses of chalcopyrite (concentration values in wt%). Note the relative importance of Zn and Pb as trace elements.

The Fig.6.7 shows the distribution for all elements in the analysed chalcopyrite grains/masses. Clearly, the most relevant are the: (i) minor amounts of Zn, with median value of 920 ppm and maximum amount of 50290 ppm; and (ii) traces of Pb, Mo, In, Se and Co, displaying median values of 335 ppm, 335 ppm, 60 ppm, 90 ppm and 100 ppm respectively. The incorporation of a variety of elements by chalcopyrite, and the existence of a great number of outliers, suggest that no compositional refinement is observed in this mineral phase, also indicating that the development of chalcopyrite could be interpreted as a decaying product of a previous Cu-rich phase and in "transition" to other phases.

Bornite (Cu_5FeS_4) is also present, mostly replacing chalcopyrite. Its iron contents are less variable than those of copper ($Fe_{0.988\text{-}1.065}$ and $Cu_{4.710\text{-}4.946}$) and a median composition of $Fe_{1.005}Cu_{4.849}S_4$ can be calculated on the basis of analyses compatible with the bornite stoichiometry. As in chalcopyrite, Zn and Pb are the most significant trace elements, with amounts ranging from 150 to 9060 ppm and up to 1420 ppm, and median values of 1900 ppm and 880 ppm, respectively. The measured contents of Ag, Mo and In are also non-negligible, reaching up to 520 ppm, 550 ppm and 790 ppm, with median values of 150 ppm, 260 ppm and 130 ppm respectively (Fig 6.8).

Many other Cu-rich phases were analysed, optically undistinguishable under the current petrography. These were characterised and processed as a group of Cu-rich sulphides, separately from chalcopyrite and bornite. Variable in composition, these Cu-rich phases display copper contents from 22.359 to 72.772 wt% (median = 53.250 wt%), and iron concentrations from 1.253 to 34.715 wt% (median = 13.703 wt%); they also show significant amounts of Zn, up to 25 wt% (including an extreme outlier), characterised by a median value of 4220 ppm. As can be seen in Fig 6.9, significant trace amounts of Pb, Ag, Mo and Te were measured, displaying median values of 565 ppm, 215 ppm, 335 ppm and 435 ppm, respectively, and maximum concentrations up to 2930 ppm, 1330 ppm, 770 ppm and 73480 ppm, following the very same order.

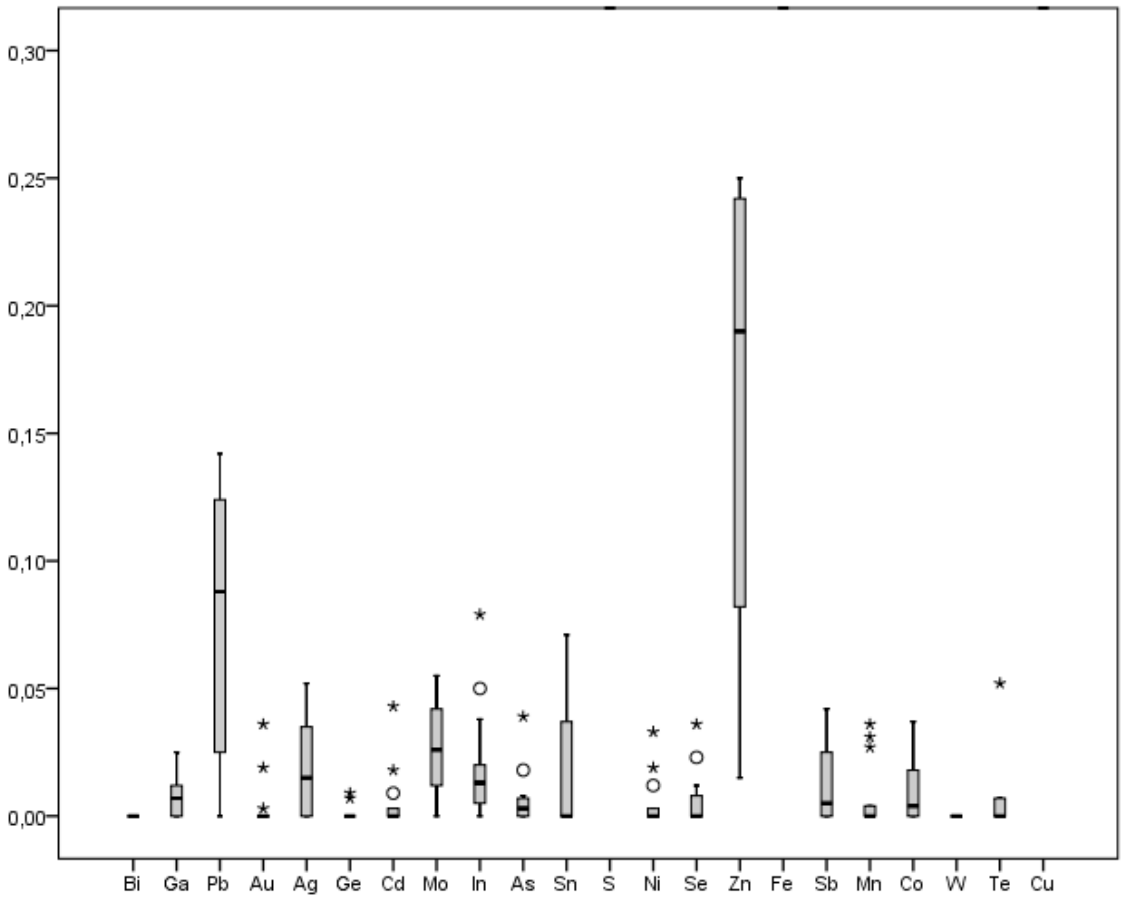

Fig 6. 8 - Box and whiskers plot for the multi-element concentration distributions (values in wt%) displayed by 13 analyses of bornite being Zn and Pb the most significant trace elements.

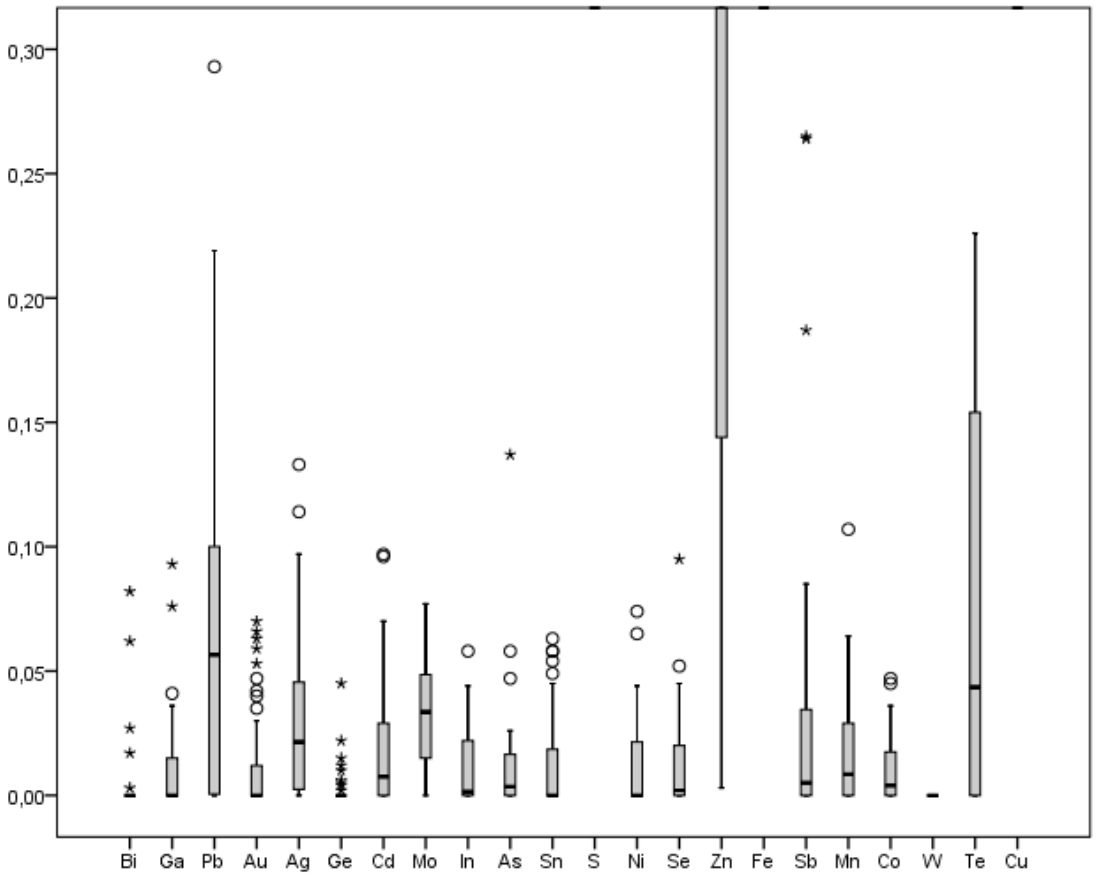

Fig 6. 9 - Box and whiskers plot for the multi-element concentration distributions (values in wt%) displayed by 64 analyses of Cu-rich phases showing minor/trace amounts of Zn, traces of some other elements are noteworthy, namely Pb, Ag, Mo and Te.

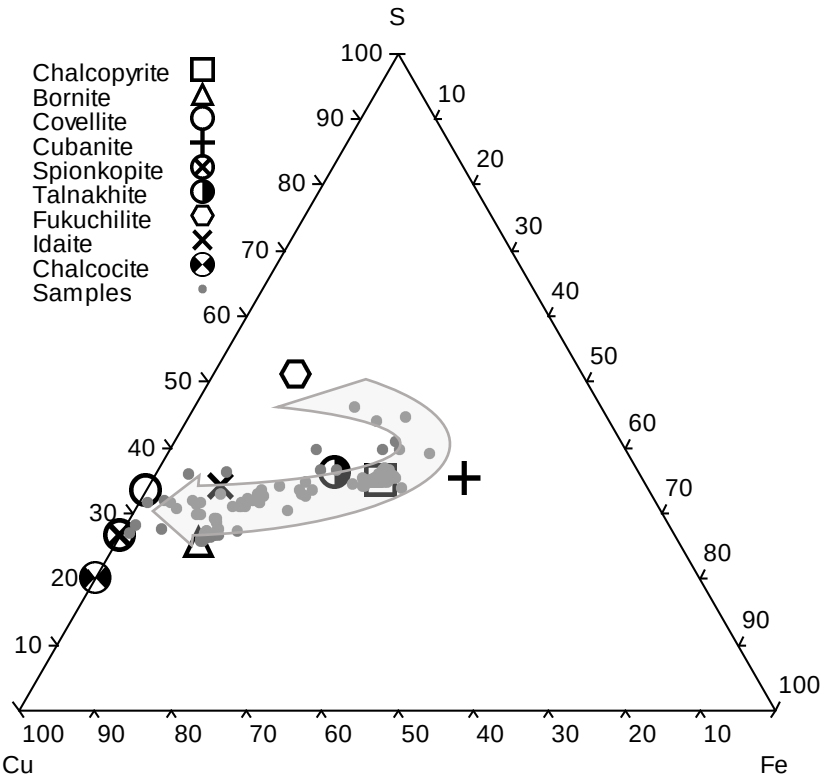

Fig 6. 10 - Ternary diagram showing oxidation trend in Cu phases.

When plotted in a ternary diagram, chalcopyrite samples are displayed around its ideal composition; the same happens with the clustering of bornite samples nearby its end-member. The non-stoichiometric compositions develop a relatively continuous trend that can be interpreted as a result of an evolutionary feature, starting near a fukuchilite-like composition (a high-temperature sulphide of ideal composition Cu_3FeS_8) and progressing towards cubanite-like ($CuFe_2S_3$) compositions, before reaching chalcopyrite ($CuFeS_2$), followed by a clearly marked oxidation trend in the direction of bornite (Cu_5FeS_4) and spionkopite ($Cu_{1.23}S$) and covellite (CuS) end-members.

6.3 Sphalerite

Sphalerite [(Zn,Fe)S] is also common as an accessory mineral phase in the Mandoos 1 sulphide ores. Its calculated median composition is $Zn_{0.952}Fe_{0.021}S$ and the distribution of zinc and iron ion contents confined to the following intervals: $Zn_{0.576\text{-}0.999}$ and $Fe_{0.002\text{-}0.210}$. Besides Fe, minor/trace amounts of Cu and Cd are meaningful, rising up to grades of 9.861 wt% and 0.673 wt%, respectively; concentration distributions of these elements are, however, asymmetrical, presenting medians of 2610 ppm and 2020 ppm. Also asymmetrical are the distributions of some meaningful trace amounts, such as Pb, As, Se, Mn, Co, W and Te. These elements show maximum values up to 4960 ppm, 1770 ppm, 1020 ppm, 41300 ppm, 1010 ppm, 2930 ppm and 1430, and their median contents are of 120 ppm, BDL, 50 ppm, 110 ppm, 30 ppm, BDL and BDL respectively. The elements showing median values below detection limit are characterised by third quartile values of 140 ppm, 520 ppm and 145 ppm respectively. Mo also has significant trace amounts, but in opposition, it displays a quasi-normal distribution with median of 560 ppm and amounts up to 1250 ppm (Fig 6.11).

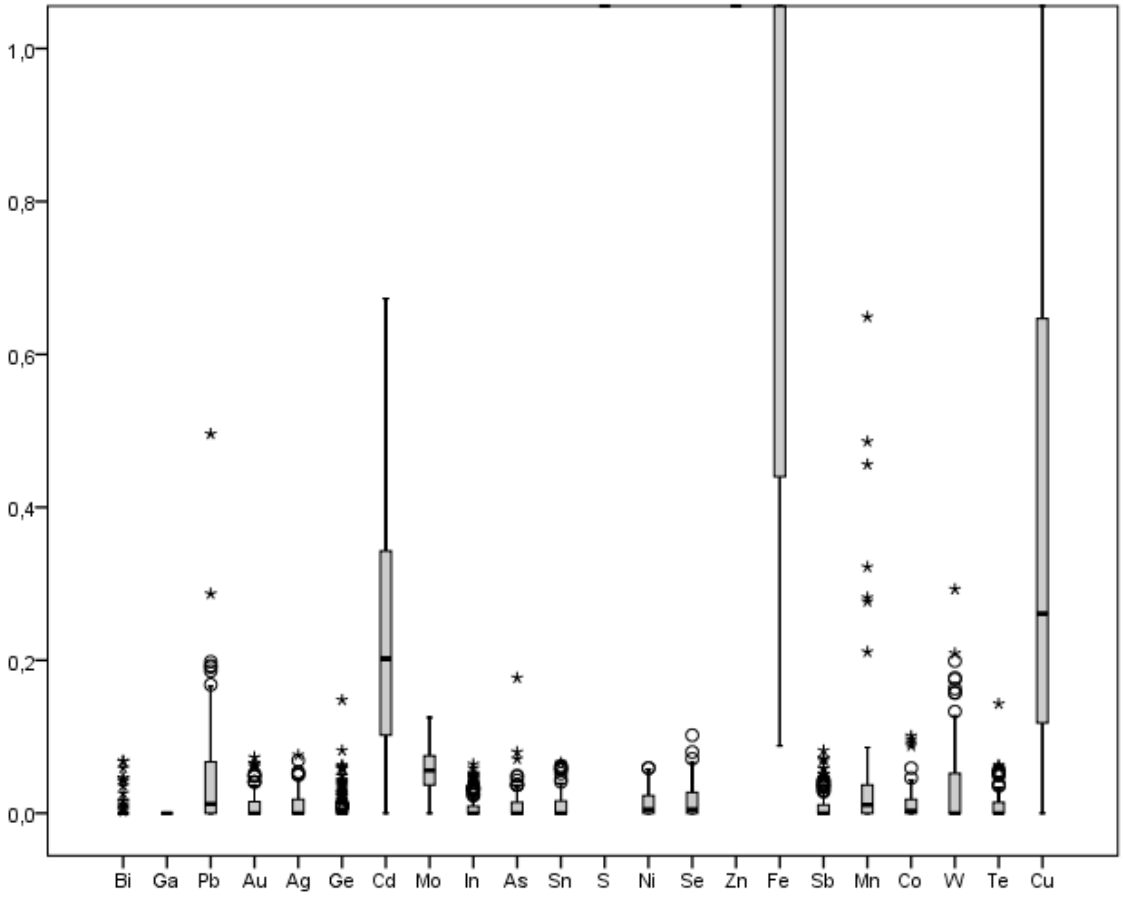

Fig 6. 11 - Box and whiskers plot for the multi-element concentration distributions displayed by 181 analyses of sphalerite (values in wt%). Minor/trace amounts of Cu and Cd are significant, traces of some other elements are noteworthy, namely Pb, Mo and W, between others.

Fig 6.12 shows a Fe versus Cd bivariant plot of all samples, distinguishing the textural arrangements where the chemical analyses for sphalerite were gathered. It is observed that sphalerites in Mandoos 1 are relatively poor in Fe, and those samples displaying "chalcopyrite disease" features are characterised by higher amounts of Cd. Chemical analyses of wurtzite (distinguished from sphalerite under optical microscopy, mostly due to its typical platy habit), sphalerite in masses showing triangular chalcopyrite intergrowths ("vent" texture), and sphalerite with fibrous texture or occurring in veins/fractures share similar compositional characteristics in this plot, i.e. low contents of Fe and Cd (Fe < 1.5 wt%; Cd < 0.4

wt%). Sphalerite forming massive/grain textural arrangements display two different trends, one towards Cd enrichment (with low contents of Fe) and another towards Fe enrichments, showing low amounts of Cd. The largest variation in Fe contents is recorded by sphalerite inclusions in pyrite, conceivably due to the "contamination" of the host mineral.

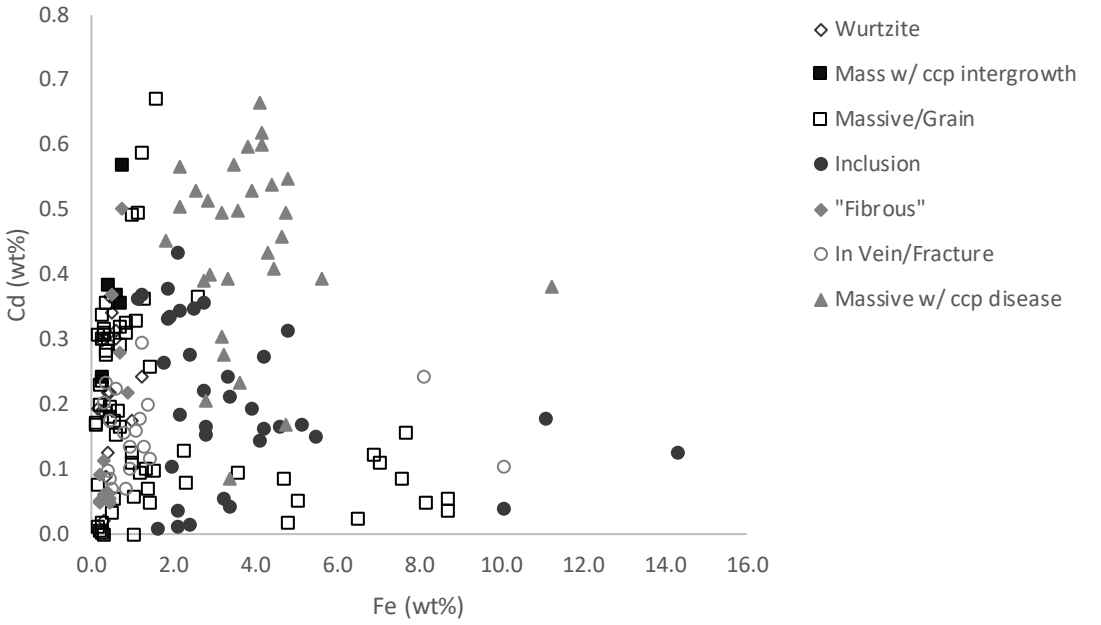

Fig 6. 13 - Bivariate diagram for textural discriminated sphalerite analysis.

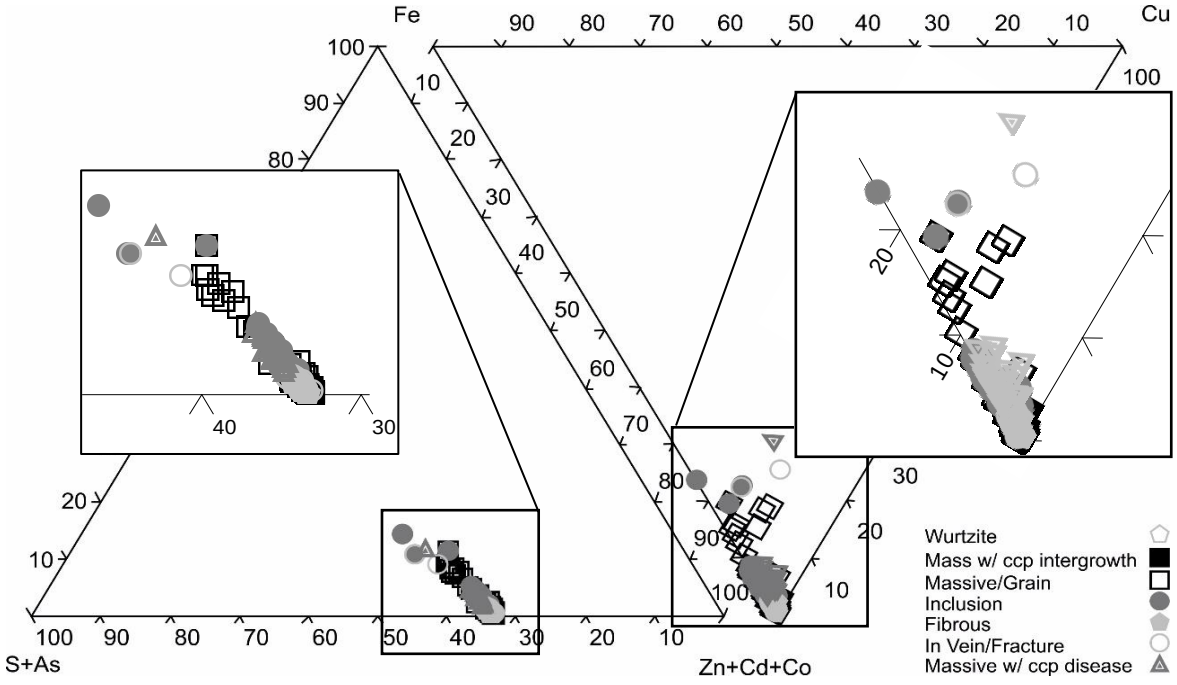

Fig 6. 12 - Ternary (S+As)–Fe–Cu– (Zn+Cd+Co) diagrams putting in evidence compositional dislocations towards Fe and Cu in sphalerites.

In the S+As – Fe – Cu – Zn+Cd+Co diagram it is observed that wurtzite, massive sphalerite with chalcopyrite intergrowth, veins and fibrous chalcopyrite are all plotted close to the S+As – Zn+Cd+Co axis, overlaying the sphalerite ideal composition and showing no significant variations towards Fe enrichments. The same happens when Cu is added; thus, all samples are clustered in the Zn – Cd – Co vertex. However, a distinct trend towards a minor Fe enrichment is observed in sphalerite samples displaying "chalcopyrite disease" features, forming massive aggregates and developing inclusions in pyrite, being the first sphalerite type less Fe-enriched than the last two cases. These three different textural arrangements also display a slight enrichment in Cu along with some sphalerite in veins.

6.4 Galena

Galena (PbS) is the less represented sulphide in all the studied samples. Indeed, tiny grains of galena are present in some samples, but their reduced dimension does not always allow the achievement of acceptable quantitative chemical analyses. The available data point to Pb contents varying from 0.976 and 1.005 atoms per formula unit, and a median composition of $Pb_{0.976}S$. Although irregular, minor amounts of Zn, Cu, Sb and Fe are present (Fig 6.14). These can go up to 20550 ppm, 5030 ppm, 2700 ppm and 3410 ppm, and display median amounts of 10770 ppm, 3810 ppm, 1130 ppm and 1170 ppm, respectively. The most significant trace amounts recorded are Sn, Se and Co; they are characterised by median values of 110 ppm, 100 ppm and 100 ppm and amounts that can reach 410 ppm, 690 ppm and 380 ppm, respectively.

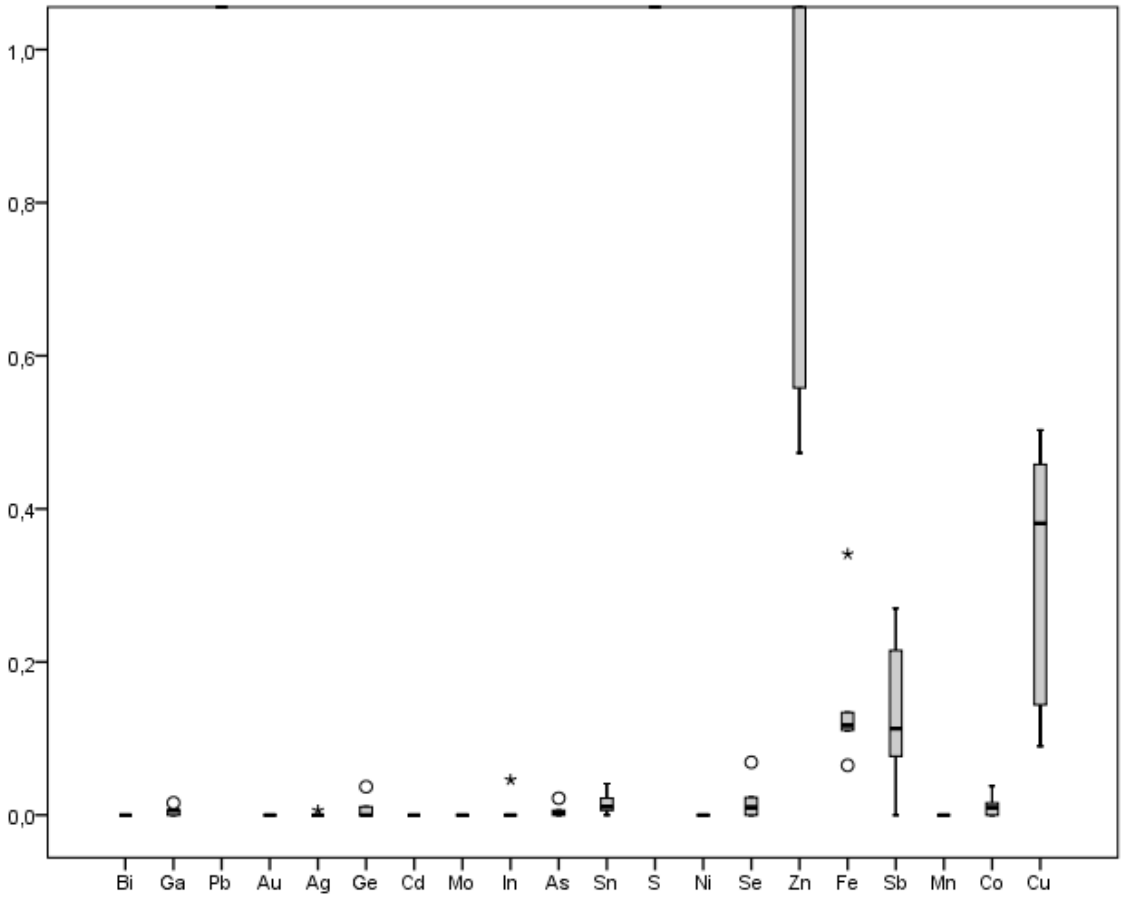

Fig 6. 14 - Box and whiskers plot for the multi-element concentration distributions displayed by 5 analyses of galena (concentration values in wt%). Note the relative importance of Zn, Cu, Sb and Fe as minor/trace elements.

7. Whole-Rock Chemistry

From the 42 samples collected during the sampling survey, 18 were chosen for minor and trace element analysis via ICP-MS in the Géosciences Environnement Toulouse laboratory (Observatoire Midi-Pyrénées), Université of Toulouse III. The same samples were also analysed via XRF for major elements at the University of Aveiro facilities. The analysed set comprises samples from different types of massive sulphides (10), metalliferous sediments (6) and mineralised (sulphide-rich or Mn-rich) jaspers (2) (Appendix IX). Due to the limited number of samples, the correlation matrixes meanwhile calculated were not as discriminative as expected, although a simple descriptive statistical study for the minor and trace elements distributions was performed, and for major elements as well.

7.1 Major Elements

The major elements measured with XRF have concentration values consistent with the observations done during re-logging and petrography. Indeed, samples of the Mandoos massive sulphides are Fe-rich and Cu-Zn-poor ores, and their correspondent grades are scattered in the intervals 3.96-24.73 wt% (median = 18.99 wt% Fe), 0.12-2.45 wt% (median = 0.51 wt% Cu) and 0.01-29.12 wt% (median = 0.048 wt% Zn) respectively, as can be seen in Fig 7.4. Silica contents are significant in these ores, rising up to 13.87 wt% and having a median value of 11.02 wt% SiO_2. These samples also contain Al and Ca, whose oxides display median concentration values of 0.097 wt% $Al_2O_3$and 0.024 wt% CaO and maximum contents of 5.46 wt% and 16.35 wt% respectively, following extremely asymmetric distributions. Sample MD-NP-1, a chalcopyrite- and sphalerite-rich ore sample, presents the highest Cu and Zn contents coupled with significant grades of SiO_2, Al_2O_3 and CaO mostly due to the presence of quartz and laumontite ($CaAl_2Si_4O_{12} \cdot 4H_2O$). As reported before, the ore samples are mostly breccias whose cement is enriched in SiO_2, and this fact explains the high-silica content displayed by most of the samples, excluding the specimens MD-P1-1-1 and MD-P3-4-1 which represent a massive pyrite accumulation and a breccia cemented by carbonates (thus displaying the highest content in CaO), respectively.

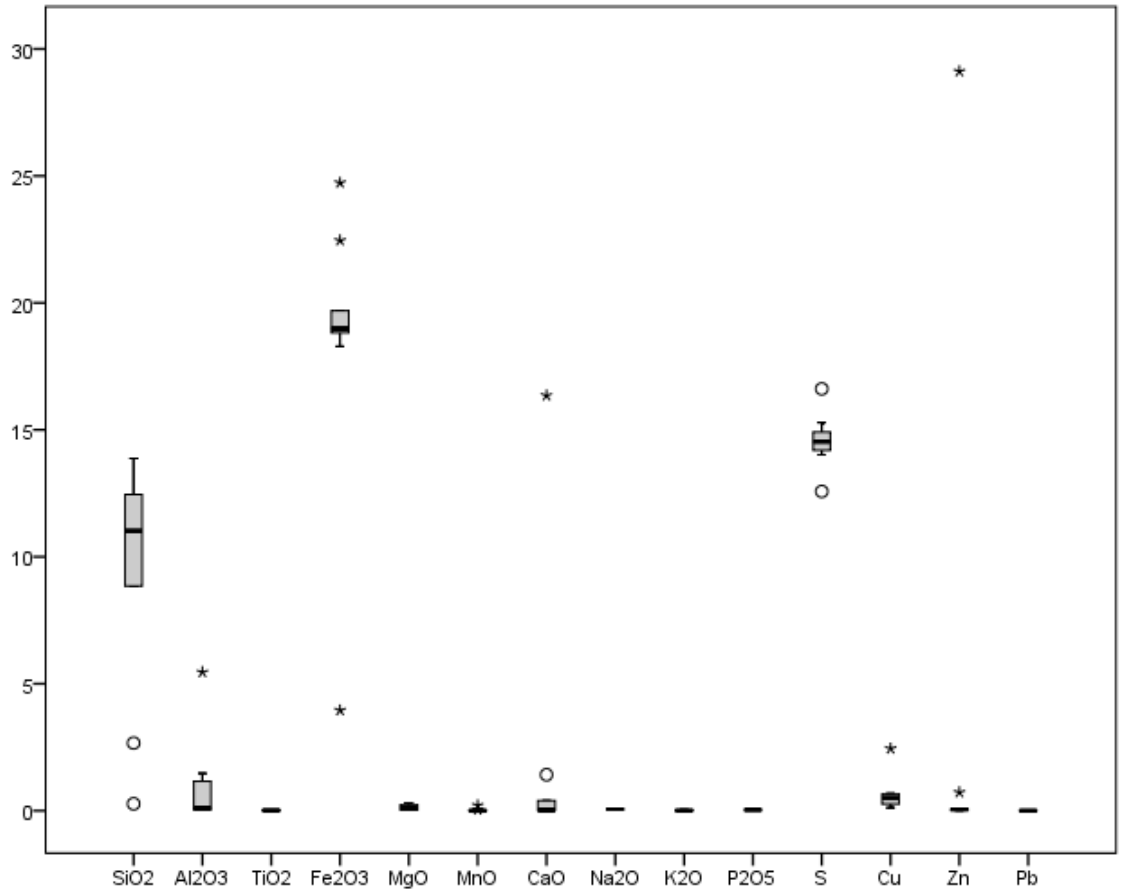

Fig 7. 1 – Major elements distribution in sulphide ores.

Umbers (Fe- and Mn-rich sediments) and ochres (Fe-rich sediments) (Fleet & Robertson, 1980) are the two metalliferous sediment types analysed in this section. As shown in Fig 7.2 (a), the Fe and Mn contents are discriminative enough to separate both rock types (umbers and ochres). These contents have their values scattered between 26.52-54.73 wt% Fe and 0.2-1.78 wt% Mn respectively. Besides the expected high-silica content, these samples also show CaO concentrations between 1.02 wt% and 12.61 wt% (median = 6.05 wt%). According to these results we may infer a set of 5 ochres and 1 umber (sample MD-178-110.5, with 1.78 wt% Mn). It is also possible to correlate the CaO contents with the presence of late carbonate veins, quite evident in sample MD-P2-2A, which is characterised by the highest contents of this oxide. Noteworthy is the Cu extreme outlier (maximum = 3.73 wt%) displayed by the sample MD-178-134.20, corresponding to a mineralised (massive sulphide) mineralised ochre.

Two different jasper samples were analysed, a mineralised sulphide-rich jasper (MD-150-114.10) and a manganese ore with jasper clasts (MD-NP-3); Fig 7.2 (b) shows clearly the discrepant composition of the two mineralised jasper samples, mostly in SiO_2 and MnO. These element oxides have minimum values of 10.45 wt% and 0.01 wt% and maximum of 30.05 wt% and 47.19 wt% respectively, being the latter value representative of the manganese ore (mainly pyrolusite – Appendix X). Also, the presence of minor amounts of Ba in the Mn-rich jasper sample is conceivably due to the presence of romanechite ($(Ba,H_2O)_2(Mn)_5O_{10}$) in the manganese ore.

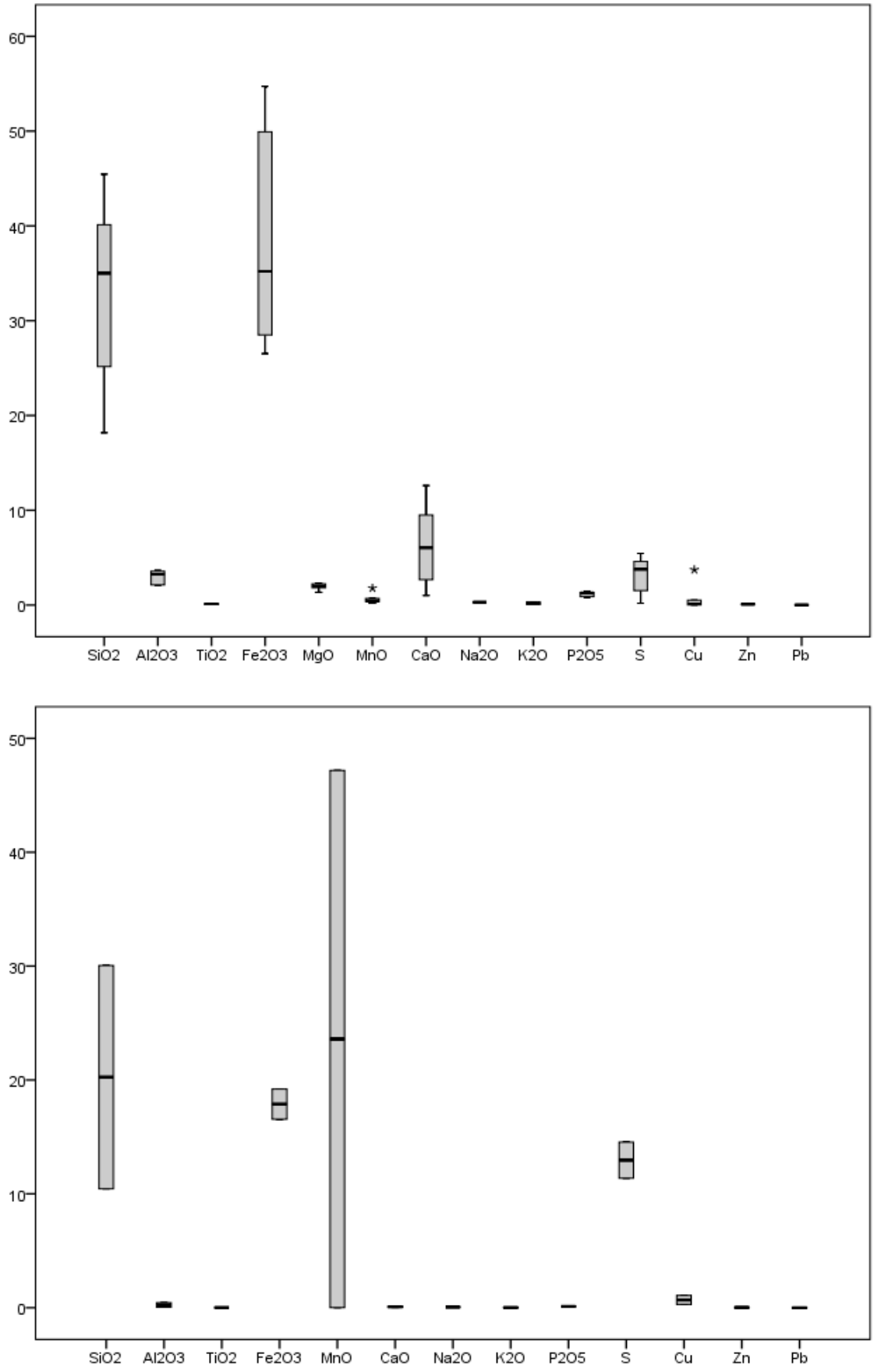

Fig 7. 2 – Major elements distributions in: A – umber and ochres; B – mineralised (sulphide-rich and Mn-rich) jaspers.

7.2 Minor and Trace Elements

As shown in Fig 7.3, minor amounts of V, Mn, Co, As and Pb can be found in massive sulphide samples, which display contents up to 67.15 ppm, 1887 ppm, 422.58 ppm, 1024 ppm and 219.97 ppm, respectively; for these elements, the median concentration values are of 43.74 ppm, 140.56 ppm, 37.78 ppm, 292.90 ppm, 53.27 ppm, by the same order. Also traces of Mo, Sn, Sb and Te are found in ore samples whose distributions are characterised by median values of 8.08 ppm, 6.07 ppm, 6.35 ppm and 12.46 ppm, respectively.

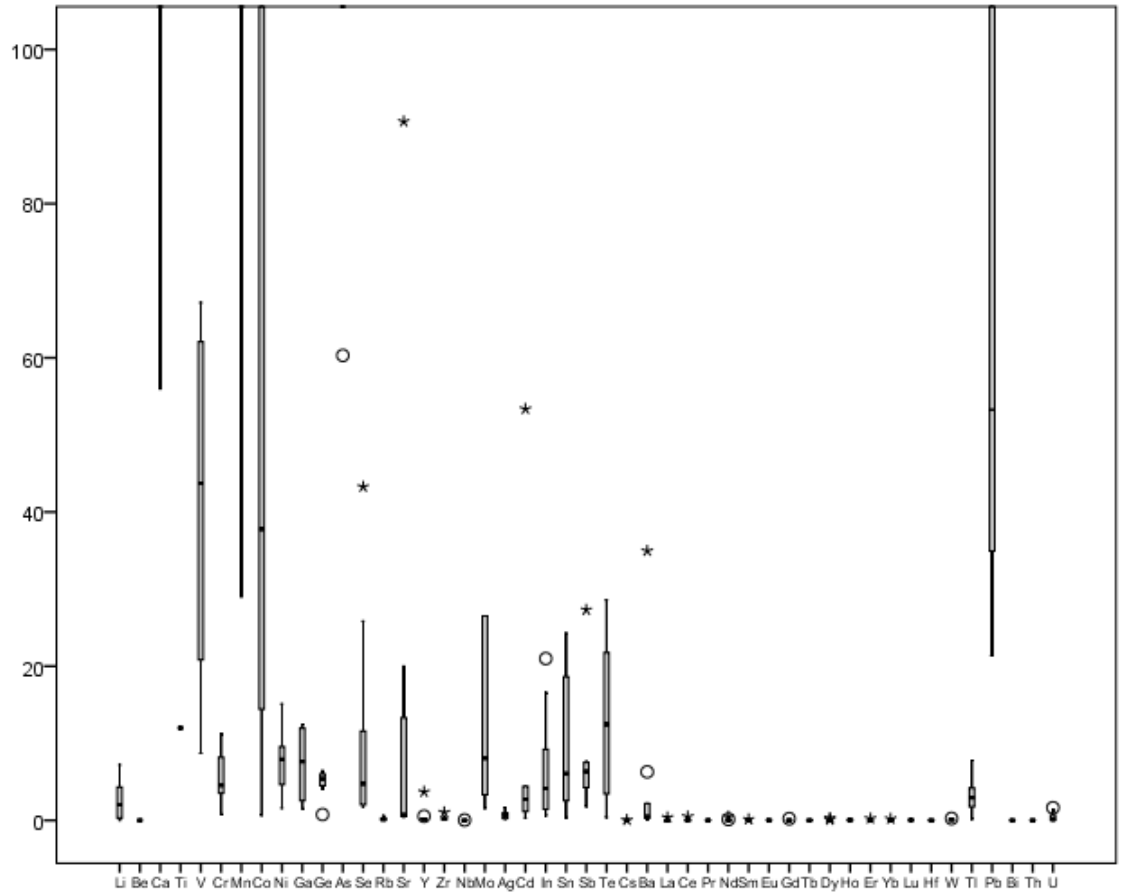

Fig 7.3 - Box and whiskers plot for the multi-element concentration distributions displayed by massive sulphides (concentration values in ppm).

The same set of minor elements is also found in metalliferous sediments, with the exception of Co and Pb, just with trace amounts. Other relevant elements found in metalliferous sediments and measured as traces are Cr, Ni and Sr (Fig 7.4); their correspondent grades are scattered within the 15.64-95.17 ppm, 35.1-185.4 ppm and 36.21-117.13 ppm intervals, respectively.

Despite having a restrict number of samples, whole-rock analyses of mineralised jaspers show strong consistency with the previous samples, displaying minor amounts of V, Co, Ni, As, Sr, Mo and Ba and some traces of Ga, Te and Pb (Fig 7.5). The median values of 217 ppm, 67.61 ppm, 88.8 ppm, 287.62 ppm, 224.86 ppm, 165.55 ppm and 372 ppm typify the concentration distributions of the aforementioned minor elements.

To date there were no data available for minor and trace elements in samples representing the Sumail ophiolite massive sulphides, being this exploratory work a further step in the characterisation of these ores.

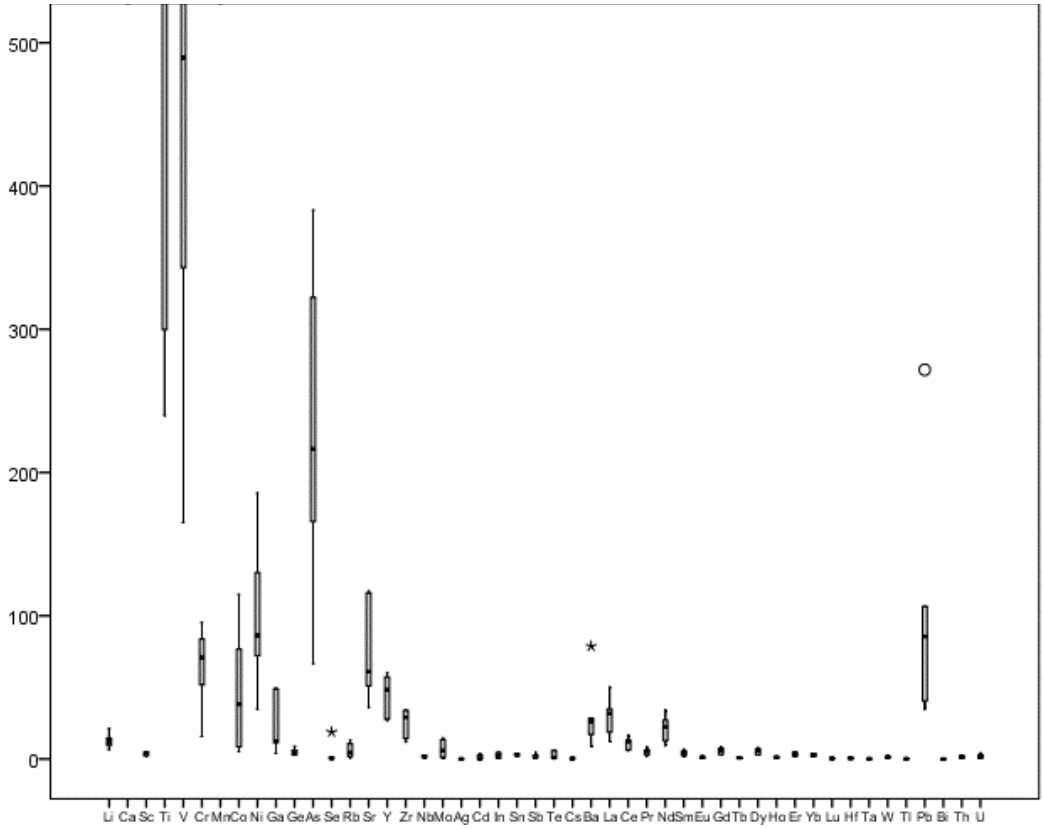

Fig 7. 4 - Box and whiskers plot for the multi-element concentration distributions displayed by metalliferous sediments;

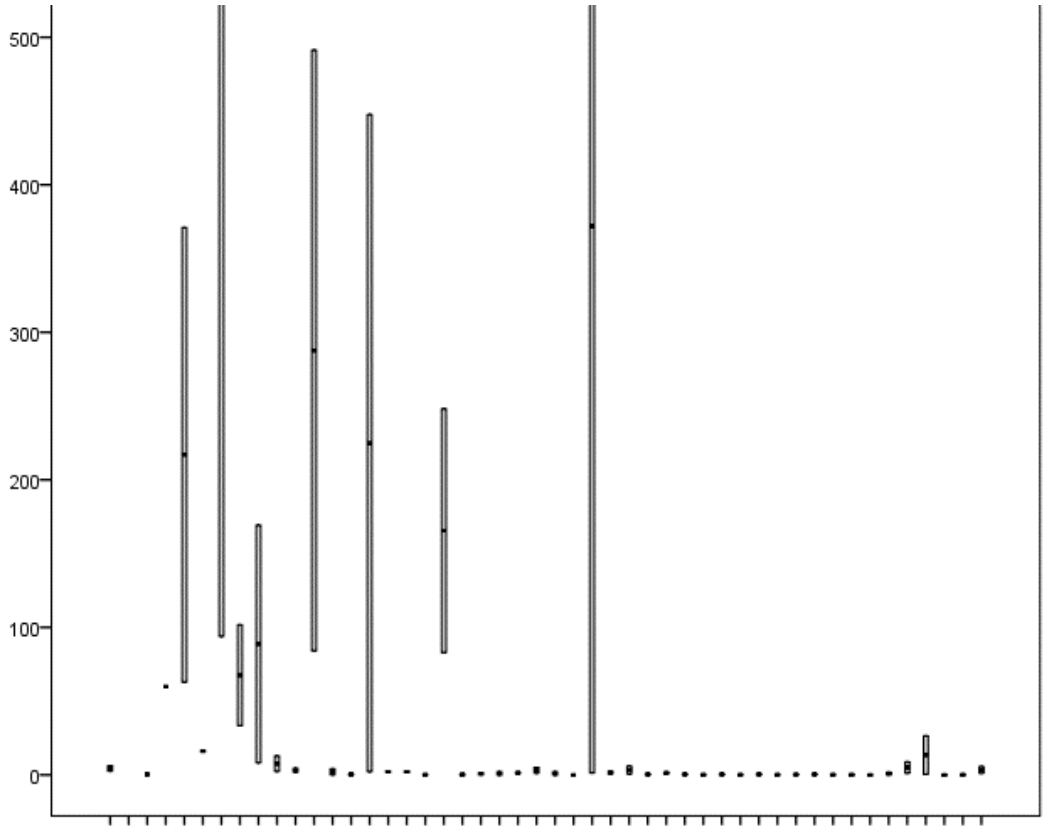

Fig 7. 5 - Box and whiskers plot for the multi-element concentration distributions displayed by jaspers (concentration values in ppm).

7.3 REE

The measured REE contents were normalised to C1 Chondrite (Palme & Jones, 2004) allowing direct comparison of patterns displayed by each set of samples (sulphide ores, metalliferous sediments and jaspers). In this approach, the relative enrichment and depletion of Eu and Ce were evaluated according to the Eu/Eu* and Ce/Ce* ratios defined as (McLennan, 1989): $Eu/Eu^* = Eu_N/(Sm_N \cdot Gd_N)^{0,5}$ and $Ce/Ce^* = 5Ce_N/(4La_N + Sm_N)$.

All the samples representing sulphide ores (Fig 7.6A) are depleted in REE, as expected; their normalised patterns are regular, revealing a feeble, almost imperceptible, enrichment in HREE, along with a positive anomaly in Eu (Eu*= 1.15 to 1.84) and a slight negative anomaly in Ce (Ce*= 0.41 to 0.91). The sample MD-P3-4-1 represents a massive sulphide breccia cemented by carbonates and is the most REE enriched (≈1 to 2× C1) specimen of the entire set. This is possibly related to the incorporation of REE in carbonates. As seen in Fig 7.6, the REE normalised pattern characterising the sulphide ores can be explained by a mixture of vent fluids and seawater; with this simple mixture it is possible to obtain a slight enrichment in HREE and a Ce negative anomaly (inherited characteristic from the seawater) together with a Eu positive anomaly (the most distinctive feature of vent fluids).

Metalliferous sediments (Fig 7.6B) are the most REE-enriched samples, displaying a wide range of values. The REE normalised patterns are characterised by LREE relative enrichments along with slight HREE depletions. An evident negative anomaly in Ce (Ce*= 0.15 to 0.18) is shown in all samples, together with a feeble negative anomaly in Eu (Eu*= 0.73 to 0.82). When compared with the seawater pattern (Fig 7.6D) it is clear that their pattern indicates a REE scavenging of the ocean by adsorption in phyllosilicates forming the sediments.

Both jasper samples share similarities in the pattern shape, revealing relative enrichments in LREE and faint enrichments in HREE. Sample MD-NP-3 displays a weak positive anomaly in Ce (Ce*=1.19) and an evident negative anomaly in Eu (Eu*= 0.07), while sample MD-150-114.10 shows a negative anomaly in Ce (Ce*= 0.34) and a positive one in Eu (Eu*= 1.56). The mineralised sulphide-rich jasper displays a pattern alike of that showed by the sulphide ore sample MD-P3-4-1; like in sulphide ore samples, these REE normalised patterns suggest the development of mixtures of seawater and vent fluids but the former component (seawater) is now more important. The Mn-rich mineralised jasper shows a distinct REE normalised pattern, conceivably due to the geochemical behaviour of Ce (Ce^{3+} is soluble under reducing conditions, precipitating as Ce^{4+} in oxidizing conditions); The sample is mainly composed of pyrolusite ($Mn^{4+}O_2$), identified via XRD (Appendix X), so most of the Ce might be incorporated in the Mn^{4+} position.

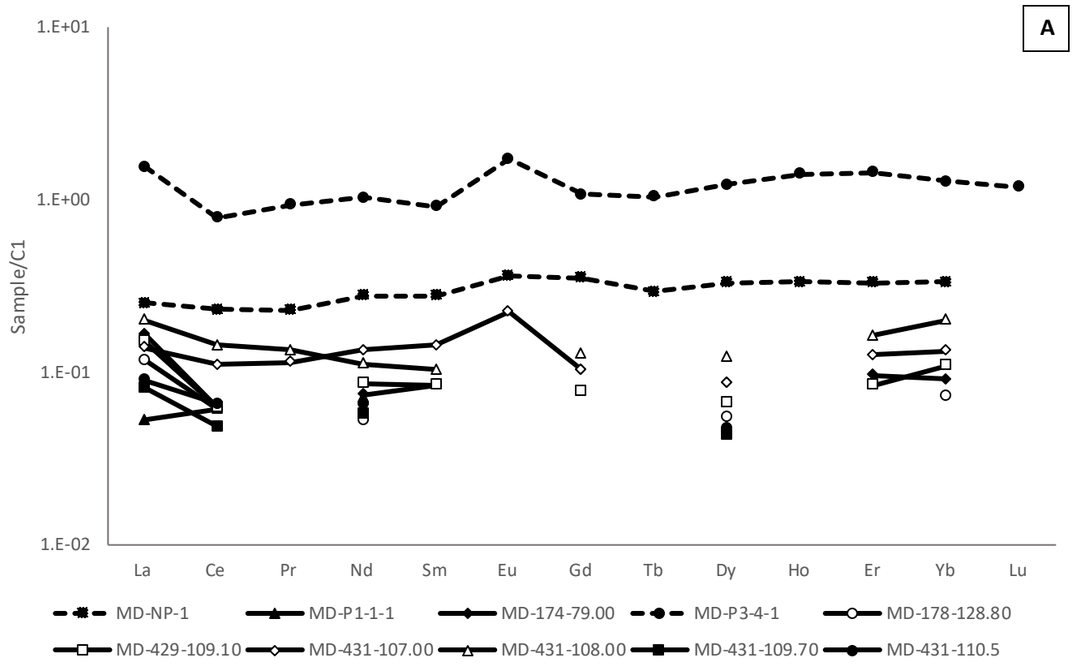

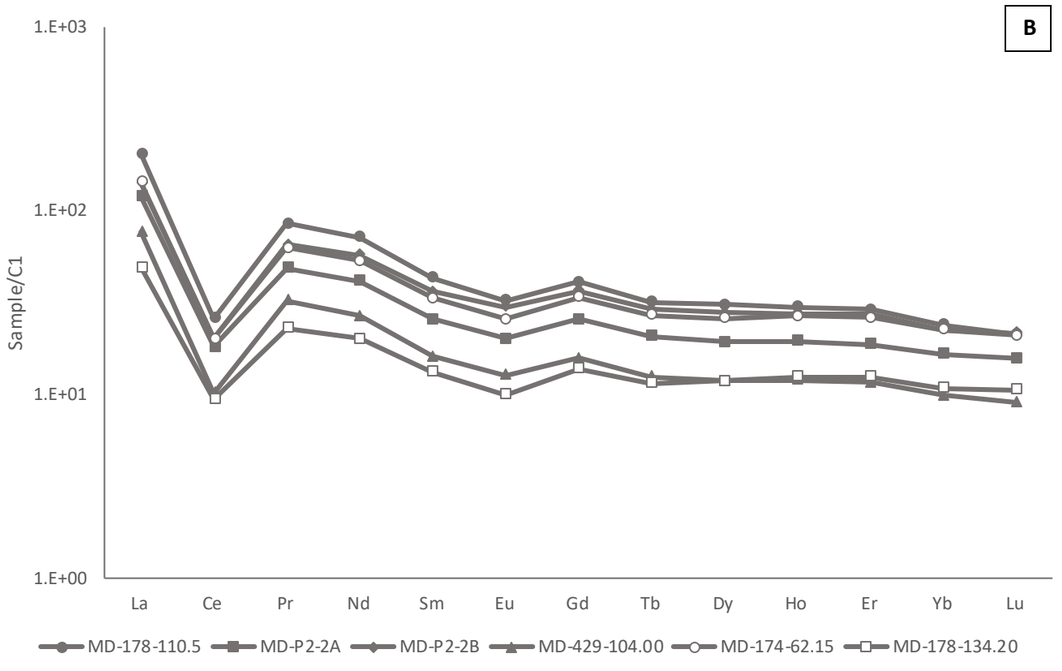

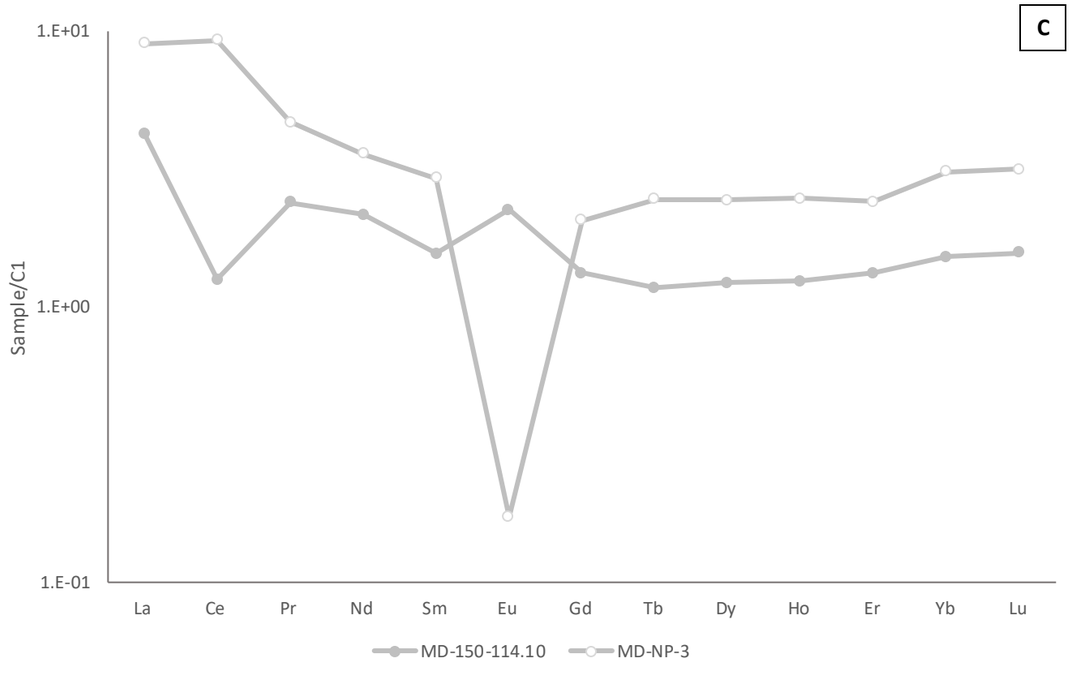

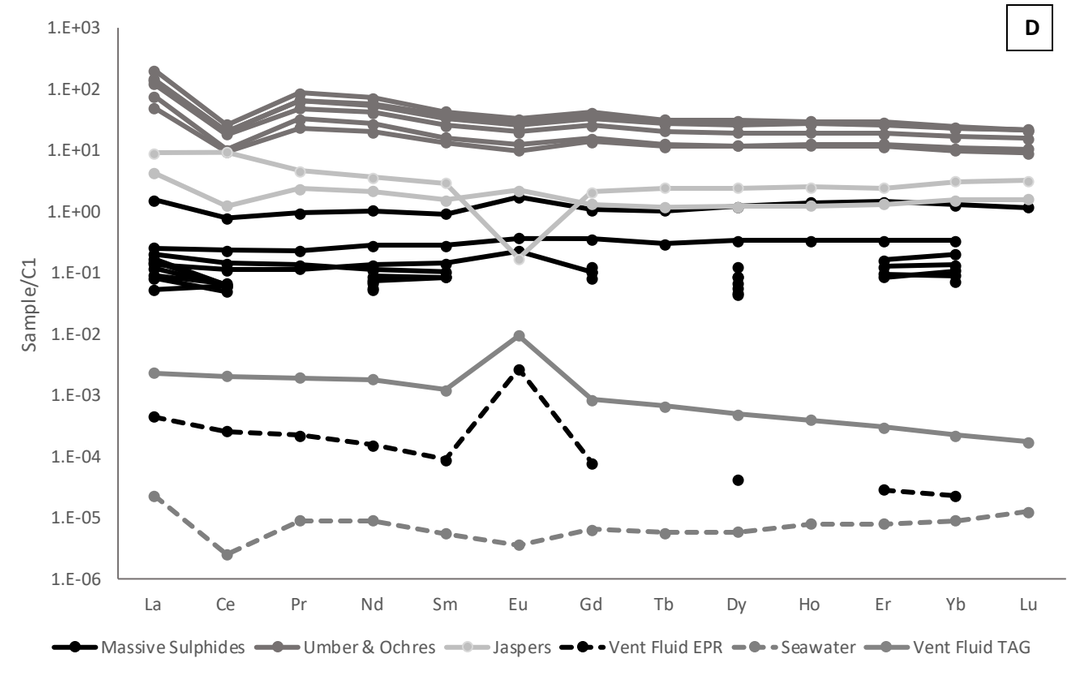

Fig 7. 6 – REE patterns for: A – sulphide ores; B – umber and ochres; C – mineralised jaspers; D – all the analysed samples together with representative REE normalised compositions of seawater (Li et al., 2004) and vent fluids (EPR (German et al., 1999) and TAG (Mills & Elderfield 1995)).

REE contents of metalliferous sediments from Troodos (Robertson & Fleet, 1976) and modern analogues from East Pacific Rise (Barret, 1988) were taken from literature for comparison purposes with the REE patterns obtained for Mandoos samples. All these sediments display a similar pattern despite of differences in relative abundances (denoting variable enrichment levels). The metalliferous sediments from Mandoos occupy an intermediate position between samples from Troodos, which are the most enriched in all REE elements, and from modern analogue settings (the lesser REE-enriched).

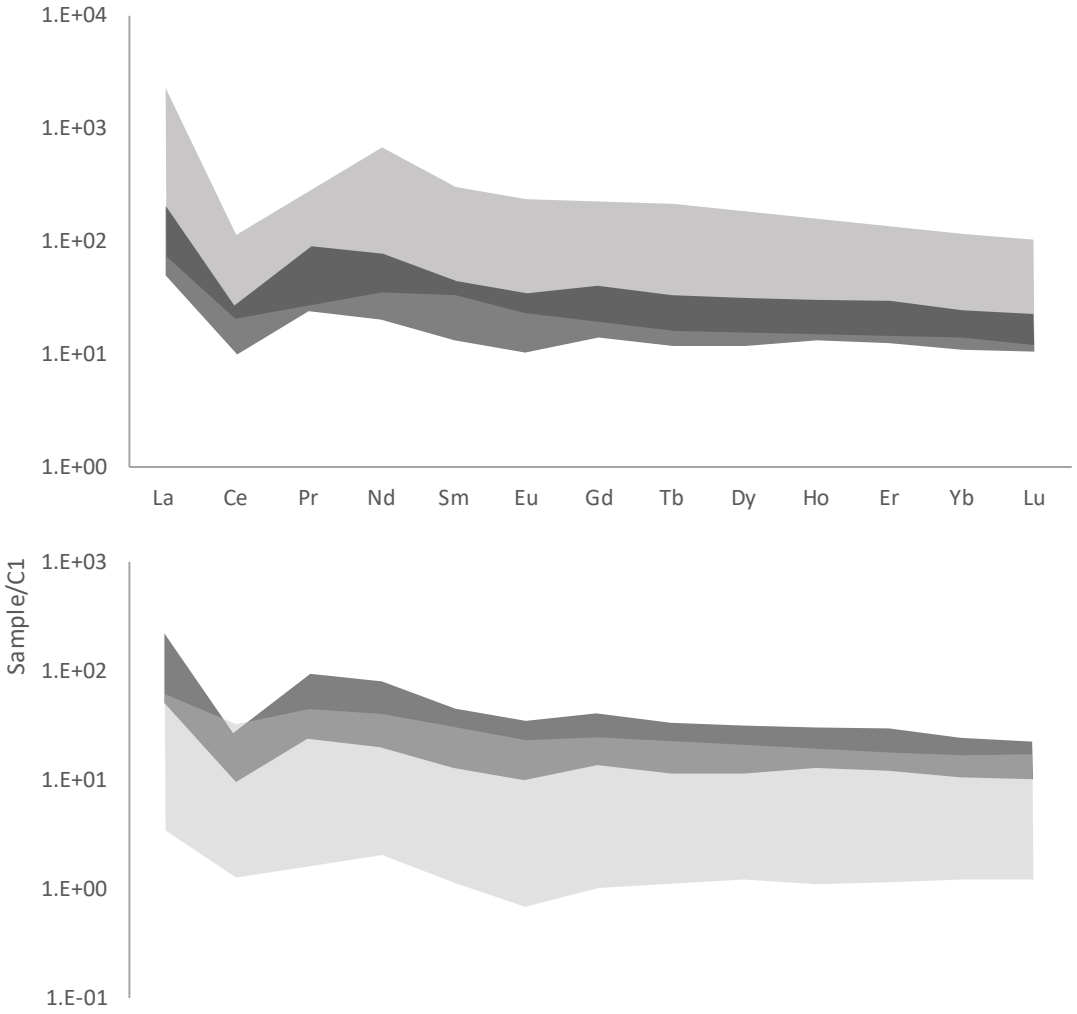

Fig 7. 7 – Comparison of metalliferous sediments REE normalised patterns: on top – Mandoos (black) and Troodos (dark grey); bottom – Mandoos (black) and EPR (light grey).

7.4 Spider Diagrams

Primitive mantle (PM) normalised (Palme & O´Neill, 2004) spider diagrams, using a set of elements organised by their atomic number, were used to characterise the Mandoos sulphide ores, metalliferous sediments and jaspers. The samples show common positive anomalies in Cu, As, Mo, In, Sb, Te, W and Pb, along with evident negative anomalies in Cr and Ni; Rb, Sr, Y, Zr, Nb and Th also show negative anomalies, but not so clearly.

Despite the positive anomalies in V and Co, the sulphide ores are still depleted, relatively to primitive mantle, in transition metals with the exception of Cu, Zn and As. Cu displays enrichment ≈340x PM, while As ≈4000 to ≈15000x PM, and Zn up to 10x PM (excluding sample MD-NP-1 which displays an Zn enrichment above 5000x PM). Depletion in Rb, Sr, Y, Zr, and Nb, as well as in REE and Th, are well marked. However, Mo, Cd, In, Sb, Te and Pb display an evident enrichment in all the sulphide ore samples. The Zn-rich sample (MD-NP-1) displays, as expected, a Cd enrichment above 60000x PM. The sulphide ore samples are also characterised by amounts of Mo between 50 and 2300x PM, Sb can vary from ≈300 to ≈5000x PM and Te between 40 and 3000x PM; the Pb positive anomaly denotes enrichment above 180x PM, never exceeding 1190x PM.

Metalliferous sediments are enriched in all the measured elements with exception of Sc, Ti, Cr, Co and Ni. Well-defined positive anomalies in P, V, Cu, As, Mo, Sb, W, Pb and U are observed in all samples; P displays enrichments from ≈40 to ≈70x PM, while As (the most enriched element) is characterised by values ranging from ≈980x PM to ≈5600x PM. W and Pb also display high levels of enrichment in these sediments; W varies from ≈45x to ≈180X PM, while Pb enrichments can reach amounts ≈1500x above the primitive mantle. The measured Mo, In, Sb and Te concentration are also significant in some samples, reaching maximums of 313x, 266x, 821x and 689x PM, respectively.

Jasper samples (MD150-114.10), represented by a mineralised sulphide-rich jasper and a manganese ore with jasper clasts (MD-NP-3), are relatively enriched in As, Mo, Cd, Sb, W and U when compared to the primitive mantle. The As values range between 1230x and 7230x PM; Cd contents may reach up to 5270x PM; and Sb concentrations remain below ≈1000x PM. In these samples, the U contents vary between 54x and 243x PM. Also noteworthy, are the enrichments in Ba (≈108x PM) and W (≈141x PM) in the MD-NP-3 sample, as well as in Cu (≈535x PM) and Pb (≈142x PM) in sample MD150-114.10.

Overall enrichments in Cd, In, Te, W, and Sn (observed in the minor and trace elements chapter) represents conceivable signals of magmatic inputs to the hydrothermal-mineralising fluids involved in sulphide deposition.

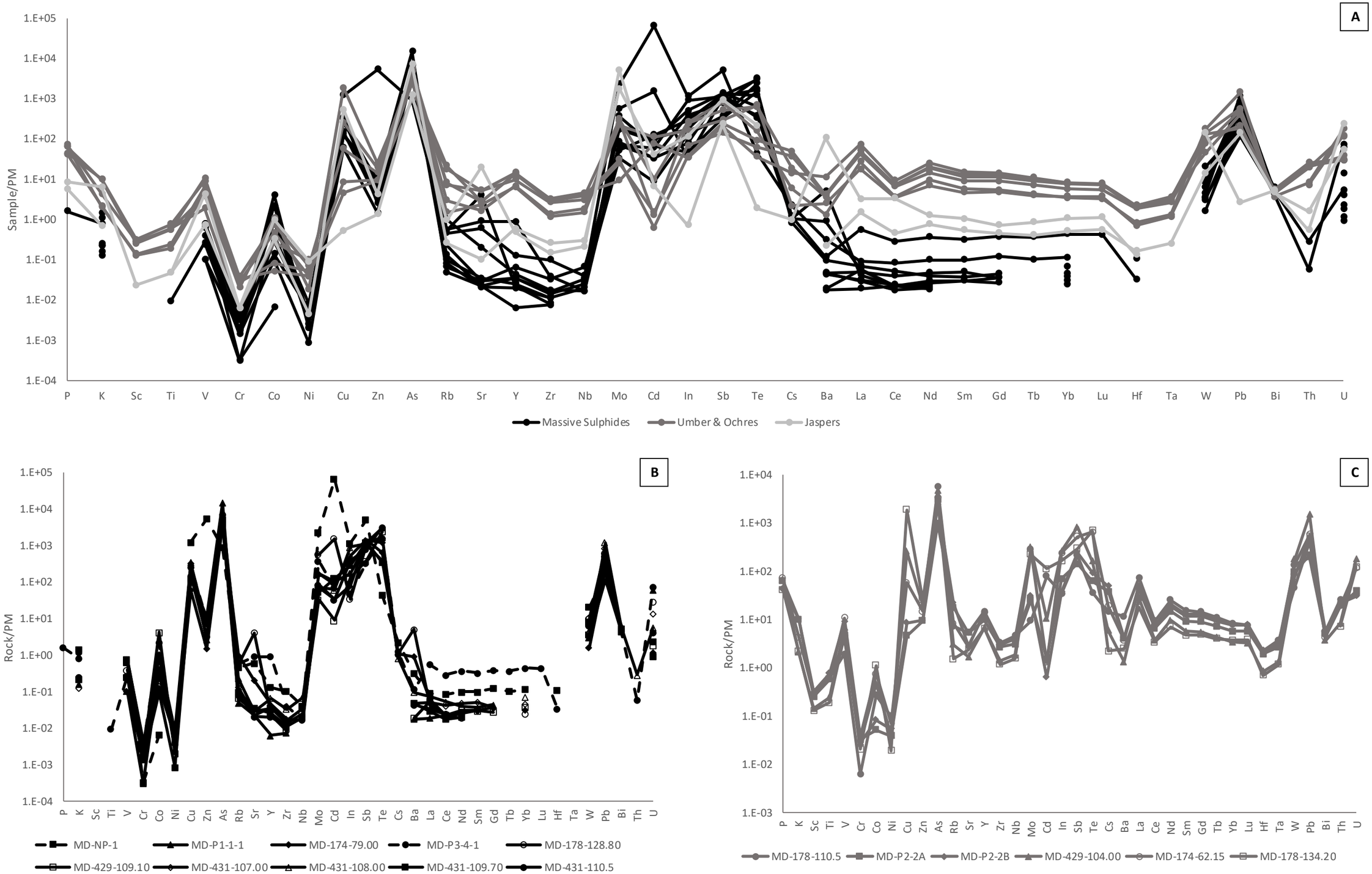

Fig 7. 8 - Normalised concentration patterns for Mandoos samples: A – all the analysed samples; B – sulphide ores; C – umber & ochres. Normalization values according to Palme & O'Neill (2004).

7.5 Immobile Elements

Since the relative mobility of elements in different geochemical settings is not a determined feature, being influenced by a wide number of features depending on element and/or environmental characteristics, it is crucial to test for each situation which elements present an immobile behaviour. Usually, various elements (such as Al, Zr, Ti, Nb, Y, Sc) tend to behave as immobile in a large assortment of geological processes and a common and simple approach to validate such relative immobility consists in plotting these elements against each other, resulting in a good positive linear co-variation that contains the origin.

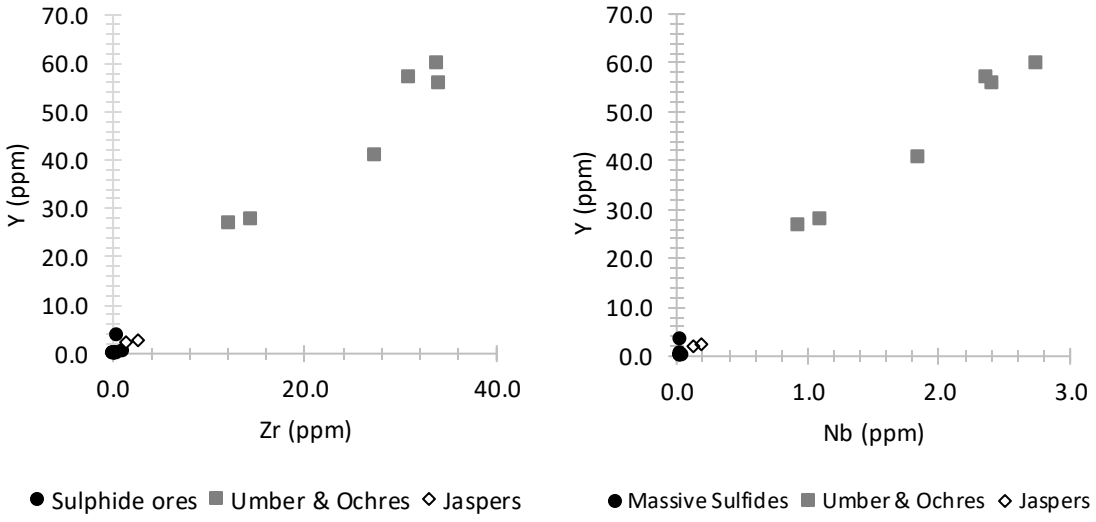

Fig 7. 9 – Y vs Zr and Y vs Nb plots showing the immobility of these elements.

The figure above (7.9) shows two examples of the plots obtained with the studied samples, indicating that Y, Zr and Nb can be considered geochemically immobile during the development of sulphide ores, mineralised jaspers and metalliferous sediments; according to the available data, La and Yb can also be

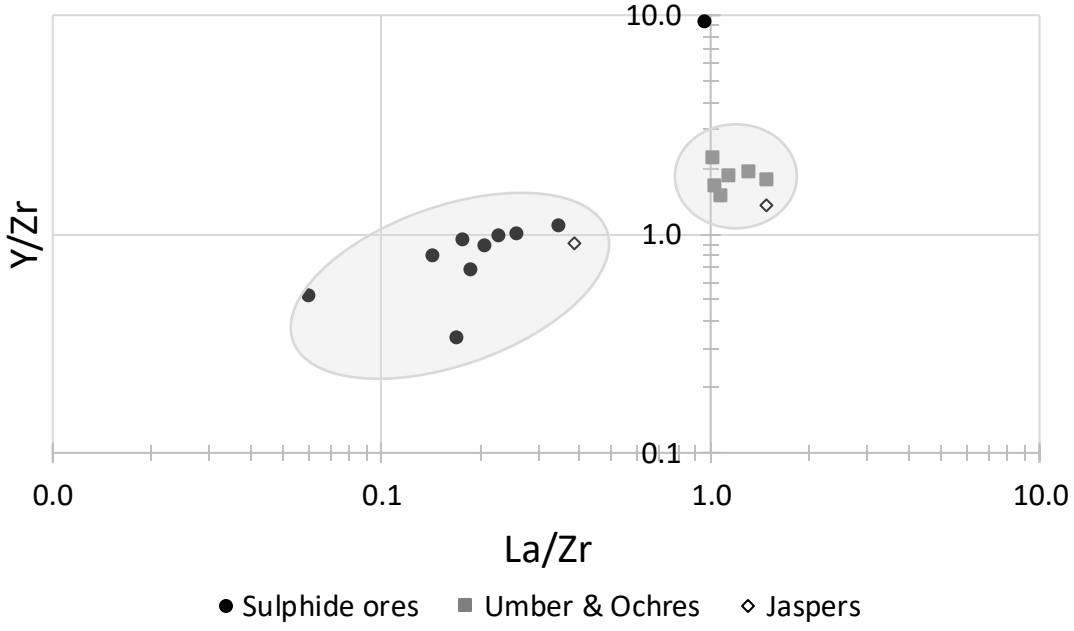

Fig 7. 10 – Y/Zr vs La/Zr plot showing two different sources for the studied samples.

classified as immobile. Using now the ratios between immobile elements, one may put in evidence the distinct sources (protoliths) related to the sulphide ores and hydrothermal sediments (Fig 7.10).

The plot La/Zr versus Y/Zr shown in Fig 7.10 is an example of that discrimination: a wide cluster that comprises the massive sulphide samples and a more constricted cluster involving all the metalliferous sediments (umber & ochres). Noteworthy is the presence of the jasper samples in both clusters, which is entirely consistent with the mineralogical characteristics of the analysed samples: sample MD-NP-3 (manganese ore) shares more affinities with metalliferous sediments; sample MD150-114.10, a sulphide-rich mineralised jasper is compositionally influenced by the mechanims related to the sulphide ore development. The deviation displayed by sample MD-P3-4-1 is ascribed to the relative abundance of late-formed carbonates in the sulphide breccia.

Normalising all the values to an immobile element will reduce the dilution factor, allowing to directly compare samples. For this exercise, Y was the immobile element chosen. Fig 7.11 compares all samples from the three different rock types collected during sampling: sulphide ores, umber and ochres and jaspers. A general inspection shows that all the samples display similar patterns; however: sulphide ores are the most chemically enriched; metalliferous sediments are the less chemically enriched; and jaspers occupy an intermediate position between those two "end-members".

A closer look into individual groups allow to better evaluate the enrichment factors; sulphide ores are mainly enriched in SiO_2, Fe_2O_3, S, As, Sr, Mo, Ta and Tl. Sample MD-P3-4-1 displays a slightly different pattern, also with the particularity of being the less-enriched sample amongst all sulphide ores, as expected (mineralised breccia cemented by carbonates). Samples MD-NP-1 and MD-178-128.80 show evident enrichment in Zn and Cd not registered in other samples, which is compatible with the observed significant amounts of sphalerite. Noteworthy is also the enrichment in Te in many samples.

Metalliferous sediments (Fig 7.11C) show enrichment in SiO_2, Fe_2O_3, CaO, As, Sr, Ba and U. Major variations amongst these samples are in Cu, Cd, Te and Ta, whose enrichment factors can vary from tens to 1000x between them.

Jaspers present two different patterns but with common enrichments in SiO_2, Fe_2O_3, S, As, Mo and U. The MnO, Ba and Sr enrichments in sample MD-NP-3 are significantly higher (1000x and 100x, respectively) than those recorded by the sulphide-rich mineralised jasper.

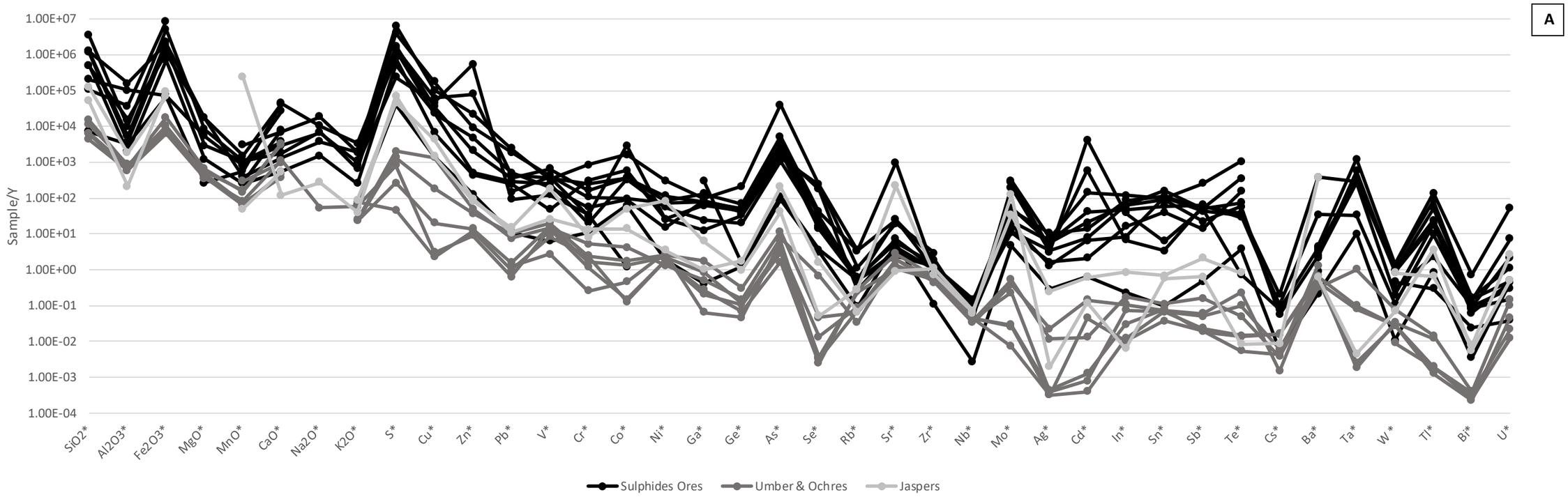

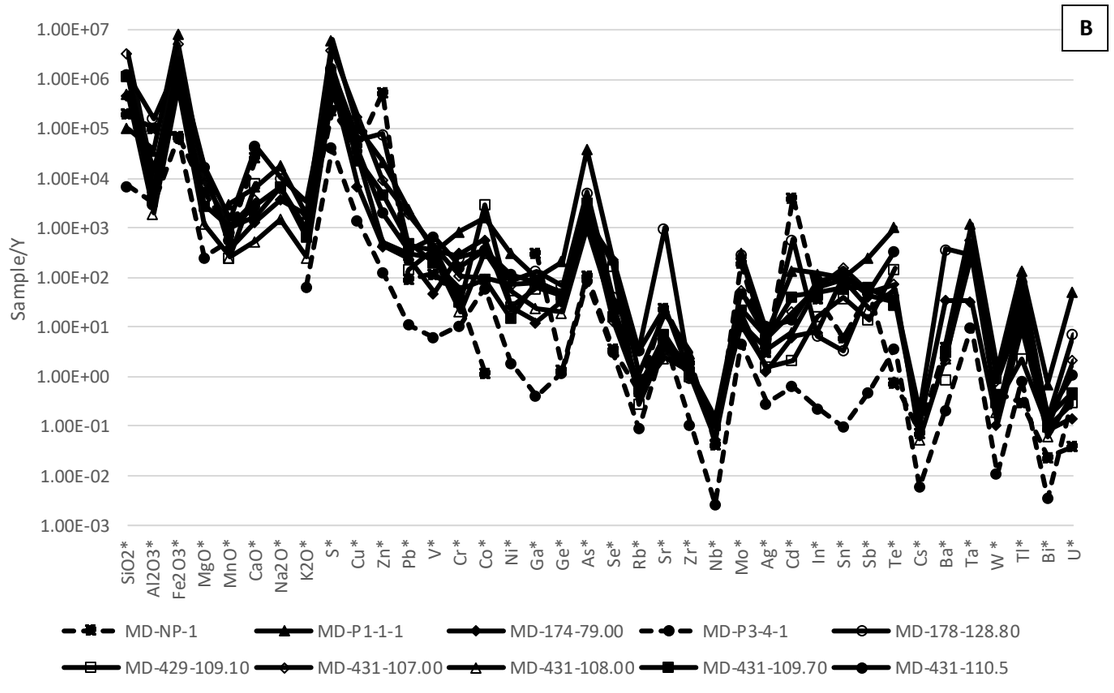

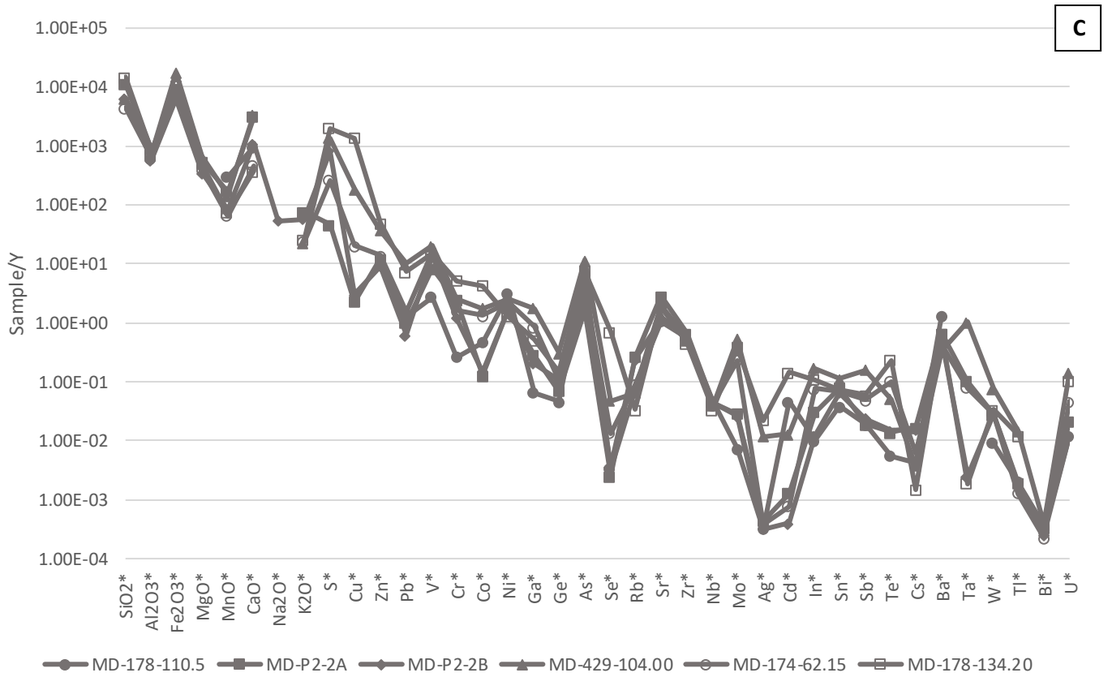

Fig 7. 11 – Normalised (Y) concentration patterns for Mandoos samples: A – all the analysed samples; B – sulphide ores; C – umber & ochres.

8. Discussion

Mafic type deposits are described as Cu-rich and Pb-poor when compared to other VMS deposits (Barrie & Hannington, 1999). The geometric mean of metals concentration in sulphide ores from different VMS deposits in distinct host-rock settings are reported in Hannington (2014). Fig 8.1 exhibits the distribution of these geometric mean concentrations in a Cu-Pb-Zn diagram, showing that the majority of VMS deposits are plotted in the Zn-Pb-Cu field, while the mafic-type deposits are distributed within the Cu-Zn-rich field. The studied VMS samples from Mandoos 1 deposit were also included in this diagram, represented by the median values of the available concentration metal distributions (marked as Mandoos). Mandoos 1 is plotted in the Cu-type field, being relatively enriched in Cu when compared to other mafic-type deposits. The 8 Mt orebody displays an average grade of 1.72 wt% Cu, which showed to be slightly below the assessed value, although this might be explained by the incomplete database provided by the company, which only made available the survey for 33 drill holes. Petrography and mineral chemistry did not present evidence for zone refining, and the modelling of Cu and Zn grades also did not also document a metal zoning in the deposit. Nonetheless, it can be shown that (at least) part of the observed Cu enrichment comes from secondary Cu-rich phases developed in the course of a more oxidising (late) evolving event. As previously stated, the presence of numerous primary textures

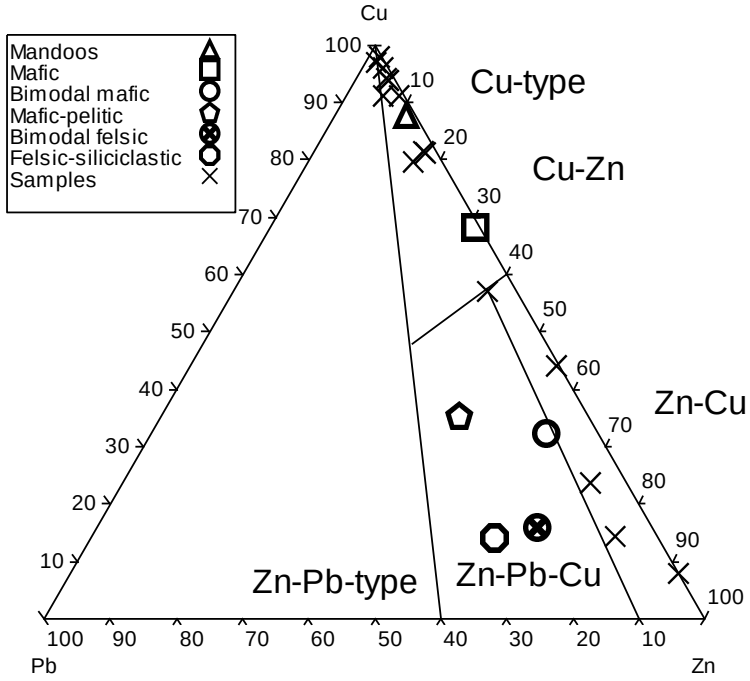

Fig 8. 1 - Cu-Pb-Zn diagram displaying metal concentrations for different VMS deposits according to their host-rock.

in sulphide ores and clasts suggest that refining processes were not important during the development of Mandoos 1 ores, placing them in a black-smoker type environment (some of the studied samples conceivably represent products of the crumbling of hydrothermal chimneys). The large amount of primary textures (framboidal and colloform) preserved in the studied samples allows also to reconsider the topic regarding the biogenic origin of pyrite in such systems. Framboids are known to be spherical to sub-spherical aggregates, composed by microcrystals of equigranular pyrite with a dense (cubic-)packing arrangement; nevertheless, irregular aggregates (loose packing) are also common (Wilken & Barnes, 1997). Many authors suggested that these forms corresponded to pyritized bacterial colonies; however the nucleation of pyrite framboidal microcrystals can also be a result of the ferromagnetic properties of greigite (Fe_3S_4), the precursor in this type of structure. Some experimental studies

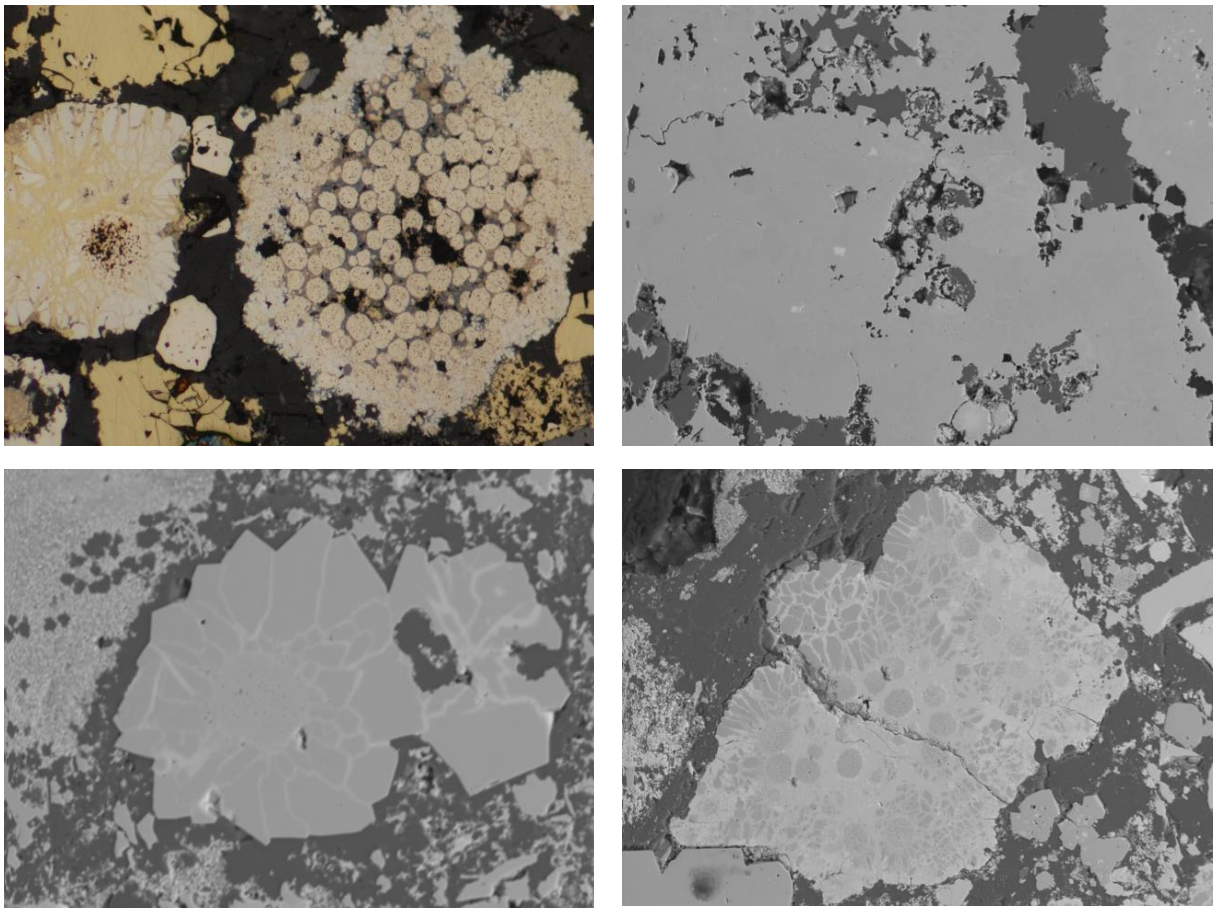

Fig 8. 2 – A – Framboidal pyrite; B – recrystallized pyrite with preserved spherulites; C – pyrite polyhedron crystallised around a framboid; D – clast of polyhedron pyrite with preserved framboidal core being replaced by chalcopyrite.

suggested that greigite can only persist in hydrothermal solutions below 200ºC; at such temperature, pyritization rates increase (Wilken & Barnes, 1997). According to Wilken & Barnes (1997) the preservation of framboidal textures may be related to secondary pyrite outward growth, while Ostwald & England (1979) suggested that the crystallization of euhedral pyrite forms can result from framboids recrystallisation; this recrystallisation is characterised by an intermediate stage, of pyrite spherulites, ending in the final euhedral shape; Fig 8.2 shows the same structures present in this deposit. In addition, colloform textures provide us a sequential information of physical and chemical conditions during precipitation and, despite the clear relationship between bacteria and sulphur reduction, the relationship of bacterial agents in the direct precipitation of crystals is more unlikely. These textures (colloform textures), just like framboidal, are thought to result of primary precipitation from the hydrothermal fluids, and not related to any bacterial related process. This is, possibly, the process that leads to the formation of most, if not all, colloform structures (Barrie *et al*. 2009).

It is also important to discuss the relationship between pyrite and marcasite, as well as between sphalerite and wurtzite, considering their coexistence in some of the studied samples. This aims to constrain the physical-chemical conditions that inhibit and/or favour one phase crystallization in relation to the other. Ramdohr (1969) describes marcasite, unlike pyrite, as unstable under most pressure and temperature conditions reproduced in laboratory experiments, only switched whenever particular circumstances are imposed (such as, quite acid solutions at moderate temperatures). It is also suggested by the same author that wurtzite is metastable and its occurrence is only possible under low pressure and temperature conditions in equilibrium with acid solutions. The commonly acceptable paramorphism implies the "changing" of wurtzite (hexagonal structure) to sphalerite (cubic structure); consequently, according to this reasoning, the two mineral phases can only coexist in contexts where the slow reaction time-periods

of the phase transformation are favoured. In sea mounds, dramatic variations in temperature and pH can be recorded within short distances (millimetres to centimetres) due to the interaction of hydrothermal vent fluids with cold sea water. Both minerals crystallise from acidic solutions; the mixture of such solution with sea water would result in a pH increase. This allows to explain the common presence of marcasite encased in pyrite crystals, where the abrupt variations in the chemical conditions promote the crystallisation of the most stable phase. The same process can be used to explain the presence of paramorphic sphalerite after wurtzite.

The Mandoos 1 stockwork is characterised by silicified basalts, where the silica is leached out from the basalt due to high temperatures, increasing porosity and resulting in sulphide dissemination. The continuous leaching can also be responsible for small/local collapses and creation of breccia zones. With the system cooling, the stockwork silicification becomes stronger due to the remaining silica advected from the deeper domains of the hydrothermal system. Strong silicification zones are seen associated with larger euhedral pyrite clusters formed in vuggs and also large anhedral pyrite clasts, showing breccia texture, possibly corresponding to local collapse zones.

As previously stated, the Mandoos sulphide ores are quite monotonous in composition and mainly formed by iron sulphides, although the presence of accessory Cu- and Zn-rich phases is common. A general paragenetic sequence resulted from petrography is illustrated in Fig 8.3. However, as seen before, in these kind of geological environment, significant chemical variations can took place in short-range space and such variations, combined with intense crumbling and mass-waste movements, may lead to different textural interpretations depending on the sampled area of the massive sulphide orebody.

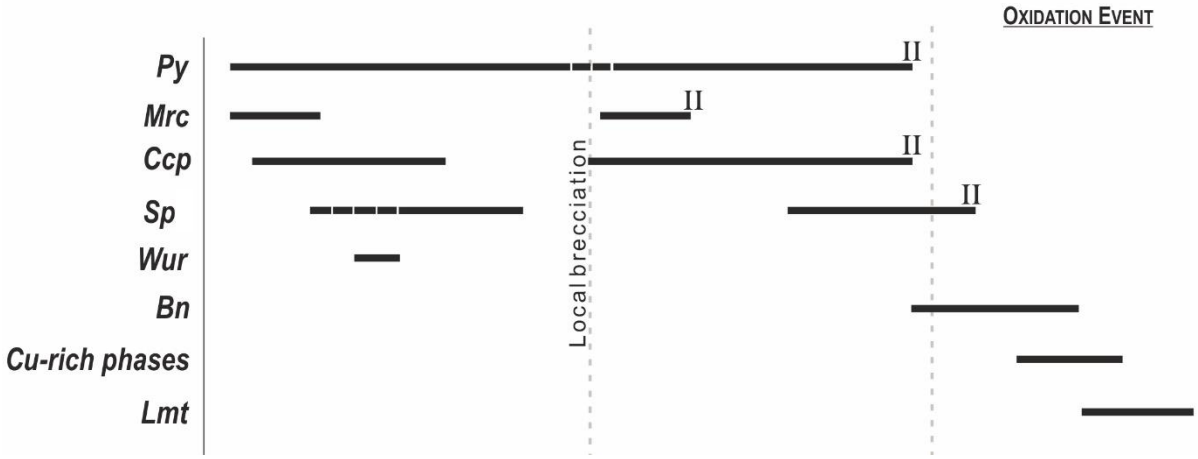

Fig 8. 3 – Schematic representation of the paragenetic sequence proposed for Mandoos 1 deposit.

The oxidation event is possibly synchronous of jaspers formation and the periodic leaching/silicification events would be responsible for the same hydrothermal imprint in jaspers and silicified (footwall) basalts. The sulphide dissemination in jaspers is possible due to an increasing of porosity during leaching, leading also to the formation of veins and some collapse breccias, later silicified when the system was subjected to cooling. The presence of the leached rims in the pyrite crystals indicate the circulation of late Fe-poor fluids, evidenced by the leaching of iron from the jaspers.

When massive sulphides are not covered, sea floor weathering can produce umbers and ochres, where massive sulphide breccias are oxidised and impregnated with silica in a colder and more oxidising environment. Nevertheless, these can also be formed by direct precipitation of metals within the water column, partly derived from the exhalative discharge, and further deposited in oxidising conditions along with the siliciclastic sediments (largely dominated by phyllosilicates).

Whole rock chemistry, more precisely the REE normalised pattern analysis, suggests that sulphide ores deposition is strongly influenced by a mixture of vent fluids and seawater, while the composition of umber and ochres is mainly determined by processes of seawater scavenging followed by phyllosilicate adsorption mechanisms (Fig 8.4). A mixture of seawater and vent fluids should also be involved in the formation of mineralised jaspers, but in this case the seawater weight in the mixture proportion is considerably higher. With the exception of umber and ochres, whose REE contents appear to derive exclusively from seawater, the REE abundances in sulphide ores and jaspers are conceivably related to the leaching and scavenging of footwall basalts synchronous of their hydrothermal alteration. It is known that footwall volcanic rocks are leached by infiltrated seawater, circulating along fractures, producing a variably modified seawater which is further released in hydrothermal chimneys, as vent fluid. Assuming that REE concentrations are in equilibrium with the vent fluid (i.e. that no significant fractionation took place after the massive sulphide ore and jaspers deposition) a simple simulation can be performed in order to predict the ratio of seawater (SW) and basalt involved in such process. Regarding to footwall less altered basalts (B), a SW:B mixing proportion scattered between 0.85:0.15 and 0.99:0.01 is needed to simulate the REE enrichment displayed by the studied samples. If the more altered footwall basalts (B') are used, the requested SW:B' proportion mixtures range between 0.50:0.50 and 0.95:0.05 because B' are significantly more depleted in REE than B. It is also noteworthy that SW:B and SW:B' interactions simulate roughly the measured vent fluids in modern analogues magnitudes (TAG an EPR) with mixing proportions between 0.999:0.001 and 0.9999:0.0001. Nevertheless, the pattern displayed by these vent fluids, characterised by an evident Eu positive anomaly and positive LREE and HREE fractionation, are not completely reproduced in this numerical simulation. This is related to the simplistic modelling and rough approach to the problem, which does not consider other geochemical factors that may control the vent fluid composition; as previously shown, there is evidence for a magmatic contribution to the hydrothermal fluid responsible for the mineralisation, and this may be one cause for the recorded differences.

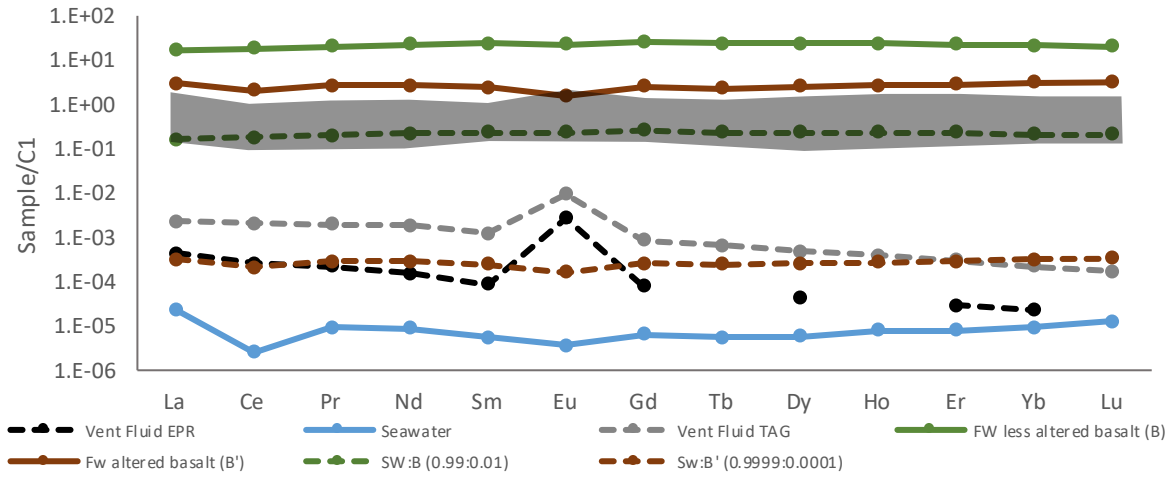

Fig 8. 4 – Vent fluid REE binary simulation using seawater and basalt compositions.

9. Conclusions

The metal contents of drill-core and open-pit samples place the Mandoos deposit in the Cu-rich VMS field, near the typical Mafic-type VMS deposits. Additionally, the 3D modelling performed with MICROMINE estimates on ca. 8 Mt of ore with 1.72 wt% in Cu. The lack of evident chemical zonation of the orebody, as indicated by the 3D modelling results, suggests also that metal zoning refinement processes were not significant all through the evolving stages recorded by the ore-forming system at Mandoos.

The massive ores are mainly composed of sulphide-rich breccias cemented by silica and/or zeolites, with minor phyllosilicates. These breccias are polymictic, comprising clasts widely varied in size, textural arrangements and mineral composition. They are possibly part of the talus found in many hydrothermal field vents in present-day analogues, where the (cyclic) crumbling of hydrothermal chimneys produce debris later cemented by siliceous fluids. This mineralisation type is characterised by a monotonous and simple mineral assemblage mainly composed of pyrite and marcasite with minor amounts of chalcopyrite, sphalerite and other Cu-rich phases.

The ubiquitous presence of primary textures, ranging from framboidal and colloform pyrite and marcasite, to the preservation of pyritised tubeworm burrows also place the studied samples in a black-smoker type vent. In these environments, the presence of framboidal pyrite crystal is interpreted as consequence of the magnetic properties of greigite, the precursor of pyrite. Additionally, the presence of marcasite and sphalerite (after pyrite and wurtzite, respectively) can be explained as a result of abrupt pH (and T?) modifications experienced by the hydrothermal fluids, especially when mixture with sea-water occurs in (sub)superficial conditions.

The formation of jaspers is considered to be a result of the temperature collapse of the hydrothermal system, correlative of the late oxidisation evolving stage, where Cu-rich mineral phases are formed (from chalcopyrite). Consequently, during the following bleaching of these silica and Fe-rich exhalative rocks, sulphide mineralization also occurs, from the scavenging of iron from the jaspers.

When the massive sulphides are exposed to the oxidising cold sea-water, oxidation phenomena occur, producing metalliferous sediments. These are easily distinguishable by their REE pattern and metal contents, which indicate that they derive, mostly, from sea-water fluids. Furthermore, the REE patterns for the massive sulphide breccias and mineralised jaspers are compatible with the mixture of vent fluid and sea-water. Vent fluid simulations were performed and established mixtures of SW:B and SW:B' scattered between 0.85:0.15 and 0.99:0.01, and 0.50:0.50 and 0.95:0.05, respectively, in order to reach ores and jaspers REE enrichment magnitudes. Modern day analogues vent fluid REE enrichments are predicted with mixtures of seawater and basalt ranging between 0.999:0.001 and 0.9999:0.0001, although, the typical pattern is not reproduced due to a magmatic contribution to the hydrothermal fluid which geochemical properties are not contemplated in the simulation.

References

ALABASTER, T., PEARCE, J.A. & MALPAS, J., 1982, The Volcanic Stratigraphy and Petrogenesis of the Oman Ophiolite Complex. *Contributions to Mineralogy and Petrology*, 81, 168-183.

ALABASTER, T., & PEARCE, J.A., 1985, The interrelationship between magmatic and ore-forming hydrothermal processes in the Oman ophiolite. *Economic Geology*, 80, 1–16.

BARRAT, J. A., KELLER, F., AMOSSÉ, J., TAYLOR, R. N., NESBITT, R. W. & HIRATA, T., 1996, Determination of rare earth elements in sixteen silicate reference samples by ICP-MS after Tm addition and ion exchange separation. *Geostandards Newsletter*, 20(1), 133-139.

BARRAT, J. A., YAMAGUCHI, A., GREENWOOD, R. C., BOHN, M., COTTEN, J., BENOIT, M. & FRANCHI, I. A., 2007, The Stannern trend eucrites: Contamination of main group eucritic magmas by crustal partial melts. *Geochimica et Cosmochimica Acta*, 71(16), 4108-4124.

BARRETT, T. J., JARVIS, I., LONGSTAFFE, F. J., & FARQUHAR, R., 1988, Geochemical aspects of hydrothermal sediments in the eastern Pacific Ocean; an update. *The Canadian Mineralogist*, 26(3), 841-858.

BARRIE, C.T., HANNINGTION, M.D., 1999, Classification of Volcanic-Associated Massive Sulphide Deposits Based on Host-Rock Composition. Chapter 1 in Barrie, C.T., and Hannington, M.D., (eds) Volcanic-Associated Massive Sulphide Deposits: Processes and Examples in Modern and Ancient Settings. *Reviews in Economic Geology*, 8, 1-12.

BARRIE, C. D., BOYCE, A. J., BOYLE, A. P., WILLIAMS, P. J., BLAKE, K., OGAWARA, T., & PRIOR, D. J., 2009, Growth controls in colloform pyrite. *American Mineralogist*, 94(4), 415-429.

DILEK, Y., FURNES, H., 2009, Structure and Geochemistry of the Tethyan ophiolites and their Petrogenesis in subduction rollback systems. *Lithos*, 113, 1-20

FLEET, A.J., & ROBERTSON, A.H.F., 1980, Ocean-ridge metalliferous and pelagic sediments of the Semail Nappe, Oman. *Journal of the Geological Society*, 137, 403-422

FRANKLIN, J.M., GIBSON, H.L., JONASSON, I.R., GALLEY, A.G., 2005, Volcanogenic Massive Sulphides. *Economic Geology 99th Anniversary Volume*, 523-560.

GALLEY, A.G., KOSKI, R.A., 1999, Setting and Characteristics of Ophiolite-Hosted Volcanogenic Massive Sulphide Deposits. CHAPTER 10 IN BARRIE, C.T., & HANNINGTON, M.D., (EDS), Volcanic-Associated Massive Sulphide Deposits: Processes and Examples in Modern and Ancient Settings. *Reviews in Economic Geology*, 8, 253-280.

GERMAN, C. R., HERGT, J., PALMER, M. R., & EDMOND, J. M., 1999, Geochemistry of a hydrothermal sediment core from the OBS vent-field, 21 N East Pacific Rise. *Chemical Geology*, 155(1), 65-75.

GILGEN, S.A., DIAMOND, L.W., MERCOLLI, I., AL-TOBI, K., MAIDMENT, D.W., CLOSE, R., AL-TOWAYA, A., 2014, Volcanostratigraphic Controls on the Occurrence of Massive Sulphide Deposits in the Sumail Ophiolite, Oman. *Economic Geology*, 109, 1585-1610.

GLENNIE, K. W., BOEUF, M. G. A., CLARKE, M. H., MOODY-STUART, M., PILAAR, W. F. H., & REINHARDT, B. M., 1973, Late Cretaceous nappes in Oman Mountains and their geologic evolution. *AAPG Bulletin*, 57(1), 5-27.

GODARD, M., DAUTRIA, J.-M., & PERRIN, M., 2003, Geochemical variability of the Oman Ophiolite lavas; relationship with spatial distribution and paleomagnetic directions. *Geochemistry, Geophysics, Geosystems*, 4(6), 1-15.

HANNINGTON, M.D., 2014, Volcanogenic Massive Sulphide Deposits. IN HEINRICH D., HOLLAND, H.D. AND TUREKIAN, K.K. (EDS), *Treatise on Geochemistry (2nd Edition)*, 13, 463-488.

IMMENHAUSER, A., SCHREURS, G., GNOS, E., OTERDOOM, H. W., & HARTMANN, B., 2000, Late Palaeozoic to Neogene geodynamic evolution of the northeastern Oman margin. *Geological Magazine*, 137(1), 1-18.

KUSANO, Y., ADACHI, Y., MIYASHITA, S., UMINO, S., 2012, Lava accretion system around mid-ocean ridges: Volcanic stratigraphy in the Wadi Fizh area, northern Oman ophiolite. *Geochemistry, Geophysics, Geosystems*, 13.

LI –H, SCHOONMAKER J.E., 2003, Chemical Composition and Mineralogy of Marine Sediments. In: Elsevier's Treatise on Geochemistry, Vol 7: Sediments, diagenesis, and sedimentary rocks. *FT Mackenzie (Ed.)* : 41-35.

LIPPARD, S.J., SHELTON, A.W., & GASS, I.G., 1986, The ophiolite of northern Oman. *Blackwell Scientific Publications Ltd*, 165 p.

MACLEOD, C. J., & ROTHERY, D. A., 1992, Ridge axial segmentation in the Oman ophiolite: evidence from along-strike variations in the sheeted dyke complex. *Geological Society, London, Special Publications*, 60(1), 39-63.

MAWARID MINING, 2014, Information Guide – Regional and Local Geology of Mandoos. Mawarid Mining, *Unpublished memorandum*, 12p.

MILLS, R. A., & ELDERFIELD, H., 1995, Rare earth element geochemistry of hydrothermal deposits from the active TAG Mound, 26 N Mid-Atlantic Ridge. *Geochimica et Cosmochimica Acta*, 59(17), 3511-3524.

OSTWALD, J., & ENGLAND, B. M., 1979, The relationship between euhedral and framboidal pyrite in base-metal sulphide ores. *Mineral. Mag*, 43, 297-300.

PALME, H. & JONES, A., 2004, Solar system abundances of the Elements. In: Treatise on Geochemistry, Volume 1 (H.D. Holland & K.K. Turekian, eds.), *Elsevier, Amsterdam*, 41-61.

PALME, H. & O'NEILL, H. ST. C., 2004, Cosmochemical Estimates of Mantle Composition. In: Treatise on Geochemistry, Volume 2 (R.W. Calson, eds.), *Elsevier, Amsterdam*, 1-38.

RAMDOHR, P., 1969, The ore minerals and their intergrowths. *Elsevier*.

ROBERTSON, A. H. F., & FLEET, A. J., 1976, The origins of rare earths in metalliferous sediments of the Troodos Massif. Cyprus. *Earth and Planetary Science Letters*, 28(3), 385-394.

ROLLINSON, H., 2009, New models for the genesis of plagiogranites in the Oman ophiolite. *Lithos*, 112(3), 603-614.

ROLLINSON, H.R., SEARLE, M.P., ABBASI, I.A., AL-LAZKI, A.I., AL KINDI, M.H., 2014, Tectonic evolution of the Oman Mountains: an introduction, In ROLLISON, H.R., SEARLE, M.P., ABBASI, I.A., AL-LAZKI, A. & AL KINDY (eds) Tectonic Evolution of the Oman Mountains. *Geological Society*, 392, 1-7.

SEARLE, M. P., & MALPAS, J., 1982, Petrochemistry and origin of sub-ophiolitic metamorphic and related rocks in the Oman Mountains. *Journal of the Geological Society*, 139(3), 235-248.

SEARLE, M.P., & COX, J., 1999, Tectonic setting, origin, and obduction of the Oman ophiolite. *Geological Society of America Bulletin*, 111, 104–122.

WILKIN, R. T., & BARNES, H. L., 1997, Formation processes of framboidal pyrite. *Geochimica et Cosmochimica Acta*, 61(2), 323-339.

YOKOYAMA, T., MAKISHIMA, A. & NAKAMURA, E., 1999, Evaluation of the coprecipitation of incompatible trace elements with fluoride during silicate rock dissolution by acid digestion. *Chemical Geology*, 157(3), 175-187.

Appendix I – List of Samples

List of Samples							
REF	Mounts	Thin Section	Powder WR	REF	Mounts	Thin Section	Powder WR
MD-P1-1-1			1	MD150-112.	1		
MD-P1-1-2	1			MD150-114.	1		1
MD-P1-2-3	1			MD174-62.1	1		1
MD-P1-2-4	1			MD174-79.0	1		1
MD-P1-3-1	1			MD178-110.50		1	1
MD-P1-3-5	1			MD178-128.	1		1
MD-P1-5-1	1			MD178-134.	1	1	1
MD-P1-5-5	1			MD429-103.	1		
MD-P1-6-3	1			MD429-104.00			1
MD-P2-1-3	2			MD429-109.	1		1
MD-P2-1-6	2			MD430-127.	1		
MD-P2-2A		1	1	MD430-129.	1	1	
MD-P2-2B			1	MD430-131.	1		
MD-P2-3-2	2			MD430-132.	1		
MD-P2-6-3		1		MD431-107.	1		1
MD-P3-2-1	1			MD431-108.	2		1
MD-P3-4-1	1		1	MD431-109.	1		1
MD-P3-5-2	1	1		MD431-110.	1		1
MD-P3-6-1	2						
MD-P3-6-2	1						
MD-P3-6-3	1						
MD-NP-1	3		1				
MD-NP-2	1						
MD-NP-3	1		1				

Appendix II – XRF detection Limits

XRF Detection Limits (ppm)			
Ba	6.9	Br	0.78
Cu	2.84	Nb	0.84
Zn	1.28	Mo	0.78
As	4.06	Ag	4.98
Pb	1.72	Sb	4.18
Sn	3.02	I	6.6
W	3.7	Hf	4.06
Bi	1.54	Tl	2.14
Cr	1.96	Th	2.52
Rb	0.64	U	1.22
Sr	0.72	La	10.08
Ta	3.86	Y	0.86
Cs	4.78	Nd	5.98
V	2.78	Sm	6.42
Cd	3.88	Yb	5.54
Co	4.54	Ce	10.9
Ni	2	Sc	3
Ga	0.94	Te	6.28
Ge	1.04	Zr	0.8
Se	0.84		

Appendix III – ICP-MS Instrumental detection limits, analytical and total procedural blanks

	Instrumental detection limit	Analytical procedural blank	Total procedural blank
	pg.g^{-1}	*ng.g^{-1}*	*ng.g^{-1}*
Li	nd	20.6	48.6
Sc	nd	1.05	1.24
Ti	0.969	630	642
V	0.278	19.6	20.2
Cr	1.56	1249	1252
Mn	2.90	76.0	82.0
Co	0.113	17.5	18.0
Ni	22.2	199	214
Cu	2.02	17.7	18.7
Zn	74.5	281	301
Ga	0.216	1.06	1.11
Rb	0.433	3.89	6.28
Sr	5.32	4.28	7.41
Y	nd	0.093	0.171
Zr	1.38	4.61	5.38
Nb	1.71	1.83	2.37
Cs	0.100	1.13	1.28
Ba	20.1	7.84	8.35
La	0.121	0.115	0.307
Ce	0.151	0.289	0.606
Pr	0.040	0.022	0.070
Nd	0.084	0.077	0.100
Sm	0.078	0.061	0.065
Eu	0.065	0.081	0.090
Gd	0.259	0.123	0.134
Tb	nd	0.018	0.047
Dy	0.079	0.041	0.045
Ho	0.025	0.008	0.018
Er	0.033	0.070	0.073
Yb	0.051	0.022	0.029
Lu	0.013	0.014	0.021
Hf	1.21	0.225	0.240
Ta	0.701	0.313	0.413
Pb	0.245	7.05	7.97
Th	0.247	0.035	0.073
U	0.036	0.064	0.076

Appendix IV- EPMA Analytical Conditions

EPMA Analytical Conditions			
Element	**X-Ray**	**Crystal**	**Standard**
Bi	Ma	PETJ	Bismuth Selenide
Ga	La	TAP	Metallic Ga
Pb	Ma	PETJ	Galena
Au	Ma	PETH	Au
Ag	La	PETJ	Ag
Ge	La	TAP	Metallic Ge
Cd	La	PETJ	Cd
Mo	La	PETH	Molybdenite
In	La	PETJ	Metallic In
As	La	TAP	Galium Arsenide
Sn	La	PETJ	Metallic Sn
S	Ka	PETH	Pyrite
Ni	Ka	LIF	Pentlandite
Se	La	TAP	Bismuth Selenide
Zn	Ka	LIF	Sphalerite
Fe	Ka	LIFH	Pyrite
Sb	La	PETJ	Stibnite
Mn	Ka	PETJ	Bustamite
Co	Ka	LIFH	Skutterudite
Cu	Ka	LIFH	Cuprite

Appendix V – EPMA Detection Limits

Detection Limits (ppm)							
	Pyrite	**Marcasite**	**Chalcopyrite**	**Bornite**	**Cu-rich phases**	**Sphalerite**	**Galena**
Bi	872	829	783	779	794	683	3662
Ga	163	157	151	150	160	229	214
Pb	621	603	557	539	595	553	858
Au	249	264	229	257	257	248	395
Ag	228	239	263	266	247	259	347
Ge	141	141	139	127	139	133	187
Cd	254	250	266	275	276	267	338
Mo	178	180	181	172	177	171	582
In	287	297	292	310	304	310	350
As	243	240	238	220	240	224	333
Sn	253	261	272	268	291	278	340
S	59	58	57	57	61	56	96
Ni	331	352	372	380	380	376	568
Se	180	185	170	165	197	172	256
Zn	595	580	642	643	656	669	1017
Fe	177	176	185	186	194	186	279
Sb	300	289	307	319	328	319	390
Mn	243	236	258	257	271	261	368
Co	169	166	184	186	189	190	278
W	828	878	1210	1254	1405	953	
Te	277	261	293	288	294	295	
Cu	281	278	299	308	322	319	451

Appendix VI – Mandoos 1 Deposit Sections (2733000mN and 2732850mN)

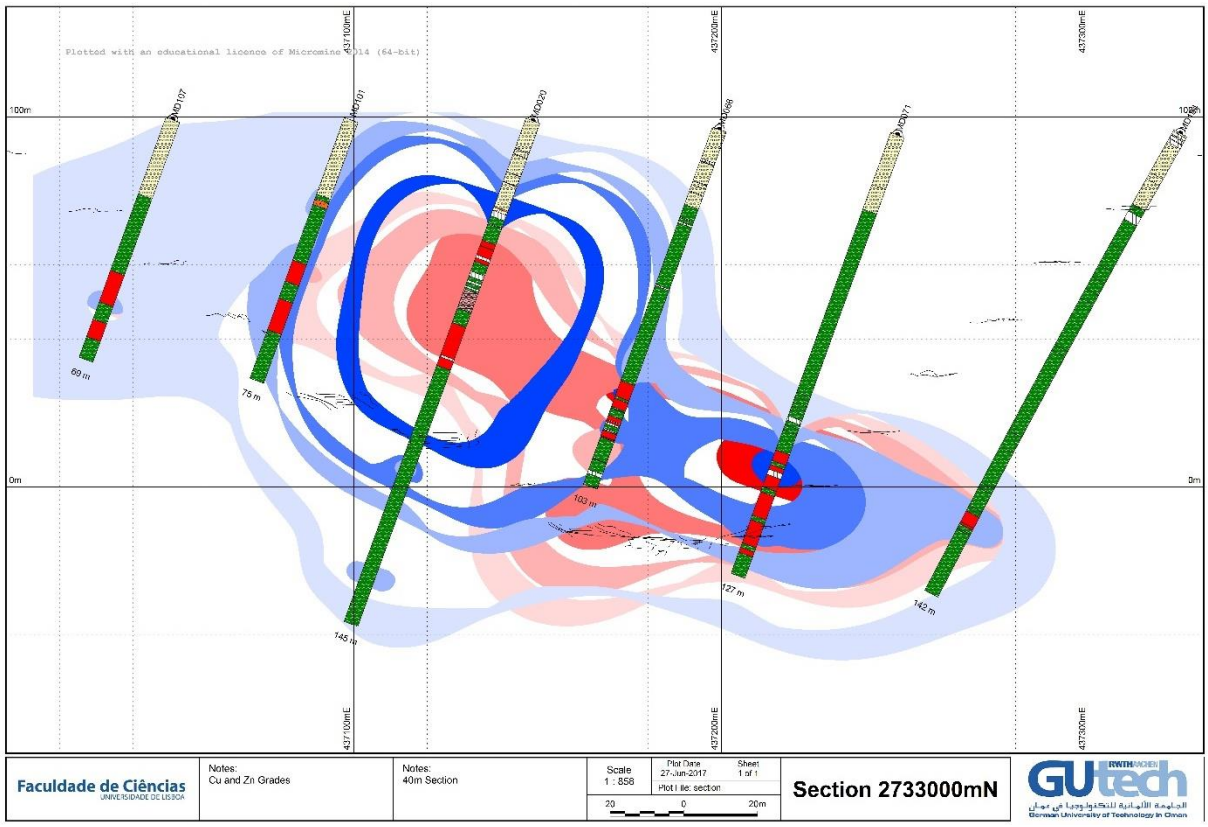

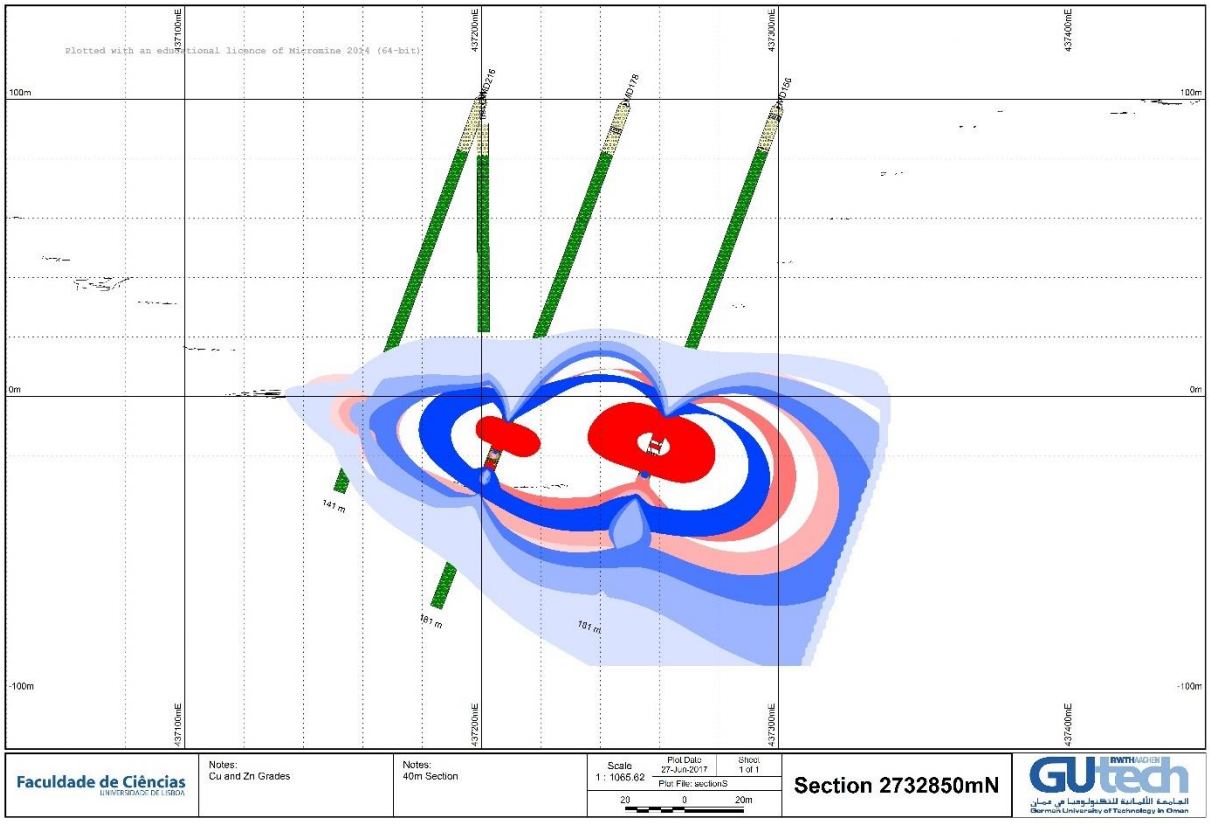

Appendix VII – EPMA Analyses Statistics

EPMA Analysis Statistics																																
	Pyrite *(n=310)*					Marcasite *(n=111)*					Chalcopyrite (n=262)					Bornite *(n=16)*					Cu-rich phases *(n=64)*					Sphalerite *(n=181)*					Galena *(n=5)*				
	Median	Min	Max	Mean	Std-Dev	Median	Min	Max	Mean	Std-Dev	Median	Min	Max	Mean	Std-Dev	Median	Min	Max	Mean	Std-Dev	Median	Min	Max	Mean	Std-Dev	Median	Min	Max	Mean	Std-Dev	Median	Min	Max	Mean	Std-Dev
Bi	0.000	0.000	0.018	0.000	0.001	0.000	0.000	0.015	0.000	0.001	0.000	0.000	0.055	0.001	0.006	0.000	0.000	0.000	0.000	0.000	0.000	0.000	0.346	0.008	0.045	0.000	0.000	0.068	0.003	0.011	0.000	0.000	0.000	0.000	0.000
Ga	0.000	0.000	0.071	0.004	0.010	0.000	0.000	0.045	0.004	0.009	0.000	0.000	0.087	0.007	0.015	0.007	0.000	0.025	0.008	0.008	0.000	0.000	0.093	0.010	0.018	0.000	0.000	0.000	0.000	0.000	0.006	0.000	0.016	0.006	0.007
Pb	0.018	0.000	0.707	0.046	0.084	0.020	0.000	0.385	0.042	0.059	0.034	0.000	0.265	0.048	0.050	0.088	0.000	0.142	0.077	0.055	0.057	0.000	0.293	0.065	0.065	0.011	0.000	0.496	0.039	0.060	86.393	85.682	87.254	86.308	0.653
Au	0.005	0.000	0.069	0.012	0.016	0.005	0.000	0.096	0.013	0.018	0.000	0.000	0.072	0.012	0.017	0.000	0.000	0.036	0.004	0.011	0.000	0.000	0.070	0.010	0.019	0.000	0.000	0.073	0.010	0.016	0.000	0.000	0.000	0.000	0.000
Ag	0.000	0.000	0.452	0.012	0.033	0.000	0.000	0.061	0.010	0.016	0.000	0.000	0.067	0.011	0.015	0.015	0.000	0.052	0.019	0.020	0.022	0.000	0.133	0.029	0.030	0.000	0.000	0.076	0.010	0.015	0.000	0.000	0.006	0.001	0.003
Ge	0.000	0.000	0.037	0.002	0.006	0.000	0.000	0.022	0.002	0.004	0.000	0.000	0.055	0.004	0.009	0.000	0.000	0.009	0.001	0.003	0.000	0.000	0.045	0.002	0.007	0.000	0.000	0.148	0.008	0.019	0.000	0.000	0.037	0.010	0.016
Cd	0.000	0.000	0.076	0.007	0.013	0.000	0.000	0.056	0.007	0.012	0.000	0.000	0.072	0.009	0.015	0.000	0.000	0.043	0.006	0.012	0.008	0.000	0.097	0.017	0.023	0.203	0.000	0.673	0.237	0.163	0.000	0.000	0.000	0.000	0.000
Mo	0.000	0.000	0.082	0.008	0.014	0.000	0.000	0.059	0.008	0.014	0.034	0.000	0.109	0.036	0.023	0.026	0.000	0.055	0.026	0.018	0.034	0.000	0.077	0.032	0.022	0.056	0.000	0.125	0.056	0.025	0.000	0.000	0.000	0.000	0.000
In	0.007	0.000	0.097	0.016	0.019	0.006	0.000	0.077	0.018	0.020	0.006	0.000	0.100	0.015	0.020	0.013	0.000	0.079	0.020	0.023	0.002	0.000	0.058	0.012	0.015	0.000	0.000	0.064	0.008	0.015	0.000	0.000	0.046	0.009	0.021
As	0.007	0.000	0.572	0.030	0.066	0.003	0.000	0.465	0.015	0.048	0.000	0.000	0.107	0.011	0.017	0.003	0.000	0.039	0.006	0.011	0.004	0.000	12.643	1.109	2.766	0.000	0.000	0.177	0.009	0.018	0.003	0.000	0.022	0.006	0.009
Sn	0.000	0.000	0.070	0.011	0.016	0.002	0.000	0.064	0.011	0.017	0.000	0.000	0.198	0.015	0.025	0.000	0.000	0.071	0.016	0.023	0.000	0.000	0.063	0.012	0.017	0.000	0.000	0.066	0.009	0.015	0.006	0.000	0.041	0.016	0.016
S	53.097	47.820	54.054	52.917	0.691	53.129	51.272	53.868	53.032	0.457	34.935	32.604	36.432	34.864	0.373	26.270	26.094	26.644	26.267	0.138	30.708	24.929	41.090	30.457	3.404	33.309	31.900	39.116	33.333	0.648	13.590	12.954	13.625	13.453	0.283
Ni	0.003	0.000	0.080	0.013	0.018	0.004	0.000	0.068	0.012	0.016	0.000	0.000	0.082	0.011	0.017	0.000	0.000	0.033	0.005	0.010	0.000	0.000	0.074	0.011	0.017	0.005	0.000	0.059	0.013	0.017	0.000	0.000	0.000	0.000	0.000
Se	0.009	0.000	0.269	0.015	0.027	0.000	0.000	0.051	0.007	0.012	0.009	0.000	0.099	0.016	0.020	0.000	0.000	0.036	0.006	0.011	0.002	0.000	0.095	0.012	0.018	0.005	0.000	0.102	0.016	0.020	0.010	0.000	0.069	0.020	0.029
Zn	0.032	0.000	2.789	0.142	0.371	0.032	0.000	0.980	0.082	0.158	0.092	0.000	5.029	0.436	0.758	0.190	0.015	0.906	0.243	0.258	0.422	0.003	25.074	2.443	4.738	64.386	45.987	67.892	63.252	4.159	0.558	0.473	2.055	1.060	0.631
Fe	46.247	41.087	47.070	45.973	0.853	46.146	42.926	46.910	45.986	0.609	30.332	26.831	32.586	30.195	0.614	11.463	11.304	12.183	11.580	0.260	13.703	1.253	34.715	13.798	6.794	1.255	0.088	14.287	2.316	2.592	0.111	0.065	0.341	0.154	0.108
Sb	0.000	0.000	0.103	0.011	0.016	0.000	0.000	0.053	0.010	0.014	0.000	0.000	0.097	0.010	0.017	0.005	0.000	0.042	0.012	0.016	0.005	0.000	1.028	0.106	0.247	0.000	0.000	0.082	0.009	0.017	0.113	0.000	0.270	0.135	0.108
Mn	0.004	0.000	0.636	0.027	0.077	0.007	0.000	1.365	0.072	0.197	0.000	0.000	0.212	0.018	0.037	0.000	0.000	0.036	0.008	0.014	0.009	0.000	0.107	0.017	0.021	0.011	0.000	4.130	0.215	0.724	0.000	0.000	0.000	0.000	0.000
Co	0.020	0.000	0.840	0.032	0.064	0.020	0.000	0.076	0.019	0.014	0.010	0.000	0.062	0.013	0.013	0.004	0.000	0.037	0.010	0.013	0.004	0.000	0.047	0.009	0.012	0.003	0.000	0.101	0.011	0.018	0.000	0.000	0.038	0.013	0.016
W	0.000	0.000	0.298	0.028	0.050	0.000	0.000	0.231	0.029	0.052	0.000	0.000	0.000	0.000	0.000	0.000	0.000	0.000	0.000	0.000	0.000	0.000	0.000	0.000	0.000	0.000	0.000	0.293	0.033	0.055	-	-	-	-	-
Te	0.000	0.000	0.130	0.017	0.026	0.002	0.000	0.086	0.014	0.021	0.000	0.000	0.116	0.011	0.018	0.000	0.000	0.052	0.012	0.023	0.044	0.000	7.348	0.590	1.557	0.000	0.000	0.143	0.011	0.020	-	-	-	-	-
Cu	0.021	0.000	8.978	0.367	1.031	0.000	0.000	3.982	0.178	0.491	34.303	31.609	38.136	34.201	0.910	63.201	61.317	63.997	62.854	0.880	53.250	22.359	72.772	50.951	11.360	0.266	0.000	9.861	0.651	1.214	0.381	0.090	0.503	0.315	0.187

Appendix VIII

EPMA Representative Analysis

	Pyrite			Marcasite			Chalcopyrite			Bornite			Covellite	Spionkopite		Sphalerite			Galena		
Bi	0.000	0.000	0.000	0.000	0.000	0.000	0.000	0.000	0.000	0.000	0.000	0.000	0.000	0.000	0.000	0.000	0.000	0.068	0.000	0.000	0.000
Ga	0.000	0.000	0.000	0.000	0.000	0.000	0.027	0.000	0.027	0.012	0.000	0.000	0.000	0.000	0.013	0.000	0.000	0.000	0.000	0.006	0.000
Pb	0.000	0.076	0.092	0.122	0.000	0.000	0.085	0.000	0.000	0.044	0.088	0.000	0.057	0.075	0.050	0.000	0.028	0.000	85.698	86.393	85.682
Au	0.000	0.022	0.009	0.000	0.000	0.000	0.000	0.000	0.000	0.000	0.036	0.000	0.000	0.000	0.000	0.000	0.001	0.000	0.000	0.000	0.000
Ag	0.037	0.007	0.000	0.000	0.006	0.000	0.000	0.000	0.000	0.035	0.016	0.004	0.000	0.051	0.049	0.000	0.028	0.019	0.000	0.006	0.000
Ge	0.000	0.000	0.001	0.000	0.000	0.000	0.021	0.000	0.000	0.000	0.000	0.000	0.000	0.000	0.015	0.000	0.010	0.000	0.011	0.000	0.000
Cd	0.000	0.000	0.000	0.000	0.000	0.000	0.000	0.007	0.011	0.043	0.000	0.018	0.005	0.000	0.046	0.293	0.154	0.168	0.000	0.000	0.000
Mo	0.000	0.014	0.018	0.000	0.017	0.023	0.027	0.015	0.026	0.024	0.012	0.042	0.019	0.000	0.000	0.077	0.072	0.060	0.000	0.000	0.000
In	0.006	0.000	0.034	0.053	0.038	0.000	0.000	0.013	0.043	0.013	0.010	0.079	0.028	0.019	0.006	0.000	0.000	0.043	0.000	0.000	0.000
As	0.184	0.000	0.000	0.031	0.003	0.000	0.000	0.026	0.060	0.000	0.000	0.008	0.000	0.000	0.000	0.000	0.000	0.001	0.000	0.000	0.006
Sn	0.017	0.000	0.004	0.008	0.000	0.000	0.000	0.010	0.029	0.010	0.041	0.000	0.000	0.000	0.000	0.000	0.000	0.022	0.022	0.006	0.000
S	53.255	53.165	53.204	52.895	52.746	53.105	35.192	34.812	35.065	26.270	26.331	26.115	31.308	27.380	28.296	33.354	33.151	33.328	12.954	13.597	13.590
Ni	0.003	0.037	0.000	0.011	0.021	0.018	0.000	0.036	0.000	0.019	0.033	0.012	0.000	0.000	0.000	0.016	0.059	0.000	0.000	0.000	0.000
Se	0.020	0.008	0.000	0.010	0.000	0.013	0.050	0.050	0.007	0.000	0.000	0.000	0.039	0.000	0.004	0.045	0.055	0.045	0.000	0.023	0.000
Zn	0.017	0.000	0.000	0.748	0.138	0.246	0.684	2.541	0.996	0.078	0.082	0.109	0.202	0.076	0.202	65.035	65.600	65.646	1.077	0.558	0.473
Fe	46.524	46.034	46.176	45.169	45.514	45.702	31.262	29.560	30.611	11.412	11.674	11.348	1.299	1.253	1.525	0.662	0.588	0.661	0.341	0.134	0.111
Sb	0.034	0.019	0.000	0.000	0.000	0.000	0.024	0.002	0.000	0.042	0.000	0.000	0.005	0.042	0.033	0.001	0.000	0.000	0.000	0.270	0.215
Mn	0.037	0.000	0.002	0.044	0.054	0.060	0.156	0.105	0.072	0.000	0.031	0.004	0.000	0.000	0.000	0.030	0.000	0.000	0.000	0.000	0.000
Co	0.007	0.019	0.011	0.021	0.028	0.007	0.004	0.025	0.000	0.000	0.000	0.004	0.000	0.004	0.000	0.012	0.013	0.000	0.038	0.010	0.000
W	0.000	0.000	0.000	0.181	0.000	0.000	0.000	0.000	0.000	0.000	0.000	0.000	0.000	-	-	0.049	0.086	0.002	-	-	-
Te	0.001	0.000	0.028	0.000	0.021	0.013	0.000	0.006	0.009	0.000	0.052	0.000	0.043	-	-	0.055	0.001	0.000	-	-	-
Cu	0.003	0.180	0.228	0.564	0.534	0.584	33.450	33.119	33.753	63.702	63.435	63.997	66.734	72.772	71.194	0.568	0.411	0.249	0.090	0.458	0.503
Bi	0.000	0.000	0.000	0.000	0.000	0.000	0.000	0.000	0.000	0.000	0.000	0.000	0.000	0.000	0.000	0.000	0.000	0.000	0.000	0.000	0.000
Ga	0.000	0.000	0.000	0.000	0.000	0.000	0.001	0.000	0.001	0.001	0.000	0.000	0.000	0.000	0.006	0.000	0.000	0.000	0.001	0.000	0.000
Pb	0.000	0.000	0.001	0.001	0.000	0.000	0.001	0.000	0.000	0.001	0.002	0.000	0.000	0.012	0.008	0.000	0.000	0.000	1.005	0.983	0.976
Au	0.000	0.000	0.000	0.000	0.000	0.000	0.000	0.000	0.000	0.000	0.001	0.000	0.000	0.000	0.000	0.000	0.000	0.000	0.000	0.000	0.000
Ag	0.000	0.000	0.000	0.000	0.000	0.000	0.000	0.000	0.000	0.002	0.001	0.000	0.000	0.016	0.014	0.000	0.000	0.000	0.000	0.000	0.000
Ge	0.000	0.000	0.000	0.000	0.000	0.000	0.001	0.000	0.000	0.000	0.000	0.000	0.000	0.000	0.007	0.000	0.000	0.000	0.000	0.000	0.000
Cd	0.000	0.000	0.000	0.000	0.000	0.000	0.000	0.000	0.000	0.002	0.000	0.001	0.000	0.000	0.013	0.003	0.001	0.001	0.000	0.000	0.000
Mo	0.000	0.000	0.000	0.000	0.000	0.000	0.001	0.000	0.000	0.001	0.001	0.002	0.000	0.000	0.000	0.001	0.001	0.001	0.000	0.000	0.000
In	0.000	0.000	0.000	0.001	0.000	0.000	0.000	0.000	0.001	0.001	0.000	0.003	0.000	0.005	0.002	0.000	0.000	0.000	0.001	0.000	0.000
As	0.003	0.000	0.000	0.001	0.000	0.000	0.000	0.001	0.001	0.000	0.000	0.001	0.000	0.000	0.000	0.000	0.000	0.000	0.000	0.000	0.000
Sn	0.000	0.000	0.000	0.000	0.000	0.000	0.000	0.000	0.000	0.000	0.002	0.000	0.000	0.000	0.000	0.000	0.000	0.000	0.001	0.000	0.000
S	2.000	2.000	2.000	2.000	2.000	2.000	2.000	2.000	2.000	4.000	4.000	4.000	1.000	28.000	28.000	1.000	1.000	1.000	1.000	1.000	1.000
Ni	0.000	0.001	0.000	0.000	0.000	0.000	0.000	0.001	0.000	0.002	0.003	0.001	0.000	0.000	0.000	0.000	0.001	0.000	0.000	0.000	0.000
Se	0.000	0.000	0.000	0.000	0.000	0.000	0.001	0.001	0.000	0.000	0.000	0.000	0.001	0.000	0.002	0.001	0.001	0.001	0.000	0.001	0.000
Zn	0.000	0.000	0.000	0.014	0.003	0.005	0.019	0.072	0.028	0.006	0.006	0.008	0.003	0.038	0.098	0.956	0.970	0.966	0.057	0.020	0.017
Fe	1.003	0.994	0.997	0.981	0.991	0.988	1.020	0.975	1.002	0.998	1.018	0.998	0.024	0.736	0.866	0.011	0.010	0.011	0.018	0.006	0.005
Sb	0.000	0.000	0.000	0.000	0.000	0.000	0.000	0.000	0.000	0.002	0.000	0.000	0.000	0.011	0.009	0.000	0.000	0.000	0.000	0.005	0.004
Mn	0.001	0.000	0.000	0.001	0.001	0.001	0.005	0.004	0.002	0.000	0.003	0.000	0.000	0.000	0.000	0.001	0.000	0.000	0.002	0.000	0.000
Co	0.000	0.000	0.000	0.000	0.001	0.000	0.000	0.001	0.000	0.000	0.000	0.000	0.000	0.002	0.000	0.000	0.000	0.000	0.000	0.000	0.000
W	0.000	0.000	0.000	0.001	0.000	0.000	0.000	0.000	0.000	0.000	0.000	0.000	0.000	-	-	0.000	0.000	0.000	-	-	-
Te	0.000	0.000	0.000	0.000	0.000	0.000	0.000	0.000	0.000	0.000	0.002	0.000	0.000	-	-	0.000	0.000	0.000	-	-	-
Cu	0.000	0.003	0.004	0.011	0.010	0.011	0.959	0.960	0.971	4.894	4.863	4.946	1.076	37.552	35.548	0.009	0.006	0.004	0.002	0.017	0.019

Appendix IX – Mandoos 1 Samples Data

Note: Highlighted cells in the major elements section correspond to data converted from ppm to wt%, except S wich was converted from Ox% to element%. The highlighted trace elements cells were converted from wt% to ppm.

	Sulphide Ores										Umber & Ochres						Jaspers	
Sample	MD-NP-1	MD-P1-1-1	MD-174-79.00	MD-P3-4-1	MD-178-128.80	MD-429-109.10	MD-431-107.00	MD-431-108.00	MD-431-109.70	MD-431-110.5	MD-178-110.5	MD-P2-2A	MD-P2-2B	MD-429-104.00	MD-174-62.15	MD-178-134.20	MD-150.114.10	MD-NP-3
SiO2 wt%	11.022	0.273	8.847	2.663	11.585		12.78	13.871	12.45	10.45		45.451	35.013	18.174	25.16	40.131	30.053	10.45
Al2O3 wt%	5.457	0.097	0.28	1.165	1.474		0.037	0.053	0.039	0.044		3.648	3.247	2.097	3.562	2.134	0.447	0.044
TiO2 wt%	0.02		0.004									0.157	0.162	0.057	0.125	0.05	0.01	
Fe2O3 wt%	3.955	22.459	19.686	24.731	18.857		18.992	18.818	18.287	19.208		26.519	35.212	49.928	54.726	28.491	16.559	19.208
MgO wt%	0.296		0.311	0.097	0.16		0.031	0.033	0.031			2.235	1.988	1.822	2.292	1.349		
MnO wt%	0.044	0.0080	0.007	0.21	0.014	0.004	0.004	0.007	0.011	0.008	1.778	0.681	0.456	0.407	0.374	0.199	0.012	47.189
CaO wt%	1.417	0.018	0.024	16.353	0.397	0.115	0.014	0.015	0.019	0.024	5.88	12.609	6.226	9.495	2.668	1.016	0.134	0.024
Na2O wt%		0.048	0.068		0.097			0.041	0.073	0.055			0.298					0.055
K2O wt%	0.045	0.005	0.034	0.025	0.031		0.004	0.007	0.007	0.008		0.313	0.322	0.065	0.135	0.068	0.022	0.008
P2O5 wt%				0.032								1.277	0.877	1.317	1.438	0.826	0.116	
S wt%	12.6	16.6	14.8	15.3	14.2		14.9	14.0	14.4	14.5		0.2	4.6	3.8	1.5	5.4	11.4	14.5
Cu wt%	2.448	0.267	0.121	0.514	0.57		0.653	0.681	0.248	0.297		0.009	0.017	0.518	0.116	3.725	1.07	0.297
Zn wt%	29.118	0.057	0.008	0.048	0.726		0.034	0.014	0.052	0.017		0.05	0.051	0.105	0.079	0.134	0.023	0.017
Pb wt%	0.005	0.006	0.004	0.004	0.004	0.002	0.007	0.008	0.005	0.003	0.008	0.004	0.004	0.028	0.009	0.02	0.003	0.003
ppm																		
Li (ICP-MS)	0.32	0.01	7.19	0.1	4.2	5.79	2.61	4.33	1.47	0.97	21.15	11.17	13.17	6.61	9.46	14.6	6.21	2.59
Sc (ICP-MS)											4.59	4.12	5.18	2.33	4.68	2.11		0.38
V (ICP-MS)	65.69	8.81	8.7	23	33.89	56.06	62.08	67.15	20.84	53.58	165	343	778	571	931	408	63	371
Cr	18.9	22.2	55.9	40	23.9	4.64	15.9	5.5	6	13.5	15.64	97.8	66.7	69.6	92.3	140	33	16.24
Co (ICP-MS)	0.66	42.14	106.47	225.57	33.42	422.58	14.42	88.4	9.76	29.36	27.6	5.25	8.45	48.92	76.72	114.79	33.48	101.73
Ni (ICP-MS)		8.08	4.65	7.2	7.93	3.7	10.59	15.08	1.6	9.56	185.4	72.1	99.4	73.1	130.2	35.1	8.4	169.2
Ga (ICP-MS)	166.32	2.55	2.24	1.5	12.45	8.81	11.97	6.44	9.22	6.24	3.9	11.5	11.6	48.9	49.5	13.9	2.5	12.8
Ge (ICP-MS)	0.76	5.49	6.01	4.48	6.43	6.37	5.95	5.34	4.92	4.09	2.81	2.89	5.96	8.73	6.28	4	4.34	1.99
As (ICP-MS)	60.31	1024.23	244.57	323.89	476.47	265.3	303.71	280.87	342.55	273.51	383.01	66.68	165.74	322.34	229	204.05	491.11	84.13
Se (ICP-MS)	1.97	6.09	43.28	11.571	3.76	25.85	2.04	5.73	1.76	2.46	0.198	0.101	0.204	1.326	0.777	18.85	4.054	0.107
Rb (ICP-MS)	0.28	0.03	0.61	0.34	0.32	0.04	0.08	0.14	0.06	0.05	4.37	10.71	13.25	1.83	5.07	0.91	0.16	0.58
Sr (ICP-MS)	13.32	0.5	4.46	19.98	90.66	0.64	0.49	0.64	0.77	0.46	115.9	117.13	62.26	36.21	59.96	51.18	2.25	447.46
Y (ICP-MS)	0.538	0.026	0.18	3.7	0.092	0.144	0.148	0.27	0.106	0.082	60.03	40.86	55.88	27.96	57.28	27.01	2.43	2.03
Zr (ICP-MS)	1.035	0.077	0.182	0.4	0.085	0.144	0.167	0.343	0.114	0.119	33.85	27.29	33.96	14.44	30.94	12.07	2.71	1.51
Nb (ICP-MS)	0.024		0.01	0.01		0.015	0.02	0.04	0.012		2.735	1.832	2.396	1.088	2.354	0.913	0.178	0.128
Mo (ICP-MS)	108.27	8.11	3.36	17.556	26.51	1.57	8.04	3.32	2.45	4	0.443	1.191	1.44	14.707	13.412	10.498	83.082	248.007
Ag (ICP-MS)	1.69	0.194	0.238	1.062	0.372	0.233	0.872	0.962	0.642	0.87	0.019	0.018	0.018	0.332	0.022	0.601	0.592	0.004
Cd (ICP-MS)	2277.78	3.68	1.16	2.384	53.37	0.31	3.07	2.14	4.42	1.16	2.736	0.053	0.022	0.36	0.045	3.912	1.469	0.24
In (ICP-MS)	20.99	3.14	1.45	0.862	0.62	2.37	9.2	16.58	5.17	6.98	0.614	1.252	0.673	4.783	4.336	2.943	2.086	0.013
Sn (ICP-MS)	3.36	2.55	18.64	0.368	0.31	5.69	23.41	24.27	6.44	8.98	2.27	3.237	3.702	3.133	3.984	1.993	1.643	1.148
Sb (ICP-MS)	27.31	6.58	7.64	1.796	5.55	2.04	7.52	6.12	6.74	4.27	1.156	0.766	1.308	4.434	2.821	1.61	5.145	1.282
Te (ICP-MS)	0.4	27.46	5.79	13.998	3.44	21.78	10.93	15.39	3.09	28.58	0.327	0.561	0.828	1.425	5.812	6.201	1.979	0.017
Cs (ICP-MS)	0.041		0.019	0.022	0.019			0.015			0.26	0.675	0.888	0.106	0.345	0.04		0.018
Ba (ICP-MS)	2.17	0.12	6.29	0.8	34.96	0.13	0.32	0.66	0.33	0.3	78.8	27.1	28.5	9.1	25.4	17.1	1.5	742.5
La (ICP-MS)	0.062	0.013	0.041	0.38	0.029	0.037	0.034	0.049	0.02	0.022	50.07	29.25	34.58	18.8	34.97	12.1	1.04	2.21
Ce (ICP-MS)	0.147	0.039	0.04	0.5	0.039	0.04	0.071	0.092	0.031	0.042	16.5	11.6	12.9	6.5	12.9	6	0.8	5.9
Pr (ICP-MS)	0.022			0.09			0.011	0.013			8.22	4.68	6.33	3.12	6.08	2.22	0.23	0.45
Nd (ICP-MS)	0.132	0.034	0.035	0.49	0.025	0.041	0.064	0.053	0.027	0.031	34.13	19.72	27.08	12.7	25.29	9.51	1.02	1.7
Sm (ICP-MS)	0.043		0.013	0.14		0.013	0.022	0.016			6.62	3.94	5.59	2.47	5.14	2.04	0.24	0.45
Eu (ICP-MS)	0.021			0.1			0.013				1.89	1.17	1.74	0.74	1.49	0.58	0.13	0.01
Gd (ICP-MS)	0.072		0.021	0.22		0.016	0.021	0.026			8.38	5.24	7.49	3.2	6.89	2.83	0.27	0.42
Tb (ICP-MS)	0.011			0.039							1.198	0.78	1.089	0.466	1.01	0.43	0.044	0.092
Dy (ICP-MS)	0.084		0.022	0.31	0.014	0.017	0.022	0.031	0.011	0.012	7.8	4.89	7.08	3.02	6.61	3.02	0.31	0.62
Ho (ICP-MS)	0.019			0.08							1.7	1.11	1.57	0.68	1.52	0.71	0.07	0.14
Er (ICP-MS)	0.055		0.016	0.24		0.014	0.021	0.027			4.81	3.12	4.51	1.93	4.34	2.07	0.22	0.4
Yb (ICP-MS)	0.055		0.015	0.21	0.012	0.018	0.022	0.033			3.96	2.73	3.73	1.63	3.7	1.79	0.25	0.51
Lu (ICP-MS)				0.03							0.54	0.4	0.55	0.23	0.53	0.27	0.04	0.08
Hf (ICP-MS)	0.033			0.01							0.66	0.58	0.69	0.25	0.6	0.21	0.05	0.04
Ta		31.6	6	37.9	26.4		83.2	74.6	32.4	28.7		4.1	0.14	28.5	4.6	0.05	0.011	
W (ICP-MS)	0.249	0.037	0.02	0.04	0.122	0.043	0.126	0.054	0.101	0.077	0.545	1.146	1.624	2.131	1.641	0.922	0.17	1.695
Tl (ICP-MS)	0.16	3.64	1.76	3.128	7.77	0.34	2.73	5.07	2.53	4.2	0.12	0.079	0.106	0.407	0.074	0.33	8.844	1.351
Bi (ICP-MS)	0.013	0.019	0.015	0.013	0.013	0.014	0.014	0.017	0.016	0.014	0.017	0.015	0.014	0.011	0.013		0.014	0.016
Th (ICP-MS)				0.005				0.024			2.189	1.712	1.828	0.706	1.633	0.606	0.137	0.046
U (ICP-MS)	0.021	1.381	0.027	1.648	0.66	0.043	0.32	0.126	0.053	0.092	0.728	0.883	0.692	4.092	2.657	2.837	1.245	5.585

Appendix X – MD-NP-3 XRD Analysis

Dataset Name MD-NP-3

Ref. Code	Chemical Formula	Mineral Name
01-070-3755	Si O2	Quartz
98-002-0229	Mn1 O2	Pyrolusite

Pos. [°2Th.]	Height [cts]	FWHM Left [°2Th.]	d-spacing [Å]	Rel. Int. [%]
21.0671	197.58	0.2342	4.21712	12.68
25.6824	37.74	0.2007	3.46879	2.42
26.8524	1145.13	0.1673	3.32025	73.52
27.6229	56.03	0.2007	3.22936	3.60
28.8835	1557.61	0.1840	3.09122	100.00
36.7679	49.29	0.1004	2.44444	3.16
37.5418	272.51	0.2007	2.39582	17.50
39.7483	37.98	0.2007	2.26776	2.44
41.2022	98.25	0.2342	2.19104	6.31
42.9662	82.50	0.1338	2.10508	5.30
46.1574	38.41	0.5353	1.96670	2.47
50.2691	53.79	0.2342	1.81506	3.45
55.1491	14.22	0.2676	1.66544	0.91
56.7960	167.91	0.1673	1.62100	10.78
59.5141	85.62	0.2007	1.55330	5.50
60.2084	27.84	0.2007	1.53703	1.79
65.1049	18.57	0.2676	1.43278	1.19
67.3619	26.89	0.5353	1.39016	1.73
68.3650	36.69	0.3346	1.37219	2.36